ABSTRACT

Title of thesis: DESIGN AND TESTING
OF AN AUTOROTATIVE PAYLOAD DELIVERY SYSTEM :
THE AUTOBODY

Anne Brindejonc, Masters of Science, 2005

Thesis directed by: Prof. Inderjit Chopra & Dr. Jayant Sirohi
Department of Aerospace Engineering

This thesis presents the design, fabrication, testing and analytical study of a autonomous autorotative payload delivery system called the Autobody. The Autobody must be capable of passively deploying a payload, consisting of an electronics package, on ground from a conventional aircraft, by means of an autorotative rotor. Operational requirements specify the total vehicle weight of 5 lbs, require the vehicle to have a four foot diameter, four bladed rotor and a desired steady state rate of descent of the system to be less than 15 ft/s. It is important that the system achieves the steady state of autorotation quickly in order to minimize its impact upon landing and to ensure that the payload and the vehicle reach the ground safely. A novel rotor hub design incorporating negative pitch-flap coupling in conjunction with negative blade pitch and a negative precone is implemented to passively achieve the transition to a state of steady autorotation. An analytical model is developed to predict the Autobody behavior in a steady state autorotation. Wind tunnel tests were performed on a rotor model to validate the theory and to investigate the effect of different design variables on the steady state performance of the system. Good correlation with theory is observed over a range of design variables. A parametric study is then performed to investigate the influence of several rotor parameters on the system performance. An optimum full scale configuration is designed based on the parametric study. The full scale instrumented prototype is flight tested by dropping it from a hot air balloon. The aim of the instrumented flight tests is to establish the proof-of-concept of the optimum configuration, to ensure the rotor settings achieved a safe steady state rate of descent as well as to obtain data to validate the analytical

predictions. For an Autobody of 5 lbs, with a -41° pitch-flap coupling angle, a -10° pitch and a -4° precone, a minimum steady state descending velocity of 13.5 ft/s was observed. The flight test data showed a maximum error of 22.2% from the analytical predictions. Based on the theory and the flight tests, it is concluded that the proposed Autobody satisfactorily meets all operational requirements.

DESIGN AND TESTING OF AN AUTOROTATIVE PAYLOAD DELIVERY SYSTEM: THE AUTOBODY

by

Anne Brindejonc

Thesis submitted to the Faculty of the Graduate School of the
University of Maryland, College Park in partial fulfillment
of the requirements for the degree of
Masters of Science
2005

Advisory Committee:

Professor Inderjit Chopra, Chair/Advisor
Assistant Research Scientist Jayant Sirohi, Co-Advisor
Professor Roberto Celi
Professor Norman Wereley

This dissertation is dedicated to my Mother and Father.

ACKNOWLEDGMENTS

I would like to thank my advisor, Dr. Inderjit Chopra, for providing me with the opportunity to work under his direction. I would also like to thank the members of my examining committee, Dr. Norman Wereley, Dr. Roberto Celi and Dr. Jayant Sirohi for their time. I would like to express my sincere gratitude towards my co-advisor Dr. Jayant Sirohi for his guidance, advice and great help. He has been patient, extremely generous with his time and resourceful with his suggestions without which, this thesis would not have materielised. I owe a special thanks to Dr. Anubhav Datta for his great help, explanations and patience.

I would like to thank Dr. Marat Tishchenko for his great help and advice, Dr. V.T. Nagaraj for his advice, Dr. Jinsong Bao for teaching me blade manufacturing, Mr. Nitin Gupta for his help in the experimental testing, and Mr. Howard Grossenbacher for teaching me machining.

My deepest thanks to my family - my Father for all the drawings, my Mother for scanning and emailing them and my brother Vincent. They have supported me and provided encouragement and suggestions. I am also grateful to my friends, among whom Jayant, Renata, Vincent, Anne-Sylvie or Stéphanie, for all the discussions and support during difficult times. Finally, I would like to thank my three nephews: Marc, Benoît and Olivier for their smiles and "flying kisses from the other side of the sea", for they mean a lot to me.

I would like to acknowledge Mr. Seibert Murphy from Progeny Systems who provided the initial impetus for this research.

Finally, I benefitted greatly from my colleagues at the University of Maryland who have contributed to my learning experience: Ron Couch, Felipe Bohorquez, Dr. Karthikeyan Duraisamy, Dr. Manikandan Ramasamy, Shaju John, Eric Parsons, Maria Ribera, Carlos Malpica, Dr. Béatrice Roget, "the Bhaiyas": Sandeep Gupta, Abhishek, Arun Jose and Nitin Gupta. It is impossible to remember all, and I apologize to those I have inadvertently left out.

TABLE OF CONTENTS

LIST OF TABLES

LIST OF FIGURES

Nomenclature

A_{annul}	Area of a rotor annulus, m^2
a_{body}	Vertical acceleration of the system, ms^{-2}
AF	Aerodynamic force, N
c	Blade chord, m
C_d	Coefficient of drag, non-dimensional
C_{d0}	Zero-lift drag coefficient, non-dimensional
CF	Centrifugal force, N
CG	Center of gravity
C_l	Coefficient of lift, non-dimensional
$C_{l\alpha}$	lift-curve slope, rad^{-1}
CP	Center of pressure
dD	Elemental drag on a segment, N
dH	Local aerodynamic force parallel to disk plane, N
dL	Elemental lift on a segment, N
dQ	Elemental torque on an annulus, Nm
dr	Blade element width, m
dT	Elemental thrust on an annulus, N
dt	Time step duration, sec
dN	Local aerodynamic force normal to disk plane, N
e	Blade hinge offset, m
g	Acceleration of gravity, ms^{-2}
h	Altitude of the system, ft
I_{rotor}	Rotor moment of inertia about hub, kg/m^2
k_β	Flap stiffness of δ_3 hinge, Nm/rad
M_{AF}	Moment created by the AF, Nm
M_{CF}	Moment created by the CF, Nm
m_{blade}	Blade mass, kg
m_{seg}	Mass of a blade element, kg
m_{tot}	Gross weight of the system, kg
N_{b}	Number of blades on the rotor
N_{seg}	Number of segments on a blade
Q	Rotor torque, Nm
R	Rotor radius, m
r	Blade element radial coordinate, m
T	Rotor thrust, N
t	Current time, sec
U	Resultant velocity, $\sqrt{U_P^2 + U_T^2}$, m/s
U_T	In-plane velocity, m/s
U_P	Out-of-plane velocity, m/s
V_d	Descending velocity of the system, m/s
v_h	Hover induced velocity, m/s
v_i	Induced velocity, m/s
W	Weight of the Autobody, N
α	Angle of attack, deg
β	Flap angle, deg
β_p	Precone angle, deg
δ_3	Pitch flap coupling
θ	Blade pitch angle, deg

θ_0	Initial collective pitch angle, deg
θ_{TW}	Twist rate of the blade, deg/ft
ρ	Air density, kg/m^3
ϕ	Inflow angle, deg
ψ	Blade azimuth angle, deg
Ω	Rotor rotational speed, rpm

Chapter 1

Introduction

Autonomous unmanned aerial vehicles (UAVs) find numerous applications in hazardous civilian and military environments. The military may use UAVs for aerial reconnaissance and surveillance of enemy territory without endangering human lives. Furthermore, UAVs find their niche in traffic monitoring, hostage crisis and search and rescue operations in urban scenarios. Because of these advantages there has been considerable interest in the design and development of versatile, cost-effective, autonomous UAVs, which are capable of deploying electronic instruments on ground from conventional aircraft. The vehicle is required to decelerate the payload, causing it to descend at an acceptable velocity and also to minimize the impact upon landing to avoid damaging the sensitive electronic equipment on-board.

1.1 Objectives

A delivery system called the Autobody is envisaged to safely deploy a payload dropped from an aircraft. The vehicle must be capable of safely delivering the payload at a low descent velocity. The main feature of the Autobody is an autorotative rotor to produce lift, thus eliminating the need for an on-board engine. The objective of the present study is to design a passively controlled, autorotative rotor. Furthermore, it is desired that the Autobody has no active controls to keep the mechanical complexity and weight to a minimum. This allows for a light weight compact vehicle.

Conventional piloted helicopters enter into autorotation in case of engine failure. The rotor initially has a fixed rotation speed that starts decreasing as soon as the engine fails. A key function of the pilot during autorotation is to ensure that the rotor speed does not decrease below a certain acceptable value. This is achieved by lowering the collective pitch till the rotor speed reaches a steady value. Flying in this state requires constant pilot inputs to control the blade pitch and therefore the rate of descent.

In the case of the Autobody, the rotor starts from rest. A negative blade collective pitch is necessary to initiate the rotation in the correct direction, i.e. leading edge first. However, as the rotor picks up speed, a negative collective pitch would result in a low thrust, which would give rise to a high rate of descent of the payload. To increase the thrust and reduce the rate of descent to an acceptable value, the negative blade pitch needs to be progressively reduced or even made positive during the descent. To keep the vehicle fully autonomous and the design simple, the Autobody should be equipped with a passive mechanism to achieve such a pitch variation.

A theory will be developed to predict the steady state behavior of the system. Wind tunnel tests will be then performed to validate the analysis. Once the theory has been validated, it will be used to design an optimum rotor geometry that will allow for a low rate of descent, and produce an optimized thrust and rotational velocity. Finally, the optimum design will be validated by flight tests on an instrumented prototype.

1.2 Why an autorotative rotor?

An autorotative rotor was preferred over other decelerating devices, such as a parachute, for several reasons (Ref. [1]):

1. The autorotative system is lighter.
2. It provides vehicle stabilization throughout the flight.
3. It eliminates the sudden deceleration during deployment, smoothening out the descent flight.
4. Once deployed, power had to be provided to the on-board instrumentation. For this reason, an autorotative rotor with embedded solar cells on blades may be used.

1.3 Operational requirements

The envisaged vehicle must follow certain design specifications as a result of operational constraints imposed by the specific deployment scenario:

1. A five-pound maximum gross weight.

2. A four-bladed rotor of four-foot diameter.

3. Completely passive deployment to keep the system complexity to a minimum.

These were the basic constraints that the Autobody design need to follow.

1.4 State-Of-The-Art

The following sections will describe the state-of-the-art of analysis in the autorotation flight regime, the autogyro, autorotative vehicles dropped from an aircraft, and re-entry vehicles equipped with autorotative rotors.

1.4.1 Autorotation flight regime

The state of autorotation is characterized by the net torque on the rotor shaft being zero. The energy to drive the rotor comes from the airstream flowing through the rotor. Autorotation is well known as a means of helicopter recovery in case of engine or tail rotor failure. Several authors have discussed the phenomenon of steady autorotation (Refs. 2–5). Autorotation normally occurs in the turbulent wake state. In this operating state, the descent velocity ratio is such that momentum theory is not strictly valid. Therefore, the state of autorotation is usually predicted by semi-empirical models based upon experimental data.

1.4.2 Autogyro

The autogyro is essentially an airplane with a rotor installed on top of it. The main rotor is unpowered and can turn freely in autorotation thus eliminating the need for a tail rotor. The rotor generates the lift required to support the aircraft. An engine and a propeller are installed at the nose of the aircraft to produce the forward thrust. The vehicle is also equipped with two wings on either side of the fuselage and with a horizontal stabilizer at the tail (Figure 1.1) to provide stability and control. The autogyros were quite popular in the $1920s$ and $1930s$ and many flying aircrafts were then built. During the development of autogyros, engineers came across numerous technical challenges that were resolved over a period of time:

(**a**) Cierva C-4 (**b**) Cierva C-30 (**c**) Weir W.5

Figure 1.1: Early autogyros.

1. First autogyros did not feature flap hinges, leading to many crashes. However, the C.4 (Figure 1.1), built by de la Cierva in 1923, overcame this problem through the incorporation of a blade flap hinge and flew successfully (Ref. [6]). Each retreating blade could therefore flap downward as the advancing one's flapped up, so that the lift forces were in balance and prevented the aircraft's tendency to become unstable and roll over while in forward flight.

2. Early autogyros also did not have collective pitch control. However, the autogyro built by Kay in 1934, introduced the first practical application of collective pitch control. In 1935, Hafner flew the first combined cyclic-and-collective control system on an autogyro with articulated blades (Ref. [6]). The W.5, developed by Weir group, flew in 1939. This two-seater autogyro was powered by a powerful fan-cooled engine located in the nose. Each of the two rotors had three blades made of compressed wood with metallic leading edges (Figure1.1). They had both cyclic and collective control all enclosed within the hub (Ref. [6]).

3. In addition to pitch control, direct rotor control was implemented on the C.30 built by de la Cierva (Figure 1.1). The rotor control was provided by means of a column suspended from the head of the pylon which acted directly on the rotor head to tilt it to produce the desired maneuver (Ref. [6]).

4. A breakthrough was made in 1936 when the W.3, built by Weir group, performed a 'jump take-off' (Ref. [6]). The vehicle was equipped with a two-bladed 'auto-dynamic' rotor. The jump take-off was achieved by running the rotor at an overspeed at zero pitch and then giving

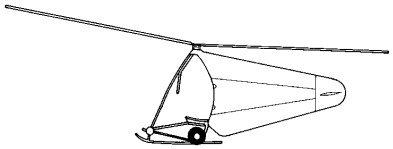

Figure 1.2: Side view of the Rotachute 1942

a sudden sufficient positive pitch to produce the jump, after declutching the engine.

As many improvements were introduced in autogyro's design, these systems were widely used and considered to be safe vehicles. The rotor hubs were generally complex and had all the features that are present in modern helicopters.

1.4.3 Autorotative vehicle dropped from an aircraft

The concept of an autorotative vehicle dropped from an aircraft has been previously explored by several researchers.

Rotachute

In 1943, Hafner and the staff of the Airborne Forces Experimental Establishment developed an autogyro glider called the Rotachute (Ref. [6]). It was intended to deploy an armed soldier on ground from a large transport aircraft. The Rotachute (see Fig.1.2), consisted of a soldered steel tube framework, carrying the rotor and having its rear part covered with rubberized fabric in which there were two small vertical shutters. The vehicle height was 2.08 m and its gross weight was 134 kg. The rotor had two wooden blades articulating on the hub by means of steel hinges. The rotor diameter was 4.57 m. The hub was attached to a small upright component by a rubber block acting as a universal joint, so that some vertical displacement could occur but vibrating loads from the rotor were dissipated before transmission to the main structure. The rotor controls operated in the opposite way from those on an aircraft. To raise the nose, the control column was pushed forward; to bank to the right, the column was moved to the left. The soldier being deployed had the additional responsability of piloting the vehicle. The undercarriage originally consisted of two main wheels joined by an axle and placed almost directly below the rotor. Following towing tests

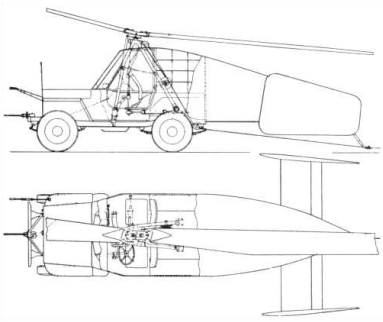

Figure 1.3: Two views of the Hafner's "Rotabuggy" 1943

behind a car, changes were made and a skid was added in the Mark 2. Further tests resulted in the Mark 3, a version of greater length and with a rigid tail. This final prototype was extensively towed by a Tiger Moth.

Rotabuggy

The rotorcraft team of the Airborne Forces Experimental Establishment (AFEE), headed by Hafner, had enjoyed some success in developing the Rotachute, and this led to the suggestion that the principle could be applied to a larger system. This prompted Hafner to propose the Rotabuggy, a rotor-equipped Jeep, and the Rotatank, a similarly-equipped Valentine tank (Ref. [6]). The first trials connected with the development of the Rotabuggy (see Fig.1.3) consisted of loading a Jeep with concrete and dropping it from heights up to 2.35m to ascertain the amount of impact that could be absorbed without incurring damage. It was found that 11g impact could safely be accepted. A two-bladed rotor with a diameter of 12.40m, a streamlined tail fairing, tailplane, twin fins (no rudders), a "hanging" control column, a rotor tachometer and glider navigational instruments were mounted on the test model. The Rotabuggy was first towed along the runway at high speed behind a car. The Rotabuggy became airborne for the first time on 16 November 1943, attaining towed airborne speeds up to 105 km/h. Eventually, the Rotabuggy was towed into the air behind a Whitley in which several issues were discovered with the control system, requiring the pilot to exert all his strength to maintain control. The initial problems were progressively ironed out, and the general handling and flying qualities of the Rotabuggy were eventually described officially as

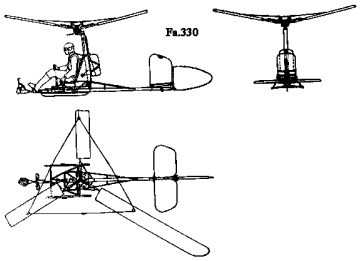

Figure 1.4: Three views of the Focke-Achgelis Fa-330 1942

"highly satisfactory", but the availability of vehicle-carrying gliders rendered further development unnecessary. The Rotabuggy had a gross weight of 1411 kg of which 964 kg was the empty weight of the Jeep and 249 kg the weight of the rotor unit and tail. The designed maximum speed was 241 km/h, and estimated rates of descent ranged from 4.9 m/s to 10 m/s. The minimum take-off and landing speed was 58 km/h and maximum sea level rotor speeds were 230 and 260 RPM.

Focke-Achgelis Fa-330 – 1942

This rotorcraft (see Fig.1.4) was flown as a kite towed by a submarine from a cable of 60 to 150 meters in length. The collapsible assembly was made of steel tubes and a pylon located behind the pilot's seat provided support to the rotor. The rotor hub was of the simplest possible autogyro type with flapping and drag hinges. The rotor was set in motion by a rope or by hand push, as long as there was sufficient wind velocity. To bring the autogyro back to the ground, the towing rope was pulled in by a winch which facilitated the landing of the aircraft. The rotor was stopped using a brake. The rotor blades were folded and the whole aircraft was finally stored in the submarine. By the end of World War II, some 200 of these small, motorless, three-bladed autogyros had been built for Focke Achgelis by the Weser Flugzeugwerke at Delmenhorst [6].

Autorotor

In 2003, Bartz and Miklosovic investigated the effect of airfoil camber on the autorotative and deceleration performance of an Autorotor (Ref. [7]). The Autorotor was to be dropped from an aircraft to deliver supplies to ground troops. It was equipped with 4 inch by 0.5 inch controllable

outboard flap which would allow for precise and controllable flight trajectory. The rotor tested was six-bladed with a diameter of 23.5 inches. The blade airfoil was symmetric and the blade chord was of 1.969 inches. The flaps were attached to the trailing edge of each blades. The wind tunnel tests were performed for airstream velocities from 20 ft/sec to 60 ft/sec, Reynolds numbers up to $7 * 10^6$ and flap angles from 0° to 8°. A 4% camber configuration was found to produce the highest drag and a maximum uncorrected drag coefficient of 2.798. A 2% camber configuration gave the highest RPM and lowest advance ratio. It was also observed that the drag coefficient increased with higher Reynolds numbers. A larger scale Autorotor would be expected to operate at higher Reynolds number. The controllable flaps could alter the geometry throughout the descent profile of a vehicle eqipped with the Autorotor, therefore the magnitude and direction of the deceleration vector could be manipulated to control precisely the trajectory of the vehicle.

1.4.4 Re-entry vehicles

Spacecraft Rotor Landing System

In 1959, Ref. [8] presented a preliminary experimental study of a model spacecraft rotor landing system. The tested rotor was supposed to be mounted on a spacecraft to lower the vehicle rate of descent during the re-entry from a supersonic speed to a subsonic autorotative glide. The rotor was three-bladed and had a 6-foot diameter. The blades were 3-inch in chord with a double wedge airfoil. Each blade was free to flap from 0° to 80°, but the flap angles of all blades were maintained identical. The blade collective pitch was controlled to vary between $-21°$ and 40°. The model was tested by mounting it on a frame on a truck. Blade angles and thrust were measured and recorded and the bottom surface of the blades faced forward velocities from 20 to 50 mph. The RPM was stable in the stalled region below tip speed to velocity ratio of 3 as well as thoughout the unstalled region. However, RPM instability was observed between stalled and unstalled region.

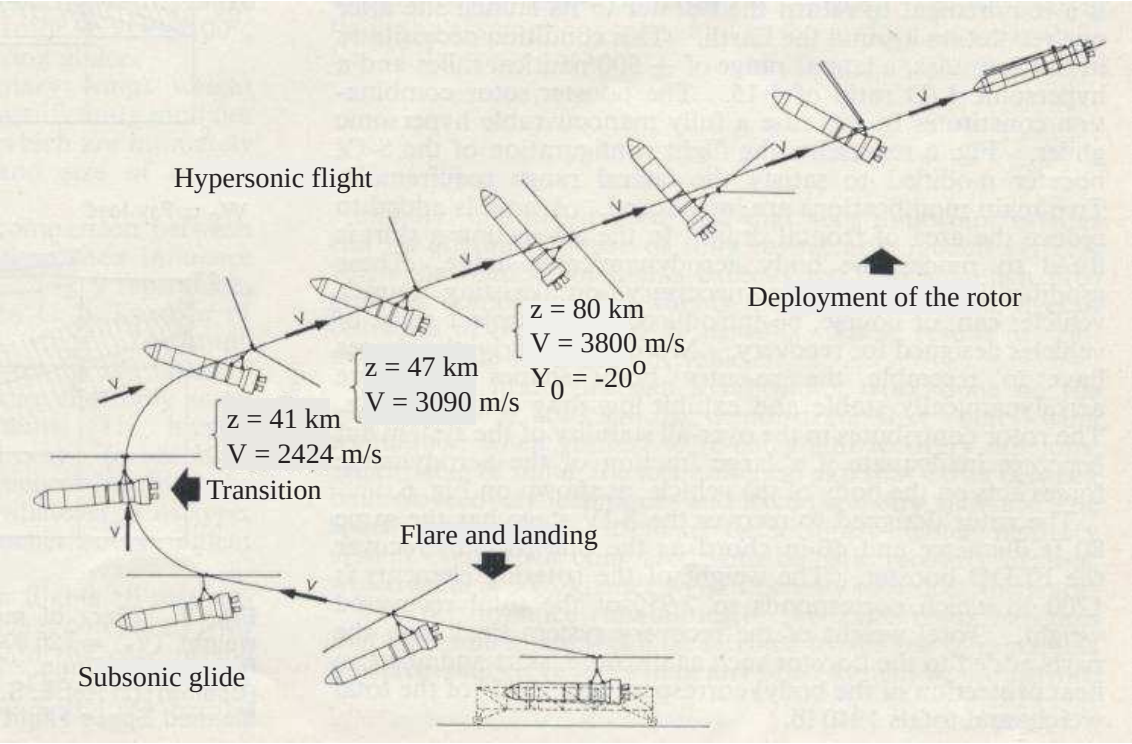

Figure 1.5: Vehicle ballistic flight path and deployment of the Space Rotor (Ref.[9]).

Space Rotor

The Space Rotor was developed by Kretz from Giravions Dorand Company in 1966. It was envisaged that space vehicles would be equipped with the Space Rotor in order to slow down their flight back to earth. The Space Rotor increased their flight stability and lateral range and allowed the vehicle to land softly at a precise location making the launcher reusable (Ref. [9]). The Space Rotor blades were 40 ft long and 40 inches in chord. The blades were attached by a suspension system to the launcher and were folded along the fuselage of the vehicle during the launch (see Figure 1.5). The whole reentry maneuver was automatic. During the reentry, the rotor was deployed in a state of weightlessness. The blades, set slighly apart, increased the vehicle stability. When the dynamic pressure was sufficient, the blade pitch was changed automatically as the rotor spun up. During the transonic flight, the launcher's fuselage orientation with respect to the relative wind changed: its engines were forward. This further increased the flight stability. Autorotation was achieved during the subsonic part of the flight.

Unpowered Rotor Re-Entry Vehicle

In 1968, Levin and Smith discussed an analysis of the aerodynamics and performance characteristics of re-entry launcher equipped with unpowered rotor similar to the Space Rotor (Ref. [10]). The aerodynamic characteristics of a rotor alone and of a rotor/launcher assembly were invertigated to determine what type of gains in performance could be achieved with the rotor. This analysis was based on blade element theory without small angle assumption so that angles up to 90° could be considered. A rotor in descent with some forward speed was studied. The autorotative equilibrium condition was zero net rotor torque coefficient. Ref. [10] showed that the rotor had a stable operating range at low blade pitch angles. In axial flight, a precise control of the blade pitch angle was essential to avoid overspeeding since the RPM was very sensitive to a small change in blade pitch angle.

In 1969, Levin and Smith also presented the results of wind tunnel tests conducted on an unpowered rotor for Mach numbers from 0.10 to 3.54 at angles of attack from 15° to 90° (Ref. [11]). Several collective (±20°) and cyclic pitches (±10°) were tested. The collective and cyclic pitch angles were changed remotely. The blades were free to flap. The rotor was four-bladed with a diameter of either 45 inches or 60 inches. The blade airfoil was chosen to minimize the aerodynamic heating at hypersonic speeds.

Roton

The Roton was a completely reusable space vehicle developed by Rotary Rocket Company (Ref. [1]). It could deliver a payload of $7,000$ lbs to low earth orbit (L.E.O.). It could takeoff vertically like a rocket under the control of a crew and fly to low earth orbit. The Roton used a similar concept as the one developed by Kretz to lower its rate of descent during re-entry. But unlike the Space Rotor, the Roton featured a nose mounted rotor. During the launch, the blades were folded down along the fuselage of the Roton. Before the re-entry, the blades were deployed and angled upward. During the hypersonic and supersonic part of the flight, the rotor was windmilling, thereby stabilizing the vehicle until it reached subsonic speed. At that point, the rotor was spun up and entered

autorotation. The pilot could land at a precise location.

1.5 Contribution of the present work

Most of the concepts mentioned in the previous section, while being innovative, were actively controlled : the autogyros, the Rotachute, Rotabuggy, Fa-330 and Roton were piloted and the Autorotor featured actively controlled flaps. It was the case with the Bell Spacecraft Rotor Landing System, the Space Rotor or the Unpowered Rotor Re-entry Vehicle. The Autobody, however, is desired to be fully autonomous and passive. No pilot inputs, actuator or engine should be incorporated to change the blade pitch for instance. In addition, the rotor of the Autobody must be used throughout the flight unlike the Space Rotor which operates only during the subsonic part of its flight.

Although the steady state of autorotation is well documented and understood, there is little data on rotors starting from rest and experiencing a transient state before reaching autorotation. A theoretical study of the feasibility of a fully autonomous, autorotative system with no active control systems on-board was performed by Sirohi et al [12]. This study proposed a rotor with a negative precone and a negative pitch-flap δ_3 coupling to achieve the required change in collective pitch in flight. The rotor started from rest and underwent a transient state before reaching the autorotation condition. While the basic concepts for an efficient autorotating system including transient state and steady autorotation state were discussed in Ref. [12], the theoretical analysis needed to be refined and validated with wind tunnel data and flight test data. The study was not conclusive and an optimum configuration of the vehicle could not be determined.

The present work consists of:

1. The design of an autorotative rotor with completely passive operation.

2. The development of a theory to predict the steady state of autorotation.

3. Wind tunnel tests and validation of this theory.

4. The definition of the optimum full scale design using the theory.

5. Instrumental flight tests and validation of this design .

1.6 Thesis outline

This thesis is composed of six chapters. A brief description of the chapters follows:

1. **Chapter 1 : Introduction**: A description of the problem statement, the previous work on the topic and the contribution of the present work is presented.

2. **Chapter 2 : Physical principles**: This chapter deals with the physical principles involved in autorotation and to initiate a rotor rotation in the correct direction. The functioning of an innovative hub design to increase the thrust produced is described.

3. **Chapter 3 : Analytical model**: The development of a steady state analysis using two different approaches is presented. Several challenges to implementing the first model are overcome in the refined second model. The model predicts the behavior of the system when it has reached its equilibrium conditions.

4. **Chapter 4 : Wind tunnel tests**: This chapter presents the small scale model which was manufactured and tested in the wind tunnel. Wind tunnel tests are conducted to validate the analysis. Their results and the corresponding analytical predictions are compared and discussed. Once the analysis is validated, a parametric study is carried out to minimize the rate of descent of the Autobody.

5. **Chapter 5 : Full scale flight tests**: The full scale prototype construction is presented. The settings of the hub parameters are obtained from the validated analysis. The set-up, instrumentation and results of the flight tests are discussed. The experimental data are then compared with the analysis predictions.

6. **Chapter 6 : Conclusions and Future work**: Important conclusions are drawn from the presented results and lead to future work suggestions to improve the design of the Autobody.

Chapter 2

Physical Principles

2.1 State of autorotation

In the event of power or tail rotor failure, a helicopter must enter in autorotation to ensure a safe landing. When the rotor operates in this state, the net rotor torque is zero. During the descent, the energy to drive the rotor comes from the airstream. In other words, the pilot adjusts control to achieve descent at a controlled rate, to keep the rotor RPM acceptable and avoid an unsafe landing.

Figure. 2.1 shows that the torque is normally zero at two stations on the blade during the descent in autorotation. At these stations, the horizontal component of the elemental lift dL_x and drag dD_x are equal and opposite, therefore their resultant is zero. On the remaining blade segments, the torque can be positive or negative (Figure. 2.1). Depending on the inflow angle ϕ, the magnitude of dL_x and dD_x will vary. Therefore the magnitude and orientation of their resultant dF_x and the local torque depend on the inflow angle. Portions of the blade thus extract power (driving regions) whereas others consume power (driven regions) so that the net rotor torque at the shaft is zero (Figure. 2.1).

If the autorotation is performed with some forward speed, the axial symmetry of the induced

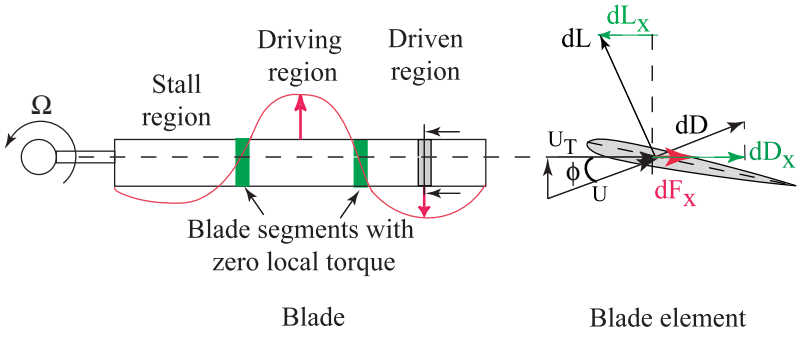

Figure 2.1: Driving and driven regions on a blade (Advance ratio $\mu = 0.$)

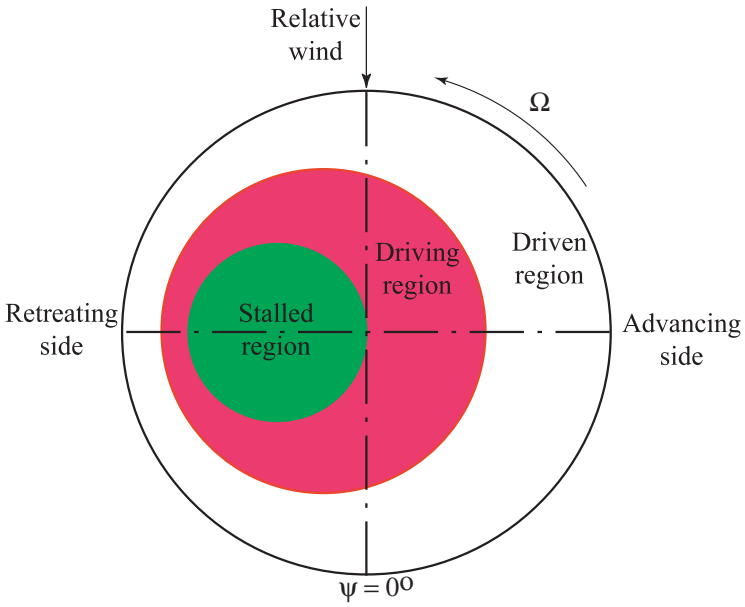

Figure 2.2: Rotor autorotative power distribution with forward speed.

velocity and angle of attack over the rotor is lost (Ref. [2]). Instead, the driving and driven regions are shifted towards the retreating side (Figure. 2.2).

The steady state autorotation of a helicopter rotor is well documented (Refs. 2–5). However, the rotor aerodynamics can be described using Momentum Theory when the rotor is in climb or steep descent. For the climb case, velocity ratios are $\frac{V_c}{v_h} > 0$ and for steep descent, velocity ratios are $\frac{V_c}{v_h} < -2$ (Figure 2.3). V_c and v_h are respectively climb velocity and hover induced velocity. When $\frac{V_c}{v_h} < -2$, the rotor is said to operate in Windmill Brake State. In the range $-2 < \frac{V_c}{v_h} < 0$, momentum theory is not valid because the direction of the flow through the rotor is not well defined. The ideal autorotation occurs in Turbulent Wake State (Figure 2.3) at a climb velocity ratio $\frac{V_c}{v_h}$ of -1.85 approximately (Ref. [2]). When a rotor operates in autorotation state, its aerodynamics cannot be described by a classical theory. Instead, it is defined by semi-empirical models based on experiments (Ref. [13]).

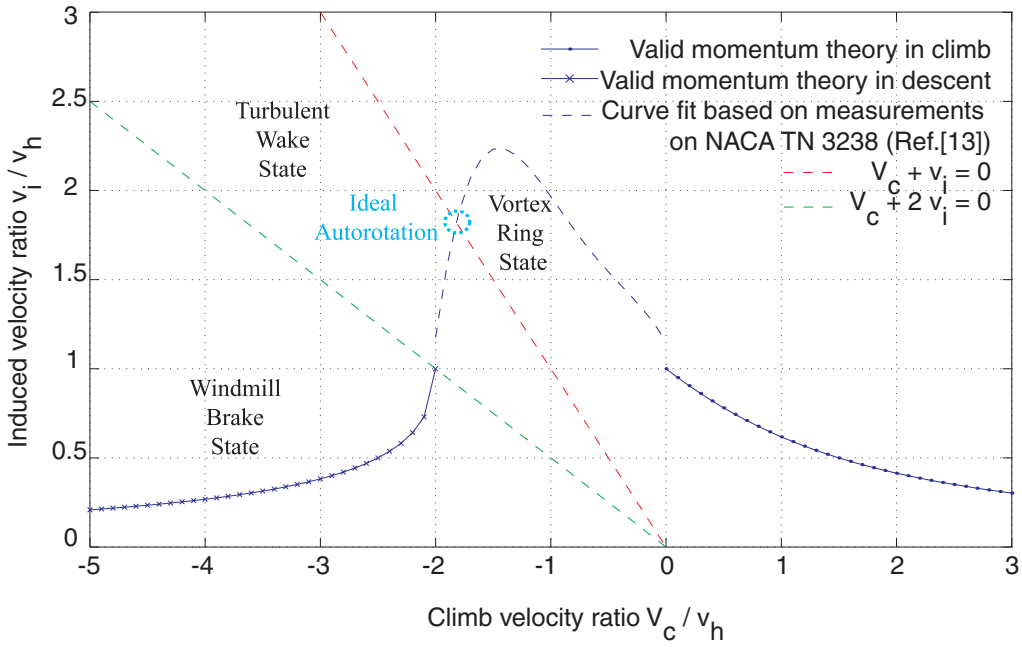

Figure 2.3: Domain of validity of momentum theory. Curve fit for $-2 < \frac{V_c}{v_h} < 0$ is obtained from Ref.[13].

2.2 The Autobody case

In the case of the Autobody, the rotor is initially at rest. The main challenges is to start the rotor rotation in the correct direction (i.e. leading edge first) and to produce enough thrust to arrest the rate of descent of the Autobody.

As mentioned above, the Autobody rotor starts from rest. Therefore, it experiences a significant transient regime before reaching its steady state equilibrium condition. Several important aspects must be considered to understand the transition from rest to steady autorotation. First, the rotor rotation needs to be initiated in the correct direction. Second, as the system descends, the rotor spins up and has to produce enough thrust that must support the gross weight of the system in steady state. Third, the rate of descent should be as low as possible to permit a safe landing. The rotor is therefore required to :

1. Start spinning in the correct direction, i.e. leading edge first.

2. Produce as high steady state thrust as possible.

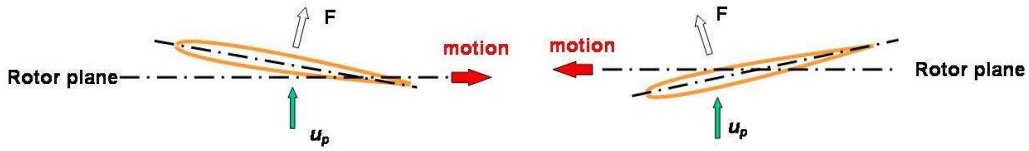

(a) (b)

Figure 2.4: Effect of the root collective pitch on the direction of rotation.

Depending on the initial blade pitch, the forces acting on the rotor blades as it starts from rest are shown in Figures. 2.4(a) and 2.4(b). Just after the vehicle is released, the rotor rotational speed (RPM) and in-plane velocity of the blades, U_T are equal to zero. A small out-of-plane velocity, U_P is present, and is equal to V_d, the descending velocity of the system. If the blade is set at a positive pitch, the air flows towards the leading edge of the profile, creating a force F as seen in Figure 2.4(a), with an in-plane component acting towards the trailing edge. This causes the rotor to start rotating trailing edge first. If the blade is set at a negative pitch, as shown in Figure 2.4(b), it ensures that the flow is directed towards the trailing edge, generating a force F which gives rise to a rotor rotation in the direction of the leading edge. Therefore a negative collective pitch at the blade root allows the rotor to spin up in the appropriate direction: leading edge first.

However, a negative pitch would result in a low steady state thrust. Therefore, to obtain a high steady state thrust, the steady state pitch should be less negative or slightly positive. The rotor pitch settings required to start the rotor rotation in the correct direction and to generate a high steady state thrust are therefore contradictory.

To achieve this increase of pitch from rest to steady state in a completely passive manner, it is proposed to incorporate a negative pitch-flap coupling at the blade hinge. This coupling can be achieved by incorporating a flap hinge with a negative δ_3 angle as shown in Figure. 2.5. As a result, as the rotor RPM increases, a positive change of flap angle will result in an increase of pitch.

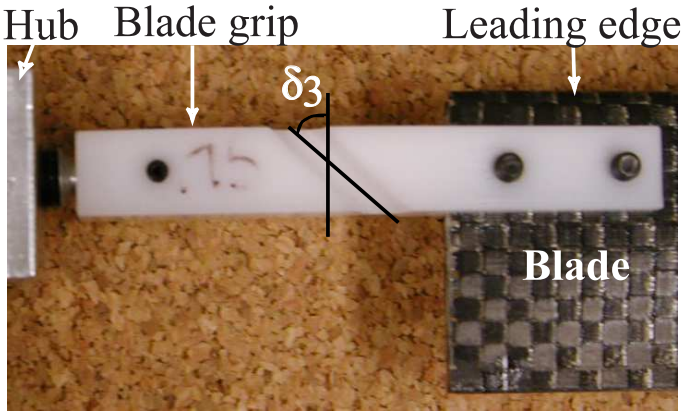

Figure 2.5: Close view of the blade grip with the δ_3 hinge.

The effect of the flap angle β and precone β_p can be seen from the pitch-flap coupling relation:

$$\begin{aligned} \Delta\theta &= -\Delta\beta \ \ tan(\delta_3) \\ &= -(\beta - \beta_p) \ \ tan(\delta_3) \end{aligned} \tag{2.1}$$

where $\Delta\theta$ is the change in pitch angle and $\Delta\beta$ the change in flap angle. It follows that it is necessary to generate a large flap deflection in order to obtain large increase in pitch and thereby a high thrust. Flap deflection is given by :

$$\begin{aligned} \Delta\beta &= \beta - \beta_p \\ &= \frac{M_\beta}{k_\beta} \end{aligned} \tag{2.2}$$

where k_β is the flapping stiffness of the hinge and M_β the flapping moment about the flap hinge. The flapping moment about the flap hinge is the sum of the aerodynamic moment M_A and centrifugal moment M_{CF}. It is noted that introducing a negative precone angle β_p helps to generate a larger flap deflection as shown in Figures 2.6(a) and 2.6(b). In Figure. 2.6(a), the blade precone angle is negative. In this case, the aerodynamic and centrifugal moments add up, generating a large flap deflection of the blade upward. On the contrary, a positive precone β_p, as shown in Figure. 2.6(b), will result in the centrifugal moment impeding the action of the aerodynamic moment. In this case, the flap deflection of the blade is lesser than with a negative angle.

Therefore the final hub design incorporates the following features:

1. A negative collective pitch angle θ_0 to initiate the rotation in the correct direction (Fig-

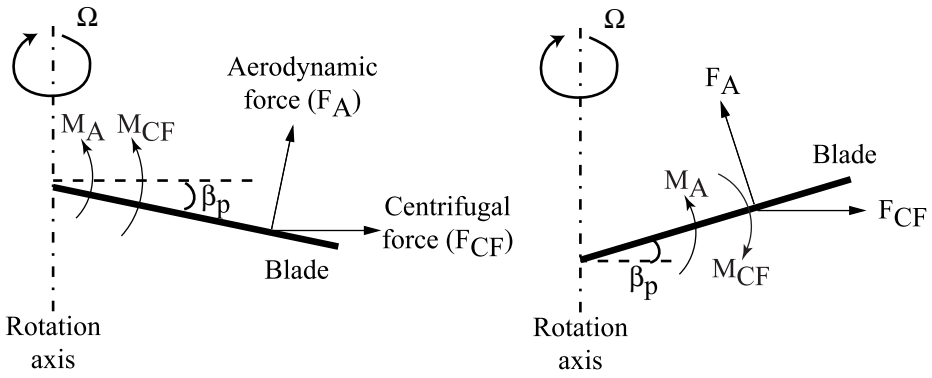

(a) (b)

Figure 2.6: Effect of the precone angle β_p on the flap deflection.

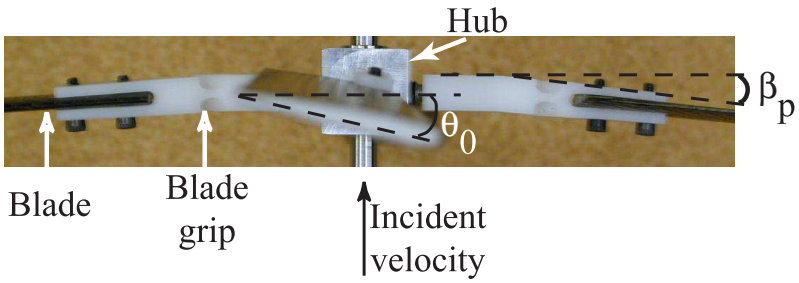

Figure 2.7: Close view of the hub with the negative root pitch angle, θ_p, and the negative precone angle, β_p.

ure. 2.7).

2. A negative δ_3 angle to convert the flap deflection to an increase of pitch in order to obtain higher steady state thrust (Figure. 2.5).

3. A negative precone angle β_p to allow a large flap deflection (Figure. 2.7).

To further increase the amount of lift generated by a blade, the blades incorporate a positive twist. This results in a higher angle of attack at the blade tip during steady state, increasing therefore the steady state thrust. It is well known from basic momentum theory that positive twist (nose up) improves autorotative performances (Ref. [4]).

The sequence of events is as follows :

1. While descending, the rotor speeds up leading to an increase in lift and centrifugal load on each blade.

2. As a result, the blade flaps up, which because of the δ_3 coupling, results in an increase in pitch.

3. This causes a further increase in the lift and torque on the rotor.

4. The rotor RPM increases continuously until the equilibrium condition is reached, which is indicated by a constant RPM and a zero net rotor torque [[3, 4]].

In this manner, a passive increase in the rotor collective pitch, and a transition to a state of steady autorotation is achieved.

Chapter 3

Analytical models

Two analytical models of the Autobody are presented in this chapter. The aim of the analysis is to predict the rotor thrust and RPM when it has reached the steady state of autorotation. The analysis is validated with experiments performed on a model scale rotor in a wind tunnel and is used to design a full scale prototype. Details of the validation are presented in Chapter 5. The final goal of this analysis is to develop tools to design an optimum rotor geometry for minimizing the drop height and the descent velocity of the Autobody. The two analytical models described in this chapter are :

1. Time Marching Method: The rotor starts from rest at $t = 0$. The torque is calculated at each time step until it converges to zero. At this final time step, the steady state of autorotation has been reached.

2. RPM Sweep Method: A range of RPM is chosen. For each RPM, the rotor thrust and torque are calculated. When the net rotor torque is zero, it is assumed autorotation has been reached and the calculations are stopped. The value of thrust at this RPM is the steady state thrust attained in autorotation.

3.1 Time marching study

A combined blade element momentum theory (BEMT) analytical model in autorotation flight, developed in Ref. [12], was extended to study the effects of various control settings and flight parameters on the system behavior during steady flight. The model predicts the steady values of the thrust, the RPM, the rotor torque, the descending velocity and the total height needed to stabilize the descent speed of the vehicle.

The development of the analysis was based on the following assumptions:

1. A quasi-steady blade element momentum theory is used to determine the rotor aerodynamic loads.

2. The coefficient of lift, C_l and the coefficient of drag, C_d of the airfoil are obtained from SC1095 airfoil look-up tables.

3. The blade is considered rigid with a flap degree of freedom at the δ_3 hinge and undergoes pitching motion because of the δ_3 pitch-flap coupling.

4. The system is assumed to fall vertically without tilting, thus the flow is assumed to be purely axial.

5. The effect of altitude is not taken into account, only sea level conditions are considered.

Several parameters of the system were set by operational constraints:

1. The full-scale vehicle was required to have a four-bladed rotor of diameter 4 ft.

2. The gross weight of the vehicle was 5 lbs.

3. Based on the availability of a mold to manufacture the blades in-house, the blades were chosen to have a SC-1095 airfoil, 3 in chord and $0.38°/in$ blade twist rate.

The hub and grip design established respectively the precone β_p and δ_3 angles. The blade mass was defined by the mold dimensions and the manufacturing process.

The analysis consists of a time stepping procedure where the forces on the rotor and on the vehicle are calculated at each instant of time until autorotation is reached. To this end, each blade is divided into N_{seg} elements, at which the aerodynamic quantities are evaluated. At the end of each time step, the angle of attack at each blade element, and velocity of the vehicle and rotor are updated. The calculations continue until the torque on the rotor becomes zero. Each time step can be divided into the following four stages:

(i) The rotor geometry and flight parameters are input to the code.

(ii) Initial conditions: the velocity of the vehicle, rotor RPM, pitch angle of each blade element and other rotor parameters such as flap angle are provided.

(iii) Calculation of aerodynamic forces: The angle of attack at each blade element is calculated from the initial conditions. The total thrust and torque on the rotor can then be computed, from which the rotor inflow is obtained. Using the rotor inflow velocity, the angle of attack at each blade element is modified, yielding a new value of thrust and torque. This procedure is iterated till converged values of angle of attack, thrust, flap angle and rotor torque are obtained.

(iv) Check for autorotation : At this stage, the rotor torque is evaluated to check if the steady state of autorotation has been reached. If the torque is non-zero, the calculation proceeds to the next time step : the rotor torque and thrust are used to calculate new values of descending velocity V_d and RPM Ω for the next time step.

The algorithm for the analysis is shown as a flowchart in Figure 3.1, and each step is explained in detail below.

3.1.1 Step 1 : Inputs

The rotor geometry data, such as the chord length, and the number of blades, as well as the flight condition, such as the air density, are provided.

3.1.2 Step 2 : Initial conditions

As mentioned previously, the rotor is initially at rest (i.e. at time $t = 0$). The state of the rotor is then characterized by :

1. Zero RPM.
2. Zero rotor aerodynamic forces.
3. Zero rotor torque.
4. Zero in-plane velocity U_T and out-of-plane velocity, U_P.
5. Initial height is chosen as zero.

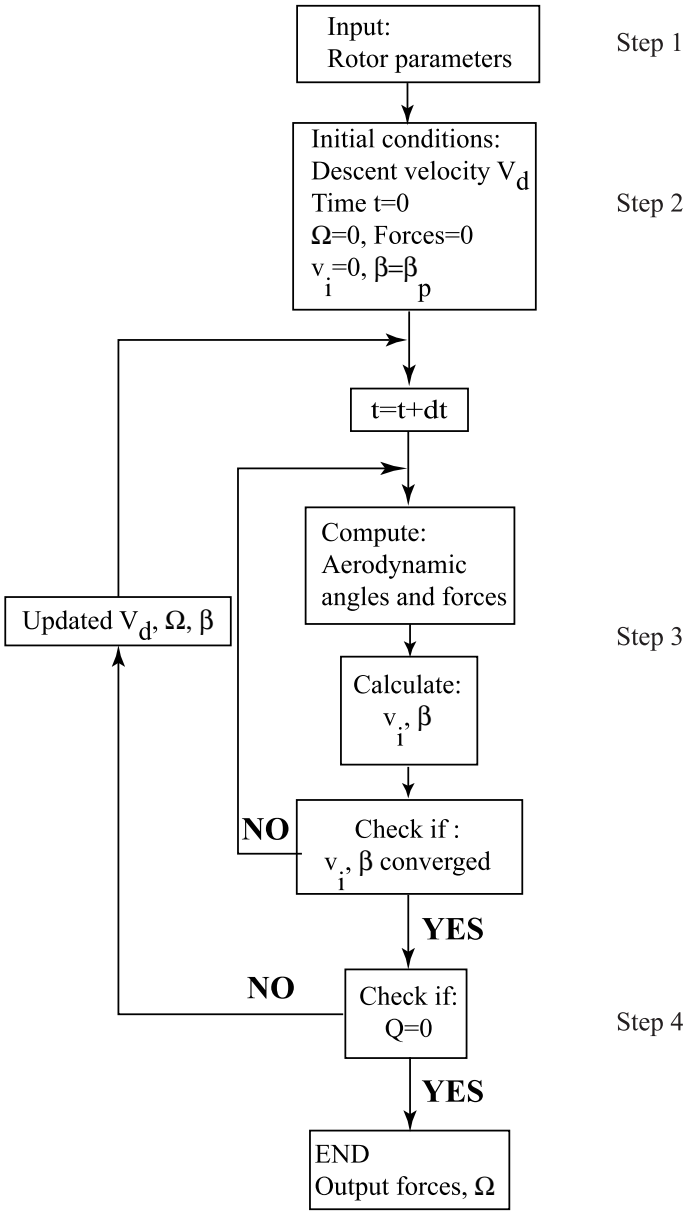

Figure 3.1: Algorithm flowchart of the vehicle time response when released from an altitude.

6. Initial flap angle is equal to the precone β_p.

The spanwise pitch angle depends on the initial pitch θ_0, the twist rate θ_{TW} and the change in pitch $\Delta\theta$ generated by the pitch-flap coupling. At any given time t, the pitch angle at any spanwise location θ_n is:

$$\theta_n = \theta_0 + r_n\,\theta_{TW} + \Delta\theta(t) \tag{3.1}$$

where r_n is the non-dimensional spanwise location of the n^{th} blade element, given by $r_n = y_n/R$, with R the rotor radius. Change in pitch occurs when there is a change in flap angle:

$$\Delta\theta = -\tan(\delta_3)\Delta\beta \tag{3.2}$$

As soon as the vehicle is released from rest, it accelerates under the influence of gravity. After one time step of Δt seconds, the value of U_p is the same as the downward velocity. This is given by:

$$V_d = g\ \Delta t \tag{3.3}$$

where g is the acceleration due to gravity. Because the rotor RPM is still zero, the initial angle of attack is nearly $-90°$. The flap angle is the same as the precone. The conditions that are specified in this stage are :

1. The vertical velocity of the vehicle.
2. The rotor RPM.
3. The blade flap angle.
4. The pitch angle.

3.1.3 Step 3 : Calculation of aerodynamic forces

Based on the four initial conditions obtained from the previous time step, the computation of the aerodynamic quantities are performed. The velocities and angles at the airfoil section are shown in Figure 3.2. Based on the blade flap angle, the pitch-flap coupling, and the blade twist rate, the pitch angle θ is calculated at each blade element. To determine the angle of attack α at each blade

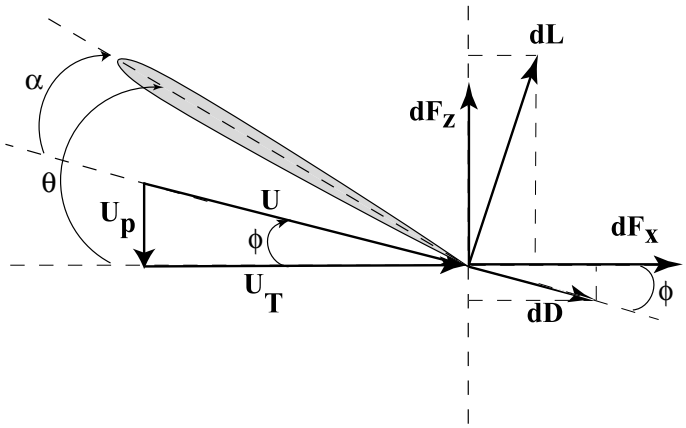

Figure 3.2: Incident velocities, aerodynamic angles and forces on a blade element.

element at a given time step, the in-plane and out-of-plane velocities are required. The in-plane velocity is given by:

$$U_{T,n} = \Omega \, r_n \tag{3.4}$$

where Ω is the rotational velocity and $U_{T,n}$ is the in-plane velocity at the n^{th} blade segment. The out-of-plane velocity is obtained from the induced velocity and the descending velocity (Figure 3.2). If the vertical axis is positive downwards, the out-of-plane velocity is given by :

$$U_{p,n} = v_{i,n} - V_d \tag{3.5}$$

where V_d is the descent velocity and v_i is the inflow velocity. The inflow velocity is calculated using differential momentum theory in an iterative manner. An initial value is assumed as the inflow velocity from the previous time step, and the angle of attack is computed from the pitch and inflow angles. From Figure 3.2, the inflow angle can be expressed as:

$$\phi = tan^{-1}(\frac{U_P}{U_T}) \tag{3.6}$$

Using the angle of attack, the lift and drag coefficients are determined. For $\alpha < 15°$, the zero lift drag coefficient $C_{d0} = 0.0012$ and the lift-curve slope $C_{l\alpha} = 5.7/\text{rad}$ are used. For higher angles of attack, the lift and drag coefficients are interpolated from 2-D airfoil look-up tables.

On the n^{th} blade element of width dy, the elemental lift dL_n and elemental drag dD_n are:

$$dL_n = \frac{1}{2}\,\rho\,U_n^2\,c\,C_{l,n}\,dy \tag{3.7}$$

$$dD_n = \frac{1}{2}\,\rho\,U_n^2\,c\,C_{d,n}\,dy \tag{3.8}$$

where the resultant velocity is $U_n^2 = U_{p,n}^2 + U_{T,n}^2$, $C_{l,n}$ and $C_{d,n}$ are respectively the lift and drag coefficients of the n^{th} blade element. The elemental forces can be resolved into in-plane and out-of-plane components.

$$dF_{x,n} = dL_n\,\sin(\phi) + dD_n\cos(\phi) \tag{3.9}$$

$$dF_{z,n} = dL_n\,\cos(\phi) - dD_n\,\sin(\phi) \tag{3.10}$$

The elemental thrust dT_n and torque dQ_n over an annulus are obtained from Equations 3.9 and 3.10:

$$dT_n = N_b\,dF_{z,n} \tag{3.11}$$

$$dQ_n = N_b\,dF_{x,n}\,y_n \tag{3.12}$$

where N_b is the number of blades. The induced velocity in hover $v_{h,n}$ is computed from dT_n:

$$\begin{aligned} v_{h,n} &= \sqrt{\frac{dT_n}{2\,\rho\,A_{annul}}} \\ &= \sqrt{\frac{dT_n}{4\,\rho\,\pi\,y_n\,dy\cos\beta}} \end{aligned} \tag{3.13}$$

where A_{annul} is the area of the annulus, ρ the air density.

Let us now calculate the induced velocity $v_{i,n}$ over one annulus. First the induced velocity v_i over the rotor is derived from momentum theory. Before reaching autorotation, the rotor is operating in windmill brake state because it is extracting power from the airflow. The control volume of a rotor operating in windmill brake state is shown in Figure 3.3. V_d is the descending velocity, v_i the inflow velocity and w is the slipstream velocity. This representation of the flow through the rotor can be used to derive the inflow velocity over the rotor in steep descent, i.e. for climb velocity ratio $\frac{V_c}{v_h} < -2$. The flow is uniform over the whole rotor. The mass flow through the whole rotor disk is:

$$\dot{m} = \rho A(v_i - V_d) \tag{3.14}$$

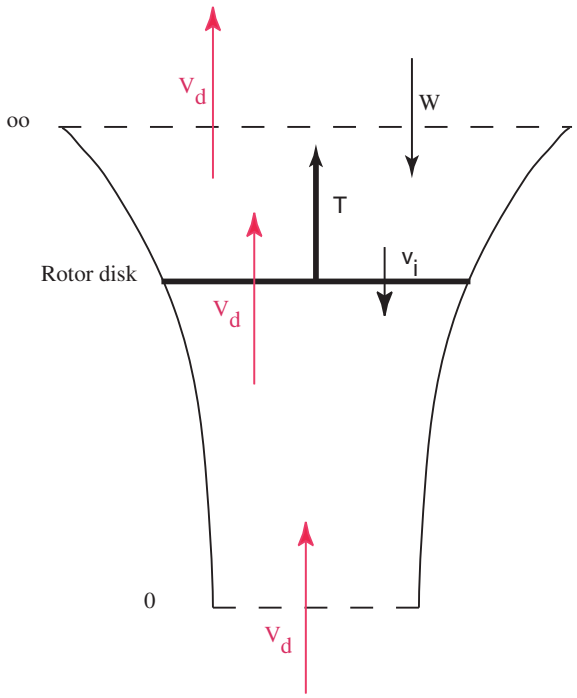

Figure 3.3: Control volume of a rotor in windmill brake state.

with A the area of the rotor. As the rotor is in descent, the flow is up through the rotor disk. Using the conservation of momentum, the thrust can be written as:

$$\begin{aligned} T &= \iint_{\infty} \rho\,(\vec{V}\cdot d\vec{S})\vec{V} - \iint_{0} \rho\,(\vec{V}\cdot d\vec{S})\vec{V} \\ &= -\dot{m}\,(w - V_d) - (-\dot{m})\,(-V_d) \\ &= -\dot{m}\,w \end{aligned} \tag{3.15}$$

W, the work done by the rotor on the flow is obtained from the conservation of energy:

$$\begin{aligned} W &= \iint_{\infty} \frac{1}{2}\rho\,(\vec{V}\cdot d\vec{S})\vec{V}^2 - \iint_{0} \frac{1}{2}\rho\,(\vec{V}\cdot d\vec{S})\vec{V}^2 \\ T(v_i - V_d) &= \frac{1}{2}\,\dot{m}\,(-(w - V_d)^2 + (-V_d)^2) \end{aligned} \tag{3.16}$$

Using Equation 3.15, the Equation 3.16 becomes

$$\begin{aligned} -\dot{m}\, w\, (v_i - V_d) &= \frac{1}{2}\, \dot{m}\, (-(w - V_d)^2 + (-V_d)^2) \\ -\dot{m}\, w\, (v_i - V_d) &= \frac{1}{2}\, \dot{m}\, (V_d^2 - V_d^2 - w^2 + 2wV_d) \\ -(v_i - V_d) &= \frac{1}{2}\, (-w + 2V_d) \\ -\dot{m}\, (v_i - V_d) &= \dot{m}\, (-\frac{w}{2} + V_d) \\ w &= 2\, v_i \end{aligned} \tag{3.17}$$

Using Equation 3.15, Equation 3.13 becomes:

$$\begin{aligned} v_h^2 &= \frac{-2\rho A(v_i - V_d)v_i}{2\rho A} \\ &= -v_i^2 + V_d\, v_i \end{aligned} \tag{3.18}$$

The following quadratic equation can therefore be obtained:

$$(\frac{v_i}{v_h})^2 - \frac{V_d}{v_h}\frac{v_i}{v_h} + 1 = 0 \tag{3.19}$$

There are two possible solutions for the induced velocity $\frac{v_i}{v_h}$:

$$v_i = \frac{V_d}{2} \pm \sqrt{(\frac{V_d}{2})^2 - v_h^2} \tag{3.20}$$

The root $v_i = \frac{V_d}{2} + \sqrt{(\frac{V_d}{2})^2 - v_h^2}$ gives non physical values of induced velocities and is therefore discarded. Thus, the solution is :

$$v_i = \frac{V_d}{2} - \sqrt{(\frac{V_d}{2})^2 - v_h^2} \tag{3.21}$$

Finally the induced velocity over one annulus can be obtained by rewriting Equation 3.21 in terms of annuli:

$$v_{i,n} = \frac{V_d}{2} - \sqrt{(\frac{V_d}{2})^2 - v_{h,n}^2} \tag{3.22}$$

with $v_{h,n}$ obtained from Equation 3.13.

From this induced velocity, an updated value of out-of-plane velocity is calculated using Equation 3.5. A new angle of attack is then found for each blade element. At the same time, the elemental lift and centrifugal forces on each blade segment create moments, M_{AF} and M_{CF}

respectively, which generate a flapping motion. These moments are computed as follows:

$$M_{AF} = \sum_{n=1}^{N_{seg}} dF_{z,n}\,(y-e)\,cos\beta \tag{3.23}$$

$$M_{CF} = \sum_{n=1}^{N_{seg}} m_{seg}\,\Omega^2\,(y_n-e)\,sin\beta\,[e+(y_n-e)\,cos\beta] \tag{3.24}$$

where m_{seg} is the mass of a blade element and e the hinge offset. Based on these moments, the flap angle is written as :

$$\beta(t) = \begin{cases} \frac{M_{AF}-M_{CF}}{k_\beta} + \beta_p & \text{if } \beta \geq 0, \\ \\ \frac{M_{AF}+M_{CF}}{k_\beta} + \beta_p & \text{if } \beta < 0. \end{cases} \tag{3.25}$$

with k_β the flapping stiffness of the δ_3 hinge and β the flap angle at the time step considered.

In this manner, a new value for the flap angle can be found, which yields an updated value for the blade pitch (Equation. 3.1). Subsequently, from the new values of angle of attack and blade pitch, in-plane and out-of-plane loads are calculated. The procedure is repeated till the inflow velocities and flap angle converge, yielding final converged values for the aerodynamic forces on each blade element. By integrating the elemental thrust (Equation 3.11) and torque (Equation 3.12) over the blade span, the forces acting on the rotor at the given time step can be expressed as:

$$T = \sum_{n=1}^{N_{seg}} dT_n \tag{3.26}$$

$$Q = \sum_{n=1}^{N_{seg}} dQ_n \tag{3.27}$$

3.1.4 Step 4 : Check for autorotation

At this stage, the value of the rotor torque is checked. If it is close to zero (i.e. less than 0.001), then it is assumed that the rotor has achieved a state of steady autorotation and further computations are stopped. If not, the computation proceeds to the next time step. From the converged values of rotor thrust and torque, updated values of rotor RPM and vehicle descent velocity are found as

follows. The rotor RPM at the next time step is given by:

$$\Omega_{t+dt} = N_b \, Q_t \, \frac{dt}{I_{rotor}} \, + \, \Omega_t \tag{3.28}$$

where N_b is the number of blades, Q_t the net rotor torque at the time t, dt the duration of the time step, Ω_t the rotational speed at the current time step and Ω_{t+dt} the rotational speed at the next time step. I_{rotor} is the rotor moment of inertia about the hub given by $I_{rotor} = \frac{N_b}{3} \, m_{blade} \, (R-e)^2$.

The vehicle is under the influence of its own weight W and the thrust T it produces. Therefore, its vertical acceleration, a_{body} is:

$$a_{body} = \frac{T - W}{m_{tot}} = \frac{T - m_{tot} \, g}{m_{tot}} \tag{3.29}$$

The updated descent velocity $V_{d,t+dt}$ is given by:

$$V_{d,t+dt} = V_{d,t} + dt \, a_{body,t} \tag{3.30}$$

The updated blade root pitch θ_{t+dt}, rotor RPM Ω_{t+dt} and descent velocity $V_{d,t+dt}$ are inputs to the next time step and are used in Equations. 3.1, 3.4 and 3.5 respectively.

The entire procedure is then repeated for the next time step and the computation proceeds in time until the state of autorotation is reached.

It was found that this procedure suffers from one major drawback. During the transient state described by this analysis, portions of the blades may go into Vortex Ring State (VRS) which is defined by low rate of descent. At those spanwise locations, the direction of the flow is not known, and there is no unique solution to the calculated $v_{i,n}$. Therefore, the induced velocity over the whole rotor cannot be defined as in Equation. 3.21. In this region, the ratio of the induced velocity over the hover induced velocity, $\frac{v_i}{v_h}$ is defined using the following curve fit based on measurements in NACA TN 3238 (Ref. [2]):

$$\frac{v_i}{v_h} = \kappa + k_1 \frac{V_c}{v_h} + k_2 (\frac{V_c}{v_h})^2 + k_3 (\frac{V_c}{v_h})^3 + k_4 (\frac{V_c}{v_h})^4 \tag{3.31}$$

where $\kappa = 1.15$ is the induced power factor and $k_1 = -1.125$, $k_2 = -1.372$, $k_3 = -1.718$, $k_4 = -0.655$. This curve fit is plotted on Figure. 2.3 along with analytical solutions for $\frac{v_i}{v_h}$ in climb and in descent condition. It was observed that because of the discontinuity between the curve

fit and the analytical solution (Equations. 3.31 and 3.21 respectively) at $\frac{V_c}{v_h} = -2$, a numerical oscillation could occur, rendering any convergence very difficult.

Therefore, it was determined that the time marching model cannot predict accurately the behavior of the system in these conditions. To address this issue, another analytical model was developed.

3.2 RPM Sweep Study

An RPM sweep analysis was developed to address the short-comings of the time marching model. This analysis was based on blade element momentum theory (BEMT). Similar to the time marching model, the goal of the steady state model is to investigate the influence of various parameters and variables on the behavior of the system when it has reached its equilibrium condition. As the flow through the rotor is not clearly defined in Vortex Ring State, this method does not attempt to calculate the inflow in this operating state. For a given RPM, the model calculates the rotor thrust T and torque Q from Blade Element momentum Theory (B.E.M.T.). The range of chosen RPM sweeps through the whole Windmill Brake State. However, calculation is stopped if $\frac{V_c}{v_h} \geq -2$, beyond which momentum theory is not valid (Figure 2.3). The calculated rotor torque coefficients are plotted versus RPM. An extrapolation of this curve is performed to find the zero torque point as shown in Figure 3.4. This point corresponds to the steady state autorotation and yields the RPM at autorotation at which thrust and torque are calculated.

The development of the RPM sweep analysis is based on similar assumptions than the time marching analysis:

1. Quasi-steady B.E.M.T. was used to determine the rotor airloads.

2. The flow was assumed purely axial.

3. Sea level conditions were considered.

4. As the angles are small in the steady state case, the coefficient of lift of the airfoil C_l is obtained by multiplying the lift curve slope $C_{l\alpha}$ by the the angle of attack α. The coefficient

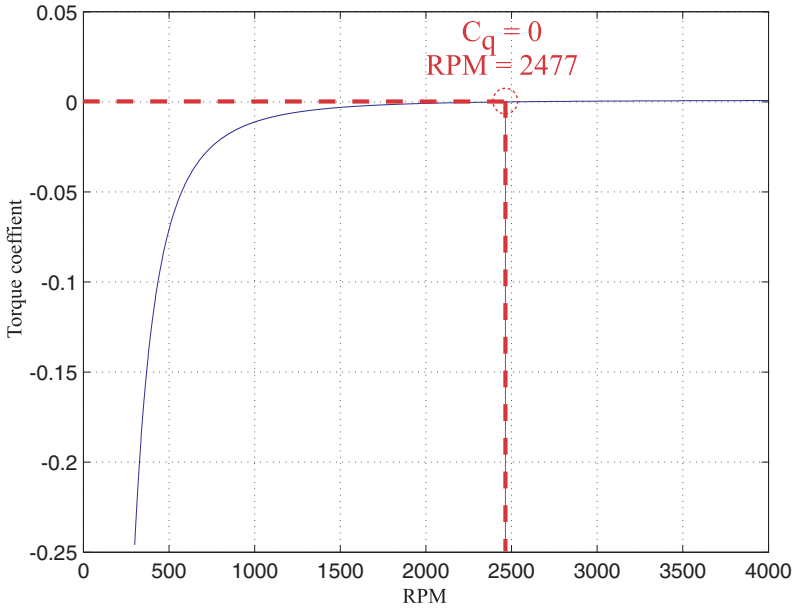

Figure 3.4: Sample result of rotor torque coefficient versus RPM given by the RPM sweep method.

of drag of the airfoil C_d is a constant chosen as 0.04.

The analysis includes blade dynamics, kinematic coupling and a refined blade element theory based asymptotic solution procedure. Given a descending velocity and a rotational velocity, the aerodynamic angles and forces are computed at each blade segments until the blade flap angle converges. The rotor thrust and torque are then output. The model can be divided into five parts:

(i) The rotor geometry and flight parameters are input to the code.

(ii) Inputs: the descending velocity, rotational speed, pitch angle, flap angle, δ_3 angle and flapping stiffness are provided.

(iii) Inflow,λ : the inflow λ is calculated at each blade segment.

(iv) The aerodynamic angles and forces are computed until the flap angle converges.

(v) Definition of autorotation : autorotation is defined from the plot of rotor torque coefficient versus RPM. The curve is extrapolated to provide the point of zero torque coefficient which corresponds to the steady state of autorotation.

The algorithm for the analysis is shown as a flowchart in Figure 3.5, and each step is explained in detail below.

3.2.1 Step 1 : Inputs

The model is given the following inputs:

1. An assumed rotational speed Ω.
2. Rotor geometry.
3. The descending velocity V_d and flight parameters.
4. The flapping stiffness obtained from the flapping frequency.

3.2.2 Step 2 : Initial conditions

Initial conditions are provided to the analysis:

1. The pitch angle θ at a segment is equal to the initial pitch of the blade θ_0, plus the blade twist θ_{TW}.
2. The flapping angle β is equal to the precone angle β_p.

3.2.3 Step 3 : Inflow, λ

The inflow is calculated by equating the incremental thrust coefficient dC_T from the momentum theory and from the blade element momentum theory.

The incremental thrust coefficient from the blade element momentum theory can be written as:

$$dC_{Tbemt} = \frac{dT}{\rho A(\Omega R)^2} \tag{3.32}$$

Rewriting dT as a function of the number of blades and the elemental lift dL on a blade element

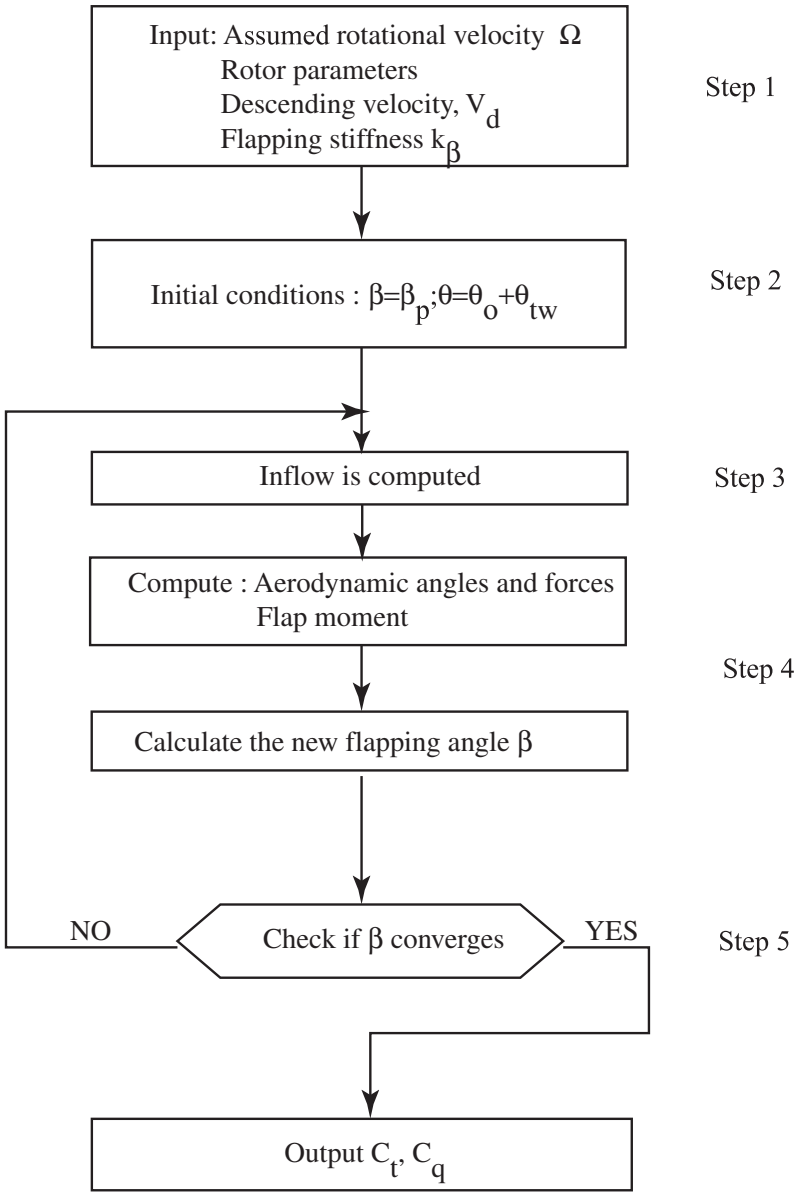

Figure 3.5: Algorithm flowchart of the rotor steady state response.

(Figure 3.2):

$$\begin{aligned} dC_{Tbemt} &= \frac{N_b dL}{\rho A(\Omega R)^2} \\ &= \frac{1}{2}\frac{N_b \rho C_L U^2 c dy}{\rho A(\Omega R)^2} \\ &= \frac{1}{2}\frac{N_b C_L U^2 c dy}{A(\Omega R)^2} \end{aligned} \tag{3.33}$$

with C_L the lift coefficient and U the resultant velocity. U can be expressed as a function of in-plane and out-of-plane velocities U_T and U_P respectively.

$$U^2 = U_T^2 + U_P^2 \tag{3.34}$$

It is assumed that U_P is negligible with respect to U_T in steady state. Therefore, Equation. 3.33 becomes

$$\begin{aligned} dC_{Tbemt} &= \frac{1}{2}\frac{N_b c}{\pi R} C_L \frac{U_T^2 dy}{(\Omega R)^2 R} \\ &= \frac{1}{2}\sigma C_{L\alpha}\alpha(\frac{U_T}{\Omega R})^2 d\frac{y}{R} \\ &= \frac{1}{2}\sigma C_{L\alpha}\alpha(\frac{U_T}{\Omega R})^2 dr \end{aligned} \tag{3.35}$$

where σ is the rotor solidity, $C_{L\alpha}$ the lift curve slope coefficient, α the angle of attack, dr the non dimensional width of the blade element. The angle of attack can be written as a function of the pitch angle θ and the inflow angle ϕ:

$$\alpha = \theta - \phi \tag{3.36}$$

Therefore, Equation 3.35 can be written as :

$$dC_{Tbemt} = \frac{1}{2}\sigma C_{L\alpha}(\theta - \phi)(\frac{U_T}{\Omega R})^2 dr \tag{3.37}$$

The inflow angle ϕ is determined as in Equation. 3.6. As the analysis is for the steady state of autorotation, it is expected that the small angle assumption is valid. Hence, Equation 3.37 becomes:

$$\begin{aligned} dC_{Tbemt} &= \frac{1}{2}\sigma C_{L\alpha}(\theta(\frac{U_T}{\Omega R})^2 - \frac{U_P}{U_T}(\frac{U_T}{\Omega R})^2) dr \\ &= \frac{1}{2}\sigma C_{L\alpha}(\theta(\frac{\Omega y}{\Omega R})^2 - \frac{U_P}{\Omega R}\frac{\Omega y}{\Omega R}) dr \\ &= \frac{1}{2}\sigma C_{L\alpha}(\theta r^2 - \lambda r) dr \end{aligned} \tag{3.38}$$

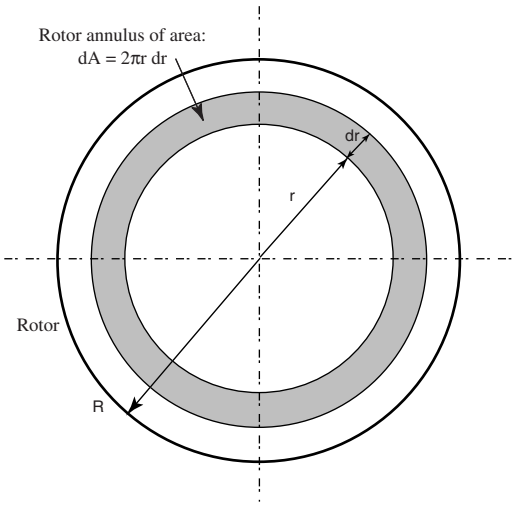

Figure 3.6: Annulus considered and its area.

Let us now calculate the incremental thrust coefficient from momentum theory dC_{Tmt}. As in Equations 3.32, dC_{Tmt} can be written as:

$$dC_{Tmt} = \frac{dT}{\rho A(\Omega R)^2} \tag{3.39}$$

The incremental thrust dT over an annulus is obtained from momentum theory, i.e. Equation 3.40 is rewritten in terms of annulus:

$$dT = -d\dot{m}\, w \tag{3.40}$$

with $d\dot{m} = \rho\, dA\, (v_i - V_d)$ is the mass flow rate over an annulus of area $dA = 2\pi y dy$ as shown in Figure 3.6. From Equations 3.39 and 3.40, the incremental thrust coefficient from momentum theory dC_{Tmt} is written as:

$$\begin{aligned} dC_{Tmt} &= \frac{-\rho dA(v_i - V_d)2v_i}{\rho A(\Omega R)^2} \\ &= -2\frac{dA}{A}\frac{v_i - V_d}{\Omega R}\frac{v_i}{\Omega R} \\ &= -2\frac{2\pi y dy}{\pi R^2}(\lambda_i - \lambda_d)\lambda_i \\ &= -4rdr(\lambda_i - \lambda_d)\lambda_i \\ &= -4rdr\lambda\lambda_i \end{aligned} \tag{3.41}$$

where λ_i is the induced inflow and λ_d the descent inflow ratio.

Equating Equations 3.38 and 3.41 gives a quadratic equation in λ:

$$\lambda^2 + (\lambda_d - \frac{\sigma C_{L\alpha}}{8})\lambda + \frac{\sigma C_{L\alpha}\theta^2 r}{8} = 0 \tag{3.42}$$

Two roots are solution of Equation 3.42:

$$\lambda = -\frac{\lambda_d}{2} + \frac{\sigma C_{L\alpha}}{16} \pm \sqrt{(\frac{\lambda_d}{2} - \frac{\sigma C_{L\alpha}}{16})^2 - \frac{\sigma C_{L\alpha}\theta r}{8}} \tag{3.43}$$

However, the root $\lambda = -\frac{\lambda_d}{2} + \frac{\sigma C_{L\alpha}}{16} - \sqrt{(\frac{\lambda_d}{2} - \frac{\sigma C_{L\alpha}}{16})^2 - \frac{\sigma C_{L\alpha}\theta r}{8}}$ does not give a physical value and is therefore discarded. The physical root of Equation 3.42 is thus:

$$\lambda = -\frac{\lambda_d}{2} + \frac{\sigma C_{L\alpha}}{16} + \sqrt{(\frac{\lambda_d}{2} - \frac{\sigma C_{L\alpha}}{16})^2 - \frac{\sigma C_{L\alpha}\theta r}{8}} \tag{3.44}$$

3.2.4 **Step 4 : Aerodynamic angles and forces**

Aerodynamic angles and forces can now be computed based on the inflow. The out-of-plane velocity is obtained from the inflow ratio:

$$U_P = \lambda \Omega R \tag{3.45}$$

The in-plane velocity is :

$$U_T = \Omega y \tag{3.46}$$

The inflow angle is computed by substituting Equations 3.45 and 3.46 in Equation 3.6. The spanwise pitch angle is computed using Equation 3.1 and the change in pitch is calculated using Equation 3.2. The angle of attack α is obtained from the pitch and inflow angles (Figure 3.2) and the lift coefficient C_L is determined by:

$$C_L = C_{L\alpha}\alpha \tag{3.47}$$

The drag coefficient is chosen constant (for instance $C_d = 0.4$). The elemental lift dL and drag dD (Figure 3.2), the elemental forces components on the horizontal and vertical axis, the elemental thrust dT and torque dQ are computed using Equations 3.7- 3.12 respectively.

Once these quantities have been computed at all stations along the blade, the non-dimensional aerodynamic flapping moment $\overline{M_{AF}}$ can be calculated:

$$\overline{M_{AF}} = \frac{\sum_{n=1}^{N_{seg}} (dF_{z,n}\, y_n)}{\Omega^2\, I_b} \tag{3.48}$$

where I_b is the blade moment of inertia about the flapping hinge. The non-rotating flapping frequency ν_{β_0} and rotating flapping frequency ν_{β_e} are defined as:

$$\nu_{\beta_0} = \sqrt{\frac{k_\beta}{I_b\,\Omega^2}} \tag{3.49}$$

$$\nu_{\beta_e} = \sqrt{\nu_{\beta_0}^2 + 1} \tag{3.50}$$

The flap equation in non-dimensional form is:

$$\overset{\star\star}{\beta} + \nu_{\beta_e}^2\,\beta = \gamma\overline{M_{AF}} + \frac{\omega_{\beta_0}^2}{\Omega^2}\,\beta_p \tag{3.51}$$

The flap angle is derived from Equation 3.51 and uses Equations 3.48, 3.49 and 3.50:

$$\beta = \frac{\overline{M_{AF}}}{\nu_{\beta_e}^2} + \beta_p\frac{\nu_{\beta_0}^2}{\nu_{\beta_e}^2} \tag{3.52}$$

The change in flap angle $\Delta\beta$ is then calculated and substituted in Equation 3.2 to calculate the variation in pitch. The whole process is repeated until β converges. Once β has converged, the rotor thrust T and torque Q are obtained from Equations 3.26 and 3.27. The coefficient of thrust C_T and torque C_Q are then calculated.

Finally the climb velocity ratio is checked. If $\frac{V_c}{v_h}$ is such that momentum theory is not valid, i.e. if $-2 < \frac{V_c}{v_h} < 0$, the calculation is stopped and the curve of rotor torque coefficient versus RPM is extrapolated to find the RPM at $C_q = 0$. Then rotor thrust and RPM are output. If $\frac{V_c}{v_h} < -2$, then the computation proceeds to the next RPM.

3.2.5 Step 5 : Definition of Autorotation

The procedure described above is repeated for a range of rotational velocities Ω. Autorotation is reached at the Ω for which the torque coefficient C_Q is close to zero. Aerodynamic angles and forces are computed at this particular Ω.

Chapter 4

Wind tunnel tests

4.1 Goal

The goal of the wind tunnel tests was to validate the theory presented in Chapter 3. To this end, steady RPM and Thrust were measured for different sets of rotor parameters. Because the wind tunnel offered a controlled environment, the influence of the pitch, precone and pitch-flap coupling on the steady state could be investigated.

This chapter discusses the construction of a scaled rotor model that was used to perform the wind tunnel tests. The set-up and instrumentation used during the tests are presented. The results of the tests are then used to validate the analysis. Finally, a parametric study is carried out to quantify the influence of each parameter on the steady state thrust and RPM of the rotor.

4.2 Prototype construction

A two-bladed model scale rotor (Figure. 4.1) of diameter 13" was sized to fit the dimensions of the open-jet wind tunnel. The model rotor grips are made of Delrin and shown in Figure 4.2. The δ_3 hinge on the model scale grips is implemented by a flexure that is achieved by milling a groove in the grips as shown in Figure 4.3. The thickness of the grip at this location is smaller, resulting in a lower local stiffness. Flexure hinges with a δ_3 of angle $-30°$, $-45°$ or $-50°$ were machined (Figure. 4.3). Blade grips without δ_3 were also manufactured, so the case of no pitch-flap coupling could be tested. The hub features a negative precone of $\beta_p = 0°$, $\beta_p = -4°$ or $\beta_p = -6°$ (Figure. 4.4). A negative collective pitch can be set at the blade root. The collective pitch is adjustable by rotating the grip around the hub fixture and fixing the position of the grip with set screws (Figure. 4.4). The technical drawings of the model scale rotor assembly are shown in Appendix A.1.

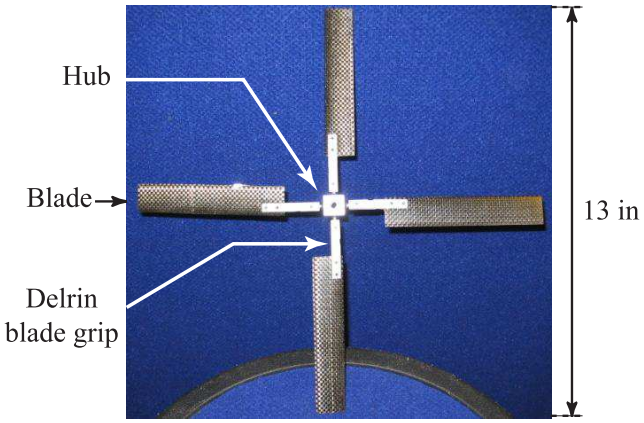

Figure 4.1: Model rotor

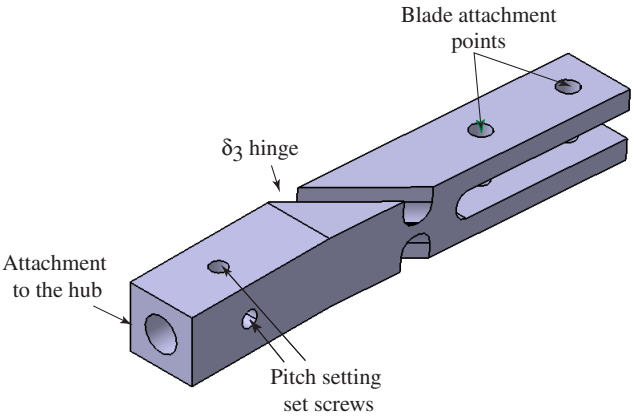

Figure 4.2: Isometric view of a model scale grip

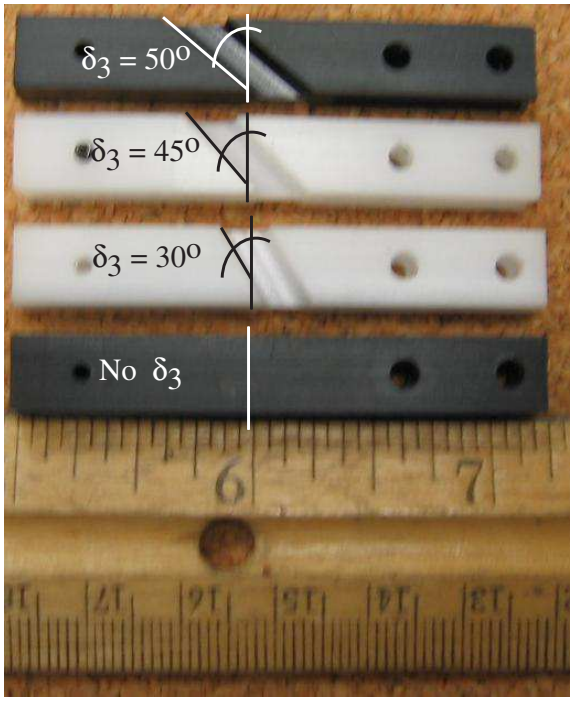

Figure 4.3: Close view of small scale grips featuring negative or zero pitch-flap couplings.

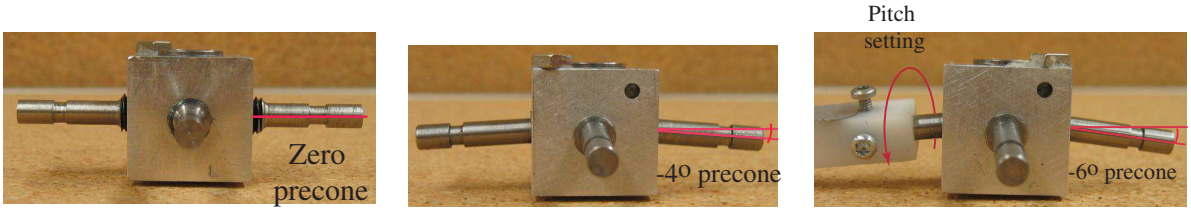

(**a**) $\beta_p = 0°$ (**b**) $\beta_p = -4°$ (**c**) $\beta_p = -6°$

Figure 4.4: Small scale hub featuring different precone angles β_p.

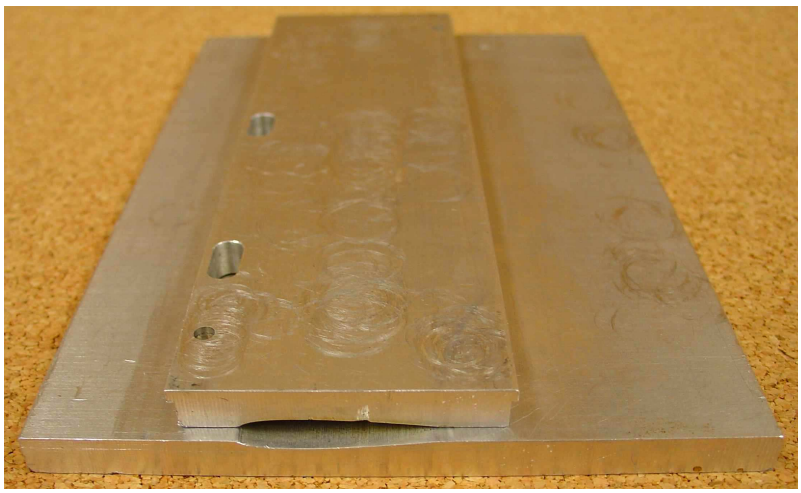

Figure 4.5: NACA 0010 mold used to manufacture the small scale blades.

A NACA-0010 airfoil shaped mold (Figure 4.5) was used to build the model scale blades. The blades were made out of 31-Rohacell foam, of density 32 kg/m^3 (Ref. [14]), and covered with one ply of $\pm 45°$ carbon fiber weave. The blades were untwisted, measure 6" span-wise and 1" chord-wise and weigh 5.2 g each (Figure 4.6). The characteristics of the blades are presented in Table 4.1.

The foam was first compressed into the mold and cured for one hour at $180°C$. The cured foam core was then wrapped in carbon fiber weave. The assembly was wrapped in releasing film so the composite does not stick to the mold. The blade was finally cured in the mold for one hour at $177°C$.

4.3 Bench-top tests

The δ_3 angle was measured to ensure the values used in the analysis are known accurately. Because of the finite width of the δ_3 flexure hinge, the bending might not occur along its central axis. Therefore, the effective angle of δ_3 may be different from the angle between the middle line of the hinge and the flap axis as shown in Figure 4.7). Bench-top tests are therefore performed to measure accurately the effective δ_3 angle.

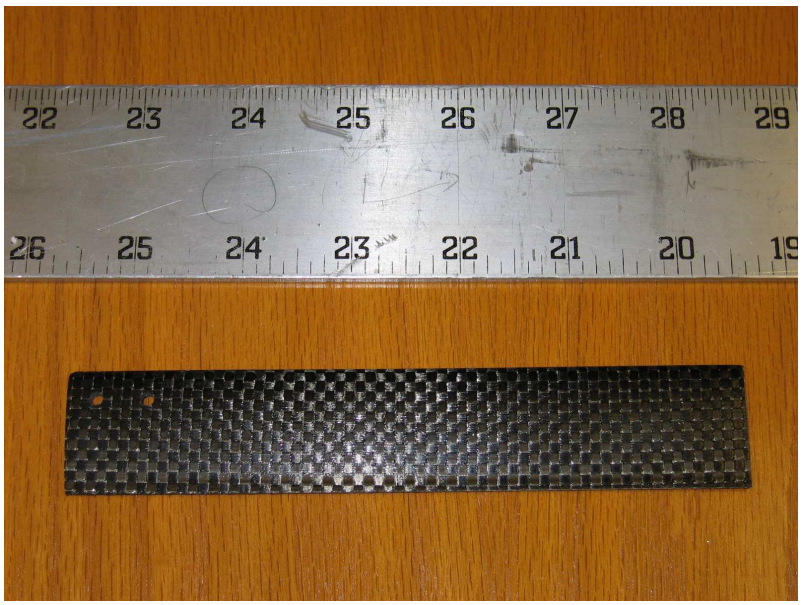

Figure 4.6: Close view of a small scale blade.

Table 4.1: Small scale rotor characteristics

Rotor diameter (in)	13
Blade number, N_b	2
Blade span (in)	6
Blade chord (in)	1.13
Blade twist (deg/in)	0
Blade mass (kg)	0.0052
Airfoil	NACA 0010
Pitch-flap coupling angle, δ_3 (deg)	-30 ; -45 ; -50
Precone angle, β_p (deg)	0 ; -4 ; -6

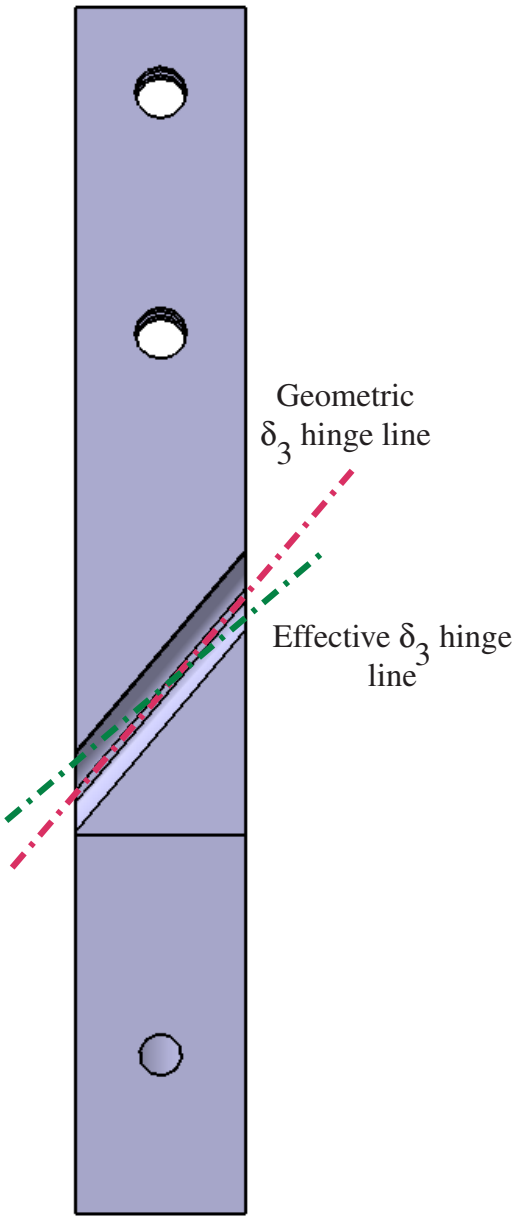

Figure 4.7: Skewed δ_3 hinge.

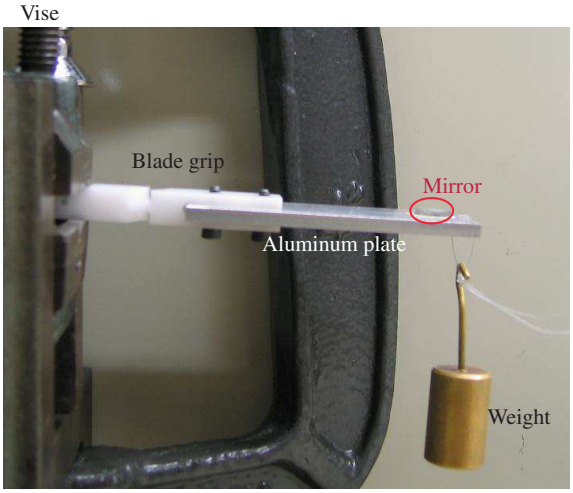

Figure 4.8: Close view of the set-up to determine the δ_3 angle of a small scale grip.

4.3.1 Bench-top test set-up

An aluminum plate is inserted in place of the blade in the blade grip so that weights can be applied at a known location. The root of the grip is clamped in a vise (see Figure 4.8). Care was taken to leave the δ_3 hinge free to deflect. A mirror is attached at the end of the aluminum plate, at the mid-chord. Weights are then suspended from this location. A laser beam is reflected off the mirror onto a surface covered with graph paper. The distance h (Figure 4.9)between this surface and the mirror must be maximized to minimize the measurement error.

If the aluminum plate/mirror assembly is at its reference position, i.e. in a horizontal axis, the incident and deflected laser rays are coincident. As shown on Figure 4.9, if this assembly deflects by an angle of $\beta°$, the angle between the incident laser beam and the perpendicular to the mirror is $\beta°$. The angle between the reflected laser beam and the perpendicular to the mirror is also $\beta°$ as the angle of reflection is equal to the angle of incidence. Therefore, the angle between the incident and deflected laser beam is $2\beta°$. Figure 4.10 shows a picture of the measured laser beam deflection for different applied loads. The deflection along the bending axis is a result of the flapping stiffness of the grip. The δ_3 angle is measured between the line of pure bending and the line of combined bending and torsion.

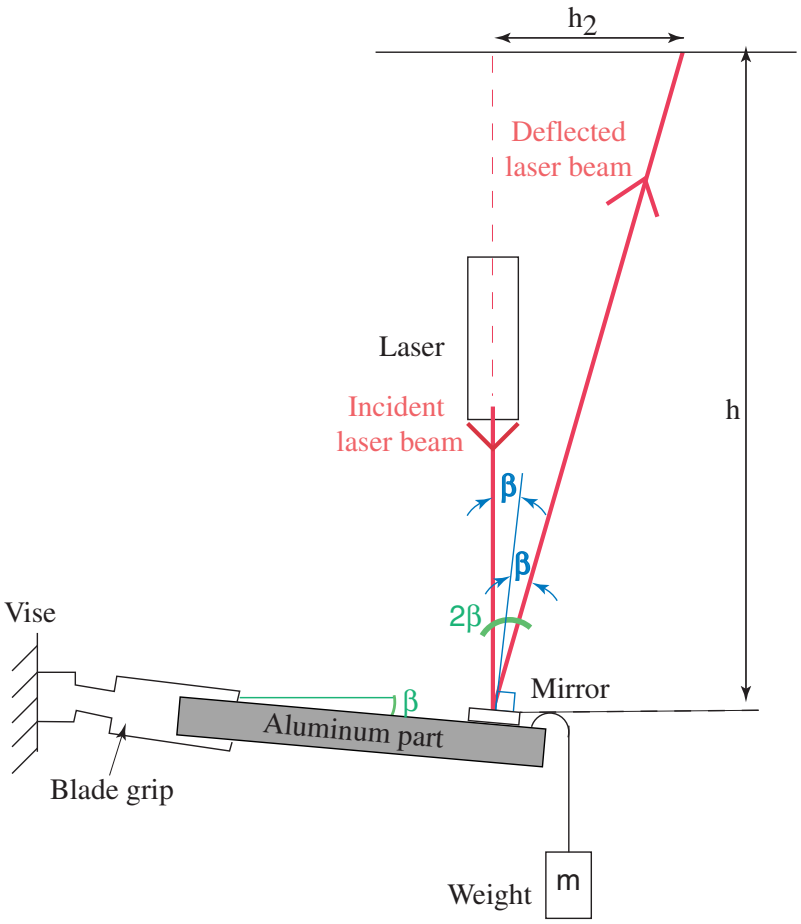

Figure 4.9: Schematic of the set up to measure the δ_3 angle and flapping stiffness.

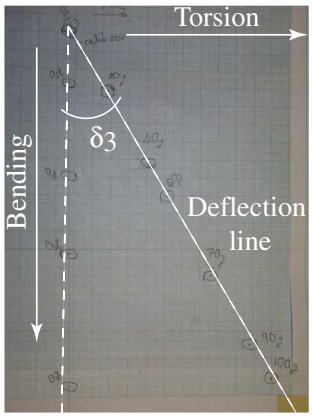

Figure 4.10: Measurement of the δ_3 angle.

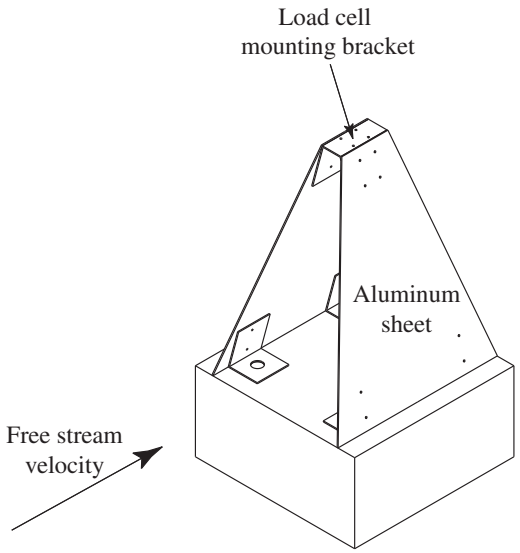

Figure 4.11: Test stand used during the wind tunnel tests.

4.3.2 Results

As a result of the finite width of the δ_3 flexure hinge, it was found that the effective pitch-flap coupling hinge was not along the machined hinge axis. The resultant pitch flap coupling values (δ_3) of the small scale grips were measured to be $-29.74°$ for the $-50°$ and $-17.33°$ for the $-30°$.

4.4 Wind tunnel test set-up

The wind tunnel tests were performed on the model scale rotor, which fits in the wind tunnel test section. The rotor was mounted on a precision shaft attached to a strain gage balance. The balance was anchored to the stand shown in Figure 4.11. As seen on Figure 4.11, the stand was constituted of plain aluminum sheet to provide stable support to the rotor/balance assembly and to avoid vibrations that could adversely affect the quality of the load cell reading. In addition, the drag generated by the stand was minimized as only the cross section area of the aluminum sheet faced the free stream velocity. This minimized flow disturbances generated by the stand. The technical drawings of the wind tunnel stand are shown in Appendix A.2.

Autorotation was simulated by a free-spinning hub (the torque on hub is zero at steady state) and the wind tunnel velocity reproduces the upward flow of velocity V_d on the rotor (Figure 4.12).

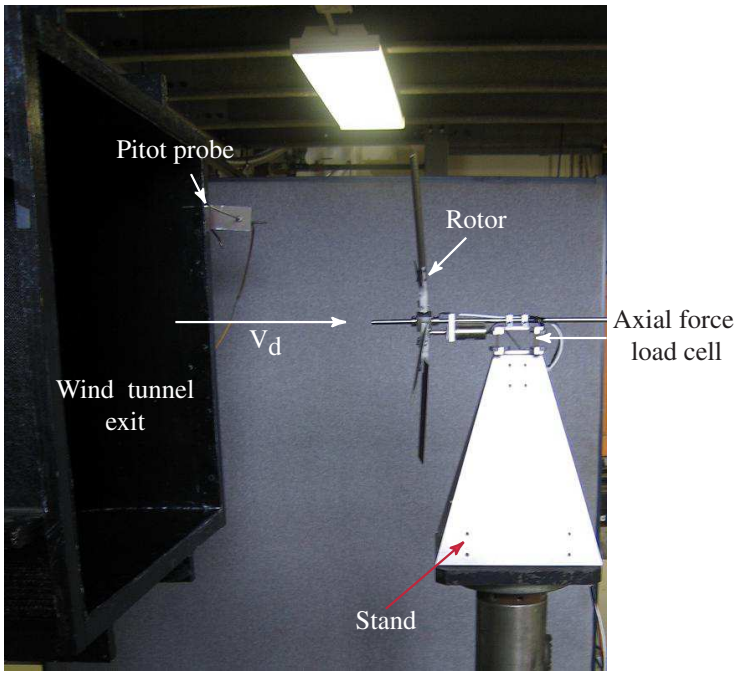

Figure 4.12: Wind tunnel test set-up.

The pitch angle of the blades must be set exactly at the same value so that the rotor is well balanced. The pitch of the blades is set using a fixture with four angled grooves in which the blade grips fit (Figure 4.13). When the rotor is at rest, the fixture is mounted on the rotor shaft and positioned against the rotor hub. The blade grips are then aligned in the grooves and their positions are locked by set screws. The blade pitch is therefore equal to the angle of the grooves with respect to the top of the fixture. This procedure ensures that all the blades have the same pitch.

4.5 Instrumentation

Instrumentation was installed to acquire rotor RPM and thrust. To this end, the following sensors were installed on the test stand:

1. The Hall switch (Figure. 4.14) was used to obtain RPM. This device is sensitive to the proximity of a magnetic field. Its output is a square wave of $0\,;-5$ volts, each rising edge

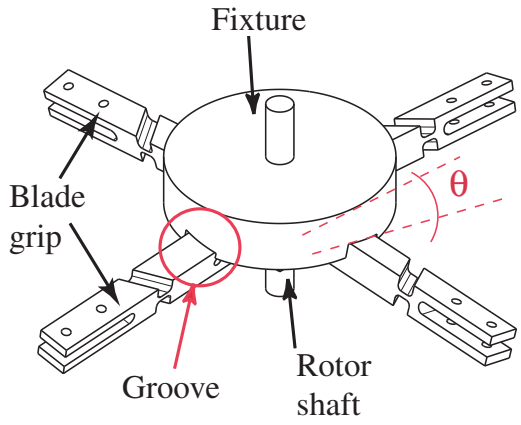

Figure 4.13: Blade pitch is set using a fixture.

occurring when a magnet passes less than a specified distance from the Hall switch. A magnet was attached to the rotor hub. The blades, hub and magnet are rotating whereas the rotor shaft and Hall switch are fixed. The RPM can then be measured from the time period of the square wave.

2. The load cell (Figure. 4.14) captured the thrust generated by the rotor. The technical drawings of the balance on which is mounted the load cell are shown in Appendix A.3.The applied load induces a strain in the load cell, which is then converted into an electrical signal.

3. The free stream velocity V_d was obtained from the dynamic and static pressures of the air exiting the wind tunnel. The pressures were sensed by a Pitot probe placed in the wind tunnel airstream and converted into voltage by a pressure transducer.

All output signals were then captured by a Data Acquisition (DAQ) board which converts the analytical data into digital format and transmits them to a computer.

4.6 Range of test conditions

The test data was collected over a range of rotor parameters: negative blade pitch setting θ_0, pitch-flap kinematic coupling δ_3, blade precone β_p and wind tunnel velocities. The different values of the rotor parameters are shown in Table 4.2. One parameter only is varied from one test to

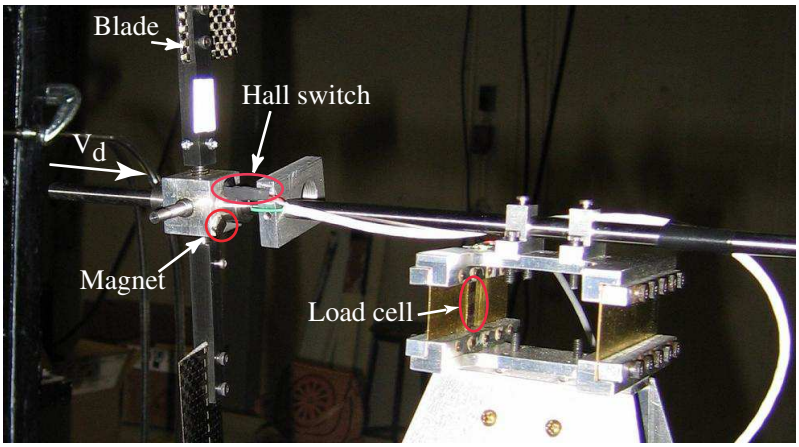

Figure 4.14: Hall switch and load cell used during the wind tunnel tests.

Table 4.2: Tested values of the different parameters.

Pitch angle (deg)	0	-6	-8	-12
δ_3 angle (deg)	None	-17.33	-29.74	
Precone angle, β_p (deg)	0	-4	-6	

another in order to study the influence of the parameter on the steady state thrust and RPM of the rotor. The general test matrix is shown in Table 4.3. The following results show test data for a two-bladed rotor ($N_b = 2$) and for wind speeds from 1 m/s to 9 m/s.

Table 4.3: General wind tunnel tests matrix.

Case #	θ_0 (deg)	δ_3 (deg)	β_p(deg)
1	-6	None	0
2	-8	None	0
3	-12	None	0
4	-6	-29.74	0
5	-8	-29.74	0
6	-12	-29.74	0
7	-6	-29.74	-4
8	-8	-29.74	-4
9	-12	-29.74	-4
10	-6	-29.74	-6
11	-8	-29.74	-6
12	-12	-29.74	-6
13	-6	-17.33	0
14	-8	-17.33	0
15	-12	-17.33	0
16	-6	-17.33	-4
17	-8	-17.33	-4
18	-12	-17.33	-4
19	-6	-17.33	-6
20	-8	-17.33	-6
21	-12	-17.33	-6

4.7 Experimental results

4.7.1 Curve fit

The validation of the analysis with the measured results is shown in the following pages. The measured steady state thrust versus wind tunnel velocity (V_d) and RPM versus V_d are presented as well as the analytical predictions based on the RPM Sweep model described in Chapter 3. In order to compare the trends of the measurements, and to correlate the analysis with the experiments, it is useful to represent the data in terms of a polynomial curve fit. For each plot of thrust versus V_d and RPM versus V_d, a curve can be fit to the experimental data points. The variation of measured thrust, T_{exp}, with V_d can be expressed as a second degree polynomial as follows:

$$T_{exp} = a_0^e V_d^2 + a_1^e V_d \tag{4.1}$$

where the superscript 'e' refers to coefficients from experimental data. The deviation of thrust data points from the polynomial fit is quantified by the regression factor R_T^2. If $R_T^2 = 1$, all the data points lie exactly on the curve fit. Figure 4.15 presents the regression factors of thrust for all cases. As all the thrust regression factors are close to 1, their values are plotted from 0.95 to 1.0 in order to visualize their variation more clearly. From Figure 4.15, it can be noticed that all regression factors are close to 1.0. The lowest regression factor is $R_T^2 = 0.9945$ and it occurs in test case #13, for a $-6°$ pitch, a $-17.33°$ pitch-flap coupling angle and a $0°$ precone. As R_T^2 is close to 1.0 for all cases, it can be concluded that the experimental thrust data versus wind tunnel speed V_d is reliable and that the expression of the thrust as in Equation 4.1 is justified. In addition, it is noted that the a_1^e coefficients are close to zero and much smaller that the a_0^e coefficients for all the experimental cases (see Table 4.4). For instance, test #1 has an experimental coefficient a_1^e of 0.0064 whereas $a_0^e = 0.0427$. Therefore, the linear part of the polynomial can be neglected and the experimental thrust can be approximated as:

$$T_{exp} = a_0^e V_d^2 \tag{4.2}$$

Similarly, the curve fit through the experimental RPM data points, Ω_{exp}, can be expressed

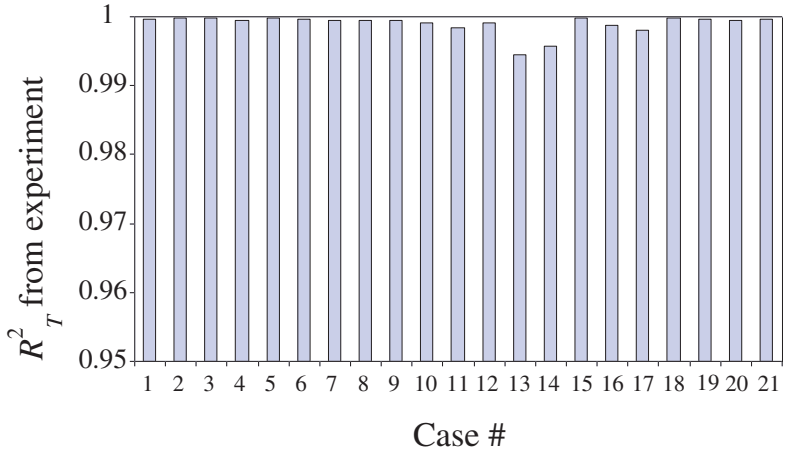

Figure 4.15: Thrust regression factor R^2_T for all cases.

as a linear function of the wind tunnel speed V_d :

$$\Omega_{exp} = b^e V_d \tag{4.3}$$

The deviation of RPM data points from the polynomial fit is quantified by the regression factor R^2_{RPM}. Figure 4.16 presents the regression factors of RPM for all cases. As all the regression factors RPM are close to 1.0, their values are plotted from 0.95 to 1.0 in order to visualize their variation more clearly. From Figure 4.16, it can be noticed that all regression factors are close to 1. The lowest regression factor is $R^2_{RPM} = 0.9863$ and occurs in test case #12, for a $-12°$ pitch, a $-29.74°$ pitch-flap coupling angle and a $-6°$ precone (Table 4.3). Hence, the experimental RPM data is reliable and the expression of RPM as in Equation 4.3 is justified.

From the RPM Sweep Method, the analytical thrust can be calculated for different V_d. It was observed that the analytical thrust predictions, T_{ana}, can be expressed exactly as a function of V_d as follows:

$$T_{ana} = a^a_0 V^2_d + a^a_1 V_d \tag{4.4}$$

where the superscript 'a' refers to coefficients from the analytical data. Similar to the case of the experimental data, it was noticed that the a^a_1 coefficients were close to zero for all cases and negligible compared to the a^a_0 coefficients (see Table 4.4). For example, for the test #1, the analytical coefficient a^a_1 is $4 * 10^{-09}$ whereas $a^a_0 = 0.0396$. Hence, the analytical predictions of

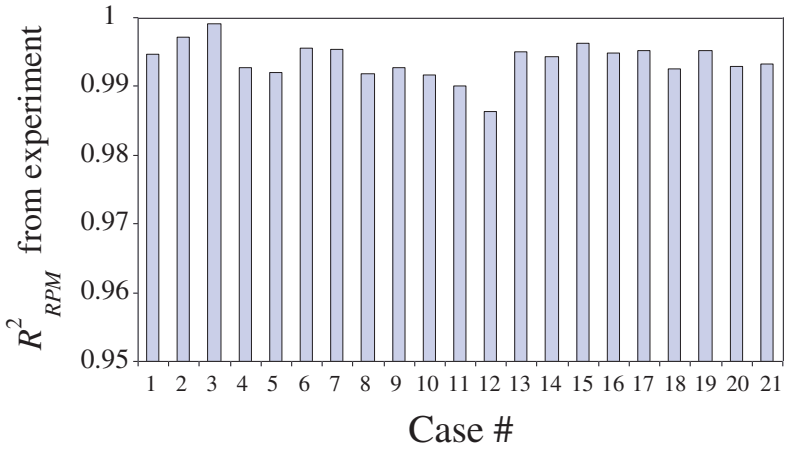

Figure 4.16: RPM regression factor R^2_{RPM} for all cases.

thrust can be approximated as:

$$T_{ana} = a_0^a V_d^2 \tag{4.5}$$

Similarly, the analytical curve of RPM can be written as a linear function of the wind tunnel speed V_d :

$$\Omega_{ana} = b^a V_d \tag{4.6}$$

Comparing the coefficients a_0^e with a_0^a and b^e with b^a provide a convenient means to evaluate the accuracy of the analytical predictions with respect to the experimental data. In addition, the trends can be observed by examining the coefficients of the curve-fits. Table 4.4 shows the a_0^e, a_1^e and a_0^a, a_1^a coefficients for the experimental curve fit and analytical predictions respectively, as well as the b^e and b^a coefficients from the RPM experimental results and analytical predictions. The error between experimental data and analytical predictions of thrust, E_T, is calculated using the following formula:

$$E_T = 100\left|\frac{a_0^e - a_0^a}{a_0^e}\right| \tag{4.7}$$

For all cases, E_T is tabulated in Table 4.4. In most cases, the E_T is in the range of 2% to 25%, except for cases 7, 8, 13, 14, 16, 17, 19. Discussion of the cause of these larger errors will follow in a subsequent section. Similarly, the error between the measurements and predictions of RPM,

Table 4.4: General wind tunnel tests matrix.

Case #	a_0^e	a_1^e	a_0^a	a_1^a	E_T (%)	b^e	b^a	E_{RPM} (%)
1	0.0427	-0.0064	0.0396	4.00E-09	7.2	403.71	362.93	10.1
2	0.0254	0.006	0.0279	3.00E-09	-9.8	343.93	326.54	5.0
3	0.0138	0.008	0.0141	-1.00E-09	-2.1	273.77	262.1	4.2
4	0.0452	-0.00229	0.0442	-0.0007	2.2	404.05	373.8	7.4
5	0.0372	-0.00102	0.0307	-0.0005	17.4	385.99	336.11	12.9
6	0.016	0.008	0.0149	-8.00E-05	6.8	290.45	263.55	9.2
7	0.092	-0.00746	0.0708	-0.0034	23.04	484.6	354.1	26.92
8	0.0688	-0.00665	0.0637	-0.0036	7.41	459.92	355.18	22.77
9	0.0303	-0.00238	0.0225	-0.0022	25.7	352.84	302.48	14.2
10	0.0833	-0.001081	0.0699	-0.0028	16.0	421.28	399.52	5.1
11	0.0669	-0.001017	0.0561	-0.0044	16.1	415.04	393.86	5.1
12	0.0333	-0.00452	0.0279	-0.0036	16.2	346.04	323.99	6.3
13	0.0853	-0.001222	0.0581	-0.0004	31.8	471.91	344.02	27.0
14	0.0486	-0.00315	0.0505	-0.0003	3.9	423.5	327.19	22.74
15	0.0181	0.0057	0.0146	-0.0001	19.3	309.96	261.35	15.6
16	0.0808	-0.00706	0.0628	-0.0017	22.27	467.22	354.71	24.0
17	0.0548	-0.00521	0.0557	-0.0015	1.6	420.08	336.66	19.8
18	0.0227	-0.0059	0.0181	-0.001	20.2	330.22	281.13	14.8
19	0.1098	-0.0747	0.0679	-0.0027	38.0	548.5	376.14	31.42
20	0.0538	-0.00447	0.0413	-0.0023	23.2	437.05	366.17	16.2
21	0.0242	-0.00117	0.0202	-0.0016	16.5	334.1	291.74	12.6

E_{RPM}, can be computed using the formula below:

$$E_{RPM} = 100\left|\frac{b_0^e - b_0^a}{b_0^e}\right| \tag{4.8}$$

The E_{RPM} for all cases are tabulated in Table 4.4. In most cases, the E_{RPM} is in the range 4% to 21%. However, the maximum E_{RPM} is 28% and occurs in test 19.

4.7.2 Discussion of experimental trends

Let us now investigate systematically the effect of each parameter on the steady state thrust and RPM. From one case to another, only one parameter varies in order to investigate its influence on the steady state rotor characteristics.

4.7.3 Change in pitch θ_0

Let us compare the thrust and RPM obtained from tests #1, #2 and #3 for a given airstream velocity V_d, for instance $V_d = 8$ m/s. In these tests, only θ_0 is varied and we can focus on the effect of this parameter. In test #1, the pitch is $\theta_0 = -6°$ and the steady state thrust is approximately $T = 2.5$ N and the RPM is $\Omega = 3400$ RPM (see Figures 4.19 and 4.20). In test #2, the pitch is $\theta_0 = -8°$, the steady state thrust is approximately $T = 1.6$ N and the RPM is $\Omega = 2700$ RPM (see Figures 4.21 and 4.22). In test #3, the pitch is $\theta_0 = -12°$, the steady state thrust is close to $T = 1$ N and the RPM is $\Omega = 2200$ RPM (see Figures 4.23 and 4.24). It can be concluded that the thrust and RPM increase with less negative pitch. This is because a less negative pitch results in a higher angle of attack and therefore a larger thrust. The same trend is observed in other groups of tests that feature different values of pitch-flap coupling angle δ_3 and precone angle β_p and is independent of the value of V_d.

4.7.4 Change in precone β_p

The thrust and RPM obtained from tests #6, #9 and #12 are compared, for a $V_d = 4.5$ m/s, to evaluate the effect of the precone variation. In test #6, the precone angle is $\beta_p = 0°$, the thrust is around 0.35 N and the RPM is $\Omega = 1260$ RPM (see Figures 4.29 and 4.30). In test #9, the precone angle is $\beta_p = -4°$, the thrust is about 0.49 N and the RPM is $\Omega = 1440$ RPM (see Figures 4.31 and 4.32). Finally, in test #12, the precone angle is $\beta_p = -6°$, the thrust is approximately 0.54 N and $\Omega = 1500$ RPM (see Figures 4.37 and 4.38). Therefore, the experiment shows clearly that the thrust and RPM increase with more negative precone. This is because the centrifugal moment and the aerodynamic moment add up to change the flap angle in upward (positive) direction.

It was observed that for hinges with no pitch-flap coupling, the measured experimental thrust and RPM values were similar for different precone $\beta_p = 0°$, $\beta_p = -4°$ or $\beta_p = -6°$. A more negative precone, and therefore a greater flap deflection, will not lead to any significant increase in pitch and thrust as there is no pitch-flap coupling.

4.7.5 Change in pitch-flap coupling angle δ_3

The thrust and RPM obtained from tests #3, #12 and #21 are compared, for a wind tunnel velocity of 6.5 m/s, to evaluate the effect of the δ_3 variation.

In test #3, the precone is $\beta_p = 0°$ whereas in tests #12 and #21, the precone is $\beta_p = -6°$. However, note that test #3 has no pitch-flap coupling, therefore it can be compared to tests #12 and #21 where the precone is $\beta_p = -6°$.

In test #3, there is no pitch-flap angle, the thrust is approximately 0.68 N and the RPM is $\Omega = 1860$ RPM (see Figures 4.23 and 4.24). In test #12, the pitch-flap coupling angle is $\delta_3 = -17.33°$, the thrust is about 0.85 N and the RPM is $\Omega = 2100$ RPM (see Figures 4.37 and 4.38). Finally, in test #21, the pitch-flap coupling angle is $\delta_3 = -29.74°$, the thrust is 0.99 N and the RPM is $\Omega = 2160$ RPM (see Figures 4.45 and 4.46). Therefore the thrust and RPM increase with more negative pitch-flap coupling.

The variation of measured steady state thrust and RPM with rotor parameters can be summarised as follows:

1. Less negative pitch angle: this results in a higher angle of attack and therefore in a larger steady state thrust and RPM.

2. More negative pitch-flap coupling: as shown in Equations 3.1 and 3.2, the increase in pitch, and therefore in thrust and RPM, is larger for more negative δ_3 angles.

3. More negative precone angle: the upward flap deflection is larger because the centrifugal moment contribution is greater. In conjunction with negative pitch-flap coupling, this will lead to an increase in pitch and result in an increase in thrust and RPM.

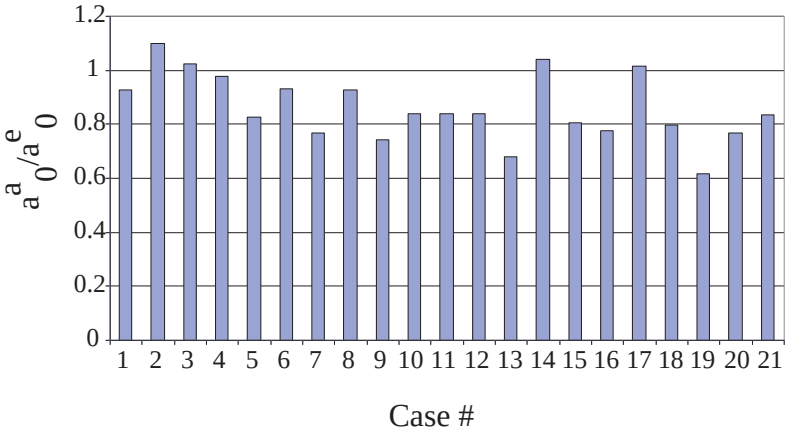

Figure 4.17: Ratio of $\frac{a_0^a}{a_0^e}$ reflects how close the analytical thrust is to the experimental data.

4.8 **Correlation with analysis**

It was shown in Section 4.7 that the experimental data was reliable. Let us check now how close the analytical predictions are to the experimental data points and examine the sources of error. As seen in section 4.7, the thrust from both the experiment and the analysis can be expressed as in Equations 4.2 and 4.5. The errors in analytical thrust, in terms of E_T, and in analytical RPM, in terms of E_{RPM}, tabulated in Table 4.4, showed that for most cases the errors between experiment and analysis are in the range 2% to 25% for thrust and less than 28% for RPM.

An alternate way of examining the correlation is to calculate the ratio of the analytical prediction of thrust, T_{ana} to the experimental thrust data T_{exp} as follows:

$$\begin{aligned} \frac{T_{ana}}{T_{exp}} &= \frac{a_0^a V_d^2}{a_0^e V_d^2} \\ &= \frac{a_0^a}{a_0^e} \end{aligned} \tag{4.9}$$

The ratio $\frac{a_0^a}{a_0^e}$ shows how close the analytical thrust predictions are to the experimental data and can also indicate if the analysis underpredicts or overpredicts the thrust. This ratio is shown for all test cases in Figure 4.17. Similarly, it was shown in Section 4.7 that the RPM can be written as in Equation 4.3 and 4.6. The comparison of the predictions and experimental data of RPM can

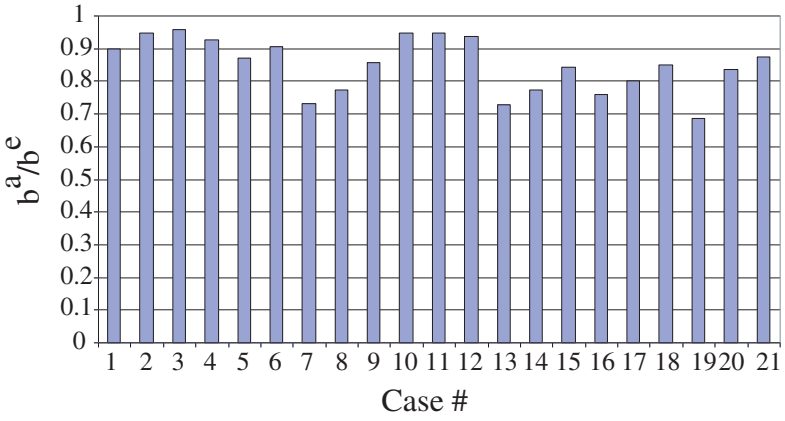

Figure 4.18: Ratio of $\frac{b^a}{b^e}$ reflects how close the analytical RPM is to the experimental data.

be obtained by the ratio:

$$\begin{aligned} \frac{\Omega_{ana}}{\Omega_{exp}} &= \frac{b^a V_d}{b^e V_d} \\ &= \frac{b^a}{b^e} \end{aligned} \tag{4.10}$$

The ratio $\frac{b^a}{b^e}$ shows how close the analytical RPM predictions are to the experimental data points, which is shown in Figure 4.18.

From Figures 4.17 and 4.18, it can be noticed that in most cases the analysis underestimates the thrust and RPM. Most of the cases with no δ_3 and with $\delta_3 = -29.74°$ show good thrust and RPM agreement. In general, the predictions show the correct trends, and less than 10 to 15% magnitude error in both thrust and RPM. However, for cases $\#7, \#8, \#13, \#14, \#16, \#17$ and $\#19$, the correlation is not accurate. For these cases, the pitch was remeasured and found to be 2° greater than the intended value. The analysis was re-run using the remeasured pitch values and the corresponding values are shown in Table 4.4 as well as Figures 4.17 and 4.18. Note that due to the inherent uncertainty in calculating the solutions by extrapolation, this amount of error in the correlation is considered acceptable.

Apart from these cases, the predictions match closely with test data confirming that the analytical model accurately captures the physical phenomena.

It is interesting to investigate the accuracy of the correlation if a lower drag coefficient is used, for instance $C_d = 0.02$ instead of $C_d = 0.04$. It was noted that for a lower C_d value,

the predictions of RPM were closer to the experimental data. For example, in case #19, the experimental coefficient b^e is 548.5. The analytical coefficient for $C_d = 0.02$ is $b^a = 488.1$, giving a RPM error $E_{RPM} = 11\%$, whereas for $C_d = 0.04$ the analytical RPM coefficient is $b^a = 394.9$, leading to $E_{RPM} = 28.0\%$. However, using a lower C_d value increases the thrust error between analytical predictions and experimental data. The experimental thrust coefficient for case #19 is $a_0^e = 0.1098$. The analytical thrust coefficient for $C_d = 0.04$ is $a_0^a = 0.0567$, giving a thrust error $E_T = 48.3\%$, whereas the analytical thrust coefficient becomes $a_0^e = 0.0523$ for $C_d = 0.02$, resulting in a thrust error $E_T = 52.3\%$. Hence, the use of $C_d = 0.04$ in the analysis is justified.

Figures 4.19- 4.46 show the measured steady state thrust versus wind tunnel velocity (V_d) and RPM versus V_d as well as the analytical predictions based on the RPM Sweep model.

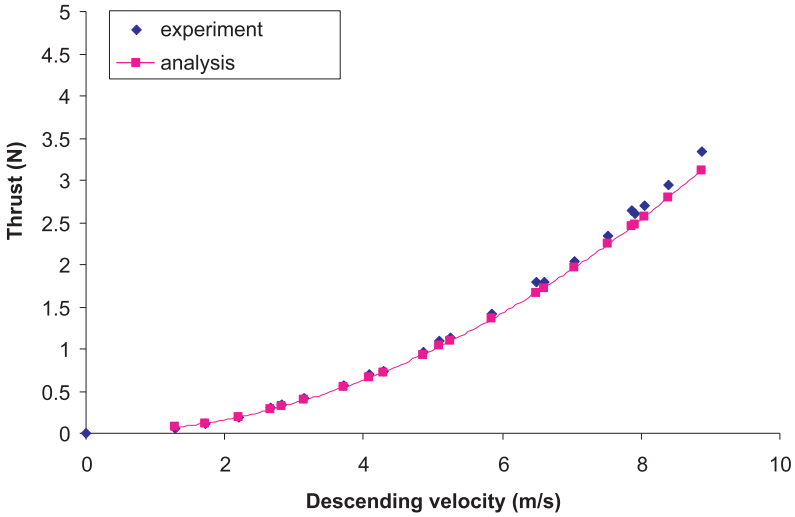

Figure 4.19: Steady state thrust generated by a 2 bladed rotor with stiff hinges, no pitch-flap coupling, precone $\beta_p = 0°$ and pitch $\theta_0 = -6°$.

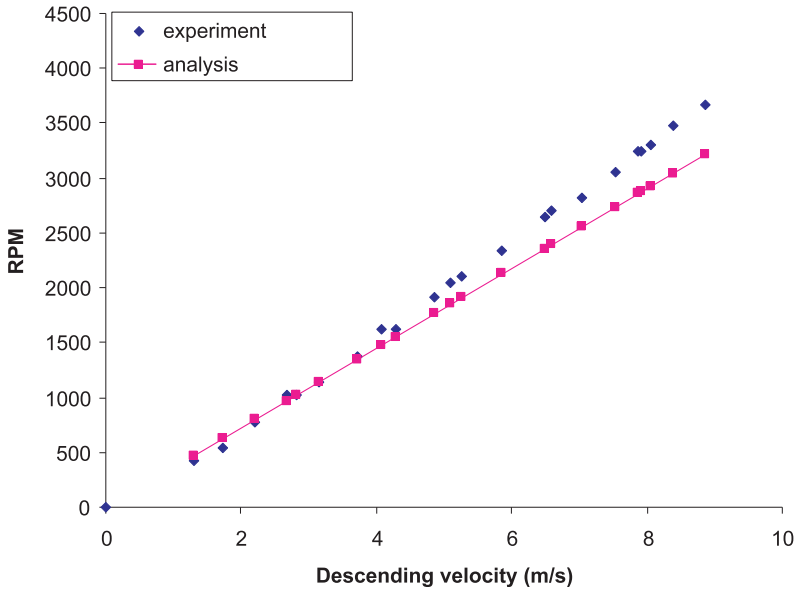

Figure 4.20: Steady state RPM generated by a 2 bladed rotor with stiff hinges, no pitch-flap coupling, precone $\beta_p = 0°$ and pitch $\theta_0 = -6°$.

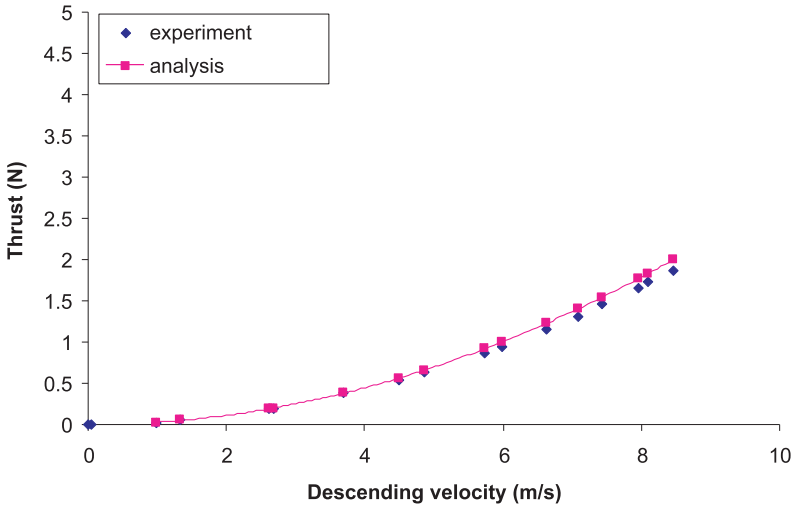

Figure 4.21: Steady state thrust generated by a 2 bladed rotor with stiff hinges, no pitch-flap coupling, precone $\beta_p = 0°$ and pitch $\theta_0 = -8°$.

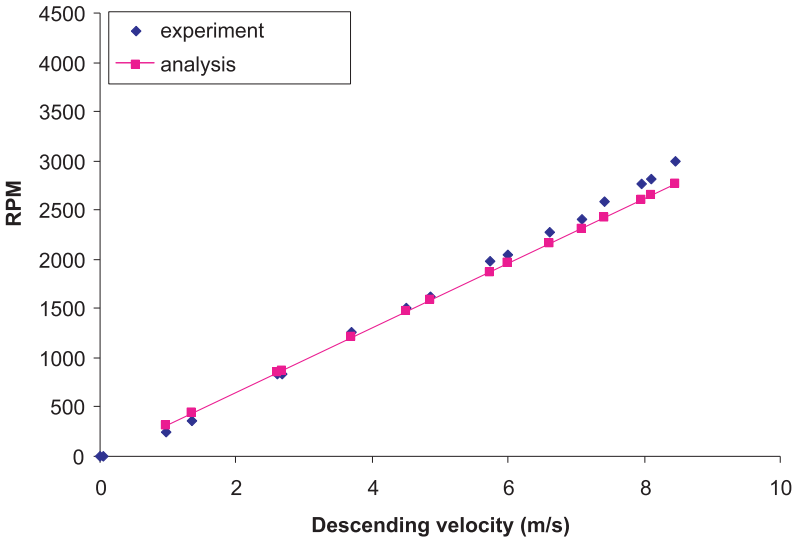

Figure 4.22: Steady state RPM generated by a 2 bladed rotor with stiff hinges, no pitch-flap coupling, precone $\beta_p = 0°$ and pitch $\theta_0 = -8°$.

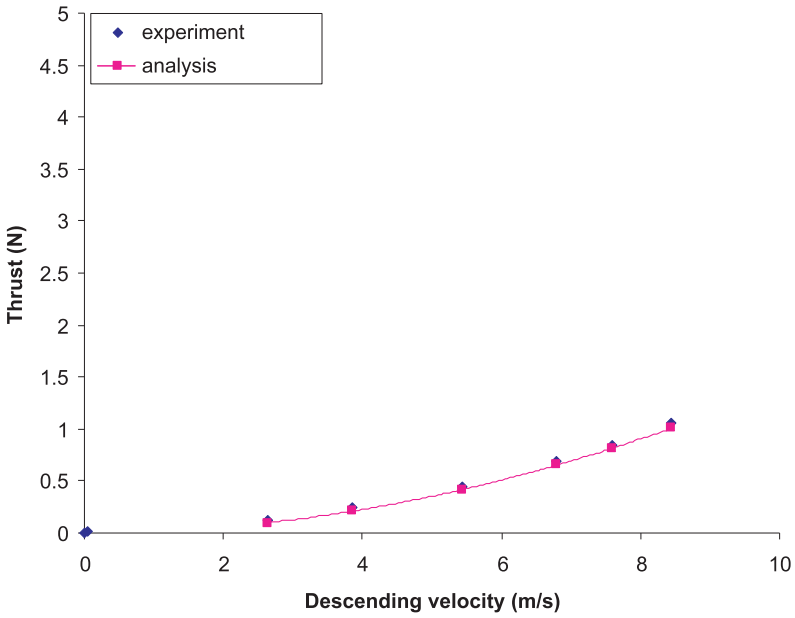

Figure 4.23: Steady state thrust generated by a 2 bladed rotor with stiff hinges, no pitch-flap coupling, precone $\beta_p = 0°$ and pitch $\theta_0 = -12°$.

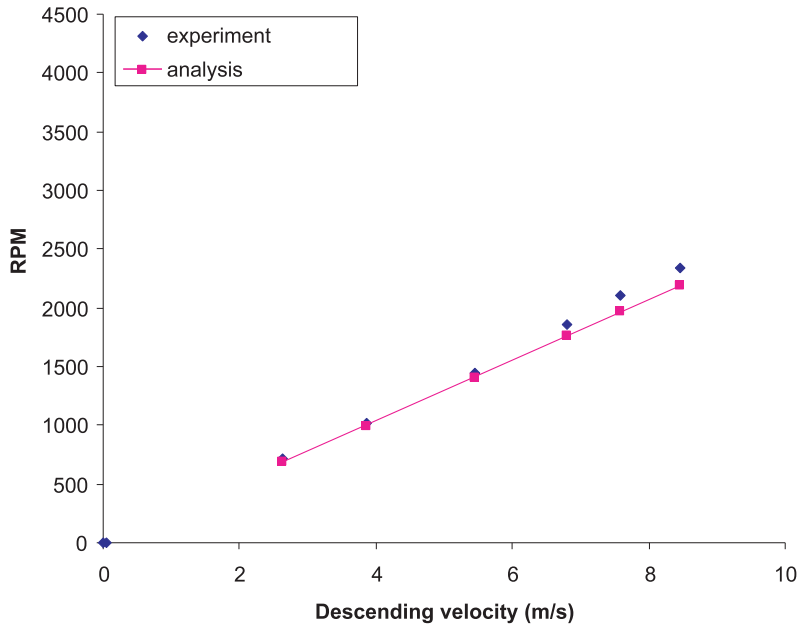

Figure 4.24: Steady state RPM generated by a 2 bladed rotor with stiff hinges, no pitch-flap coupling, precone $\beta_p = 0°$ and pitch $\theta_0 = -12°$.

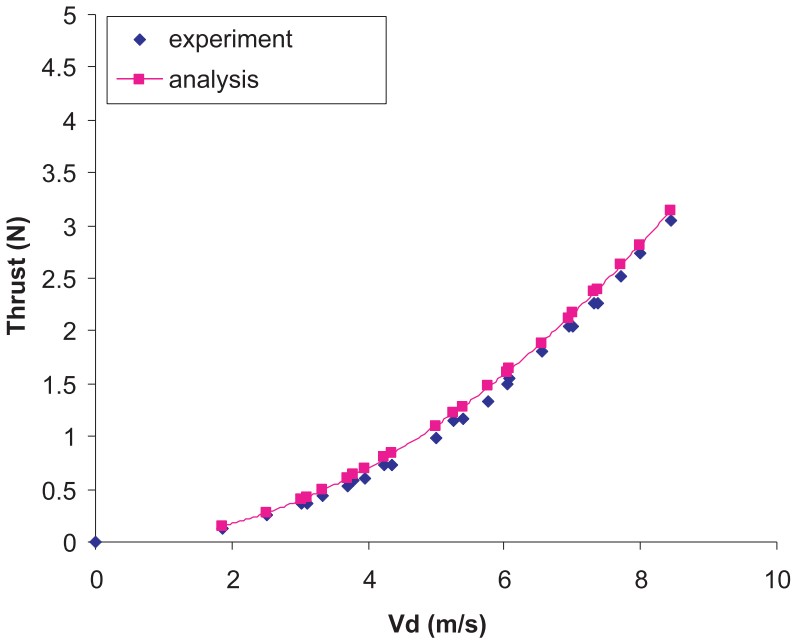

Figure 4.25: Steady state thrust generated by a 2 bladed rotor with a pitch-flap coupling $\delta_3 = -29.74°$, precone $\beta_p = 0°$ and pitch $\theta_0 = -6°$.

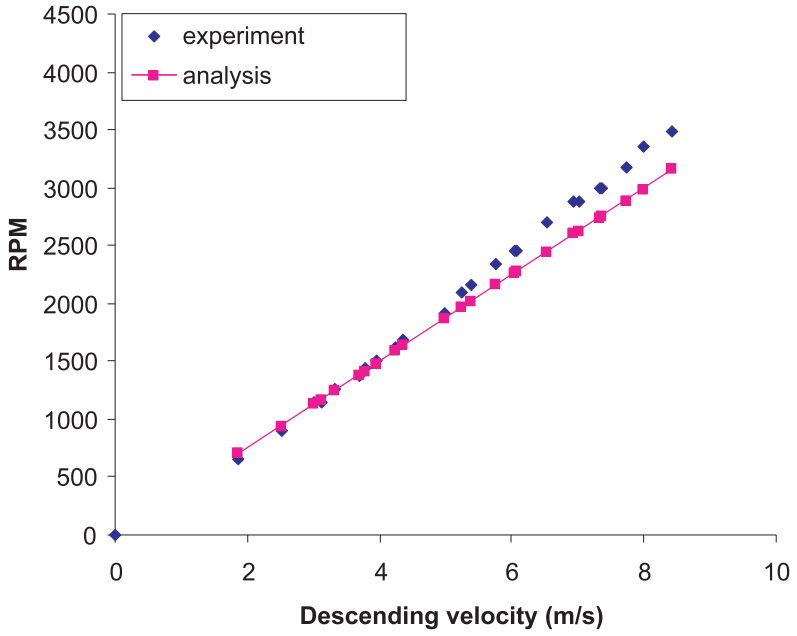

Figure 4.26: Steady state RPM generated by a 2 bladed rotor with a pitch-flap coupling $\delta_3 = -29.74°$, precone $\beta_p = 0°$ and pitch $\theta_0 = -6°$.

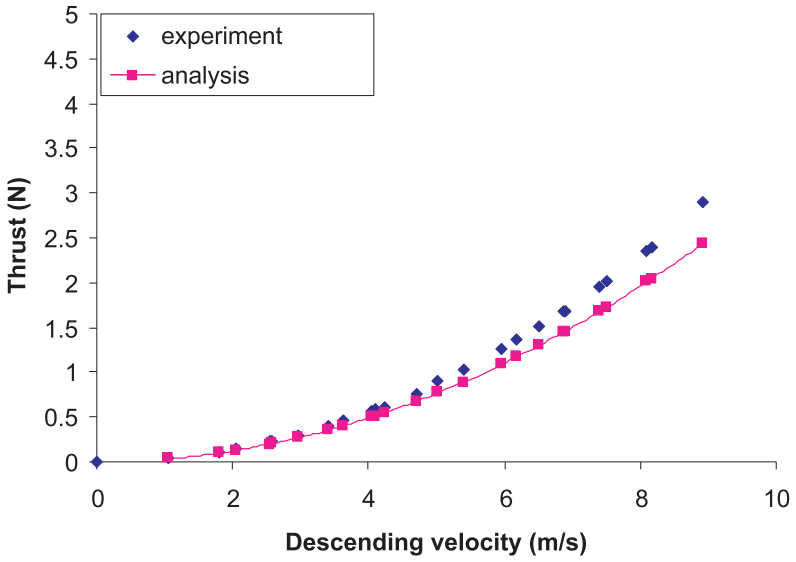

Figure 4.27: Steady state thrust generated by a 2 bladed rotor with a pitch-flap coupling $\delta_3 = -29.74°$, precone $\beta_p = 0°$ and pitch $\theta_0 = -8°$.

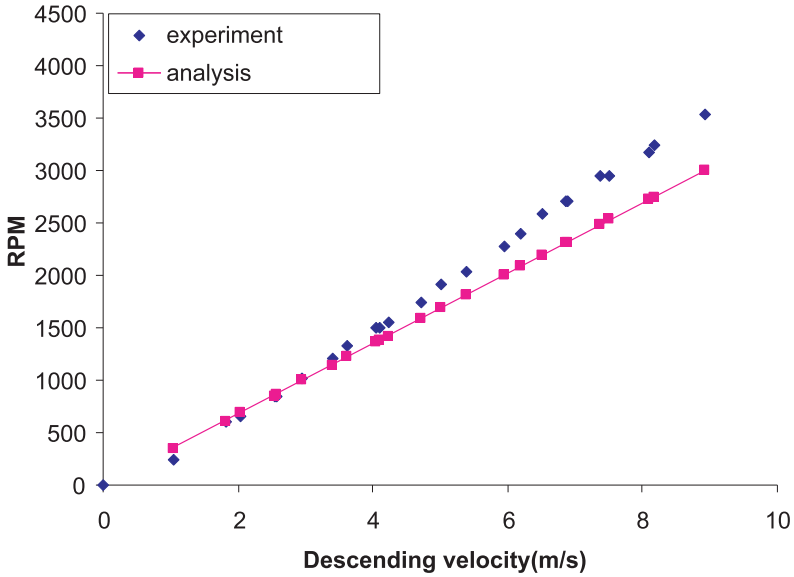

Figure 4.28: Steady state RPM generated by a 2 bladed rotor with a pitch-flap coupling $\delta_3 = -29.74°$, precone $\beta_p = 0°$ and pitch $\theta_0 = -8°$.

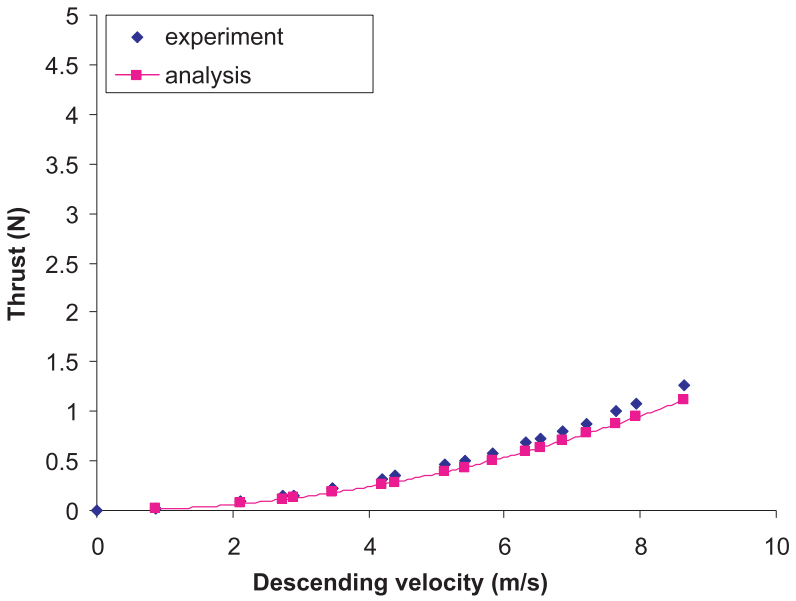

Figure 4.29: Steady state thrust generated by a 2 bladed rotor with a pitch-flap coupling $\delta_3 = -29.74°$, precone $\beta_p = 0°$ and pitch $\theta_0 = -12°$.

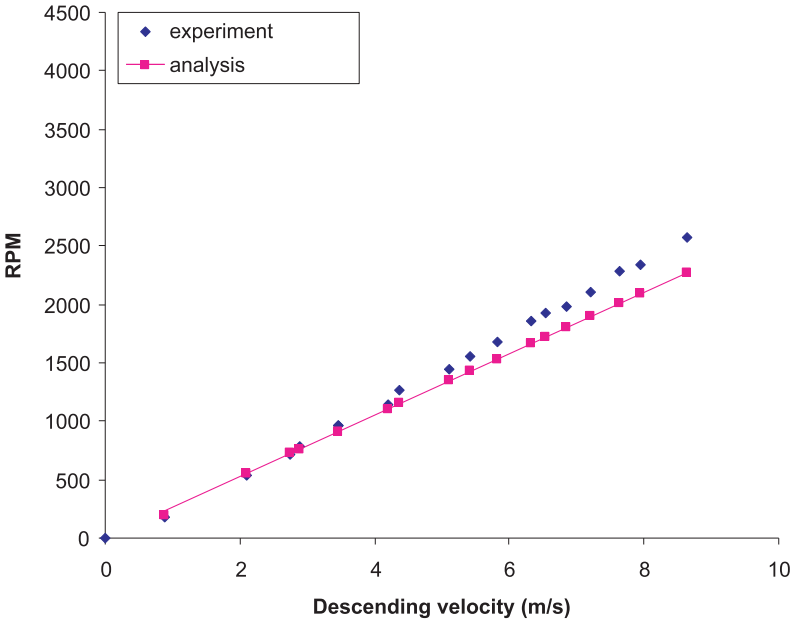

Figure 4.30: Steady state RPM generated by a 2 bladed rotor with a pitch-flap coupling $\delta_3 = -29.74°$, precone $\beta_p = 0°$ and pitch $\theta_0 = -12°$.

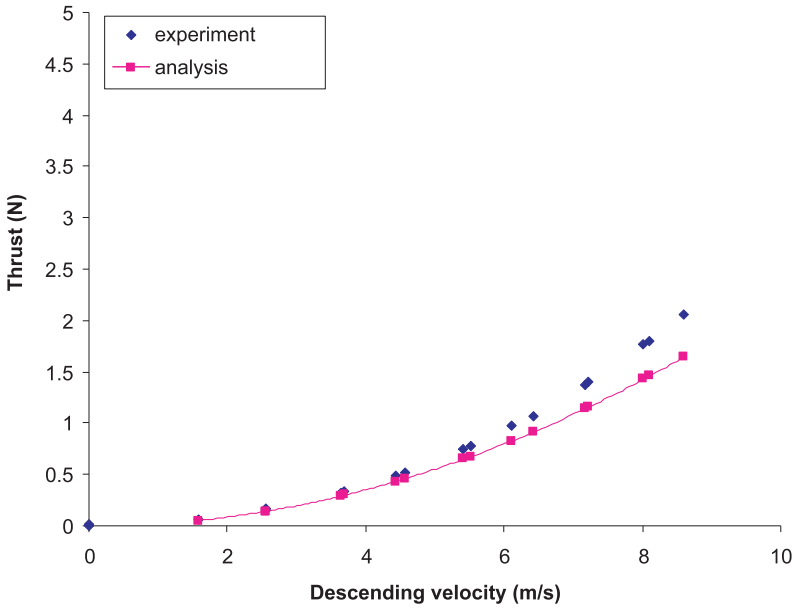

Figure 4.31: Steady state thrust generated by a 2 bladed rotor with a pitch-flap coupling $\delta_3 = -29.74°$, precone $\beta_p = -4°$ and pitch $\theta_0 = -12°$.

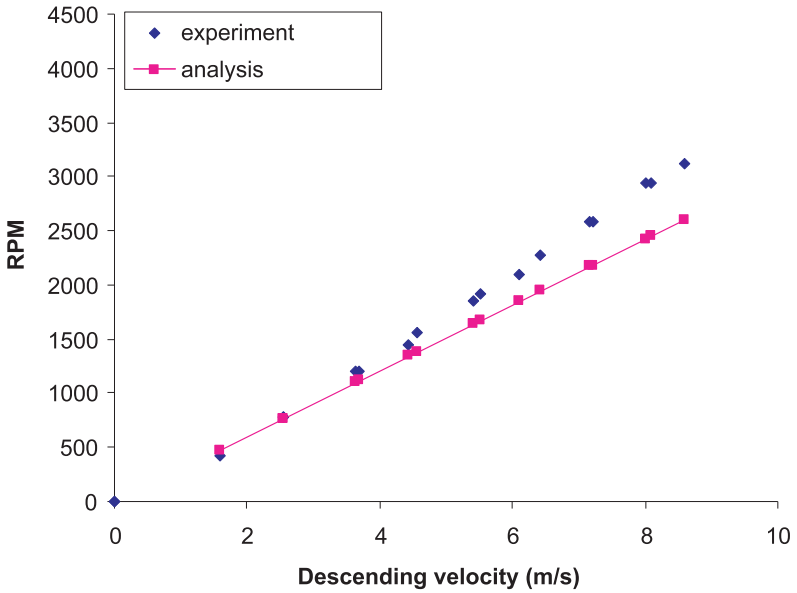

Figure 4.32: Steady state RPM generated by a 2 bladed rotor with a pitch-flap coupling $\delta_3 = -29.74°$, precone $\beta_p = -4°$ and pitch $\theta_0 = -12°$.

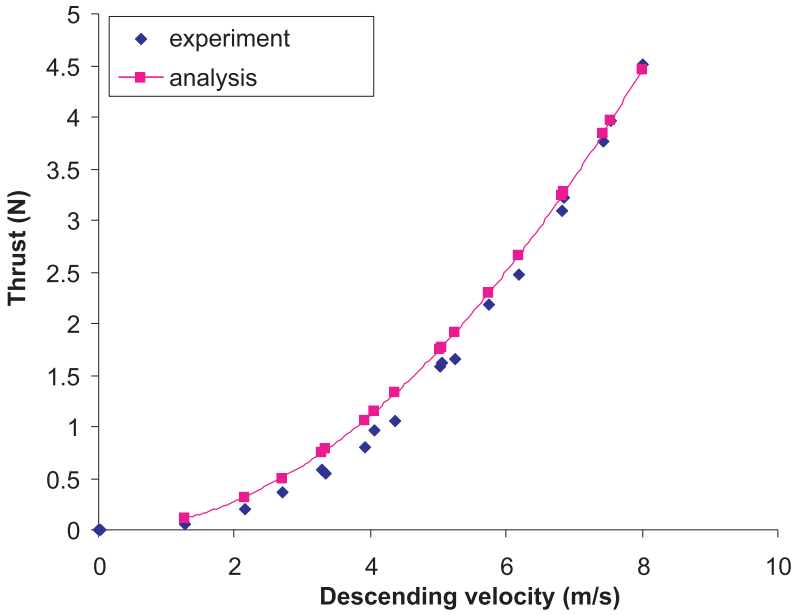

Figure 4.33: Steady state thrust generated by a 2 bladed rotor with a pitch-flap coupling $\delta_3 = -29.74°$, precone $\beta_p = -6°$ and pitch $\theta_0 = -6°$.

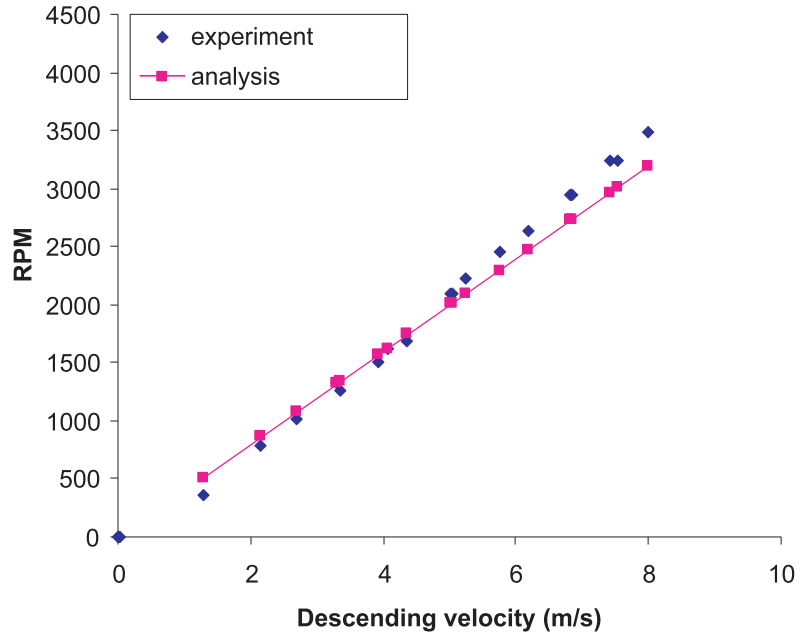

Figure 4.34: Steady state RPM generated by a 2 bladed rotor with a pitch-flap coupling $\delta_3 = -29.74°$, precone $\beta_p = -6°$ and pitch $\theta_0 = -6°$.

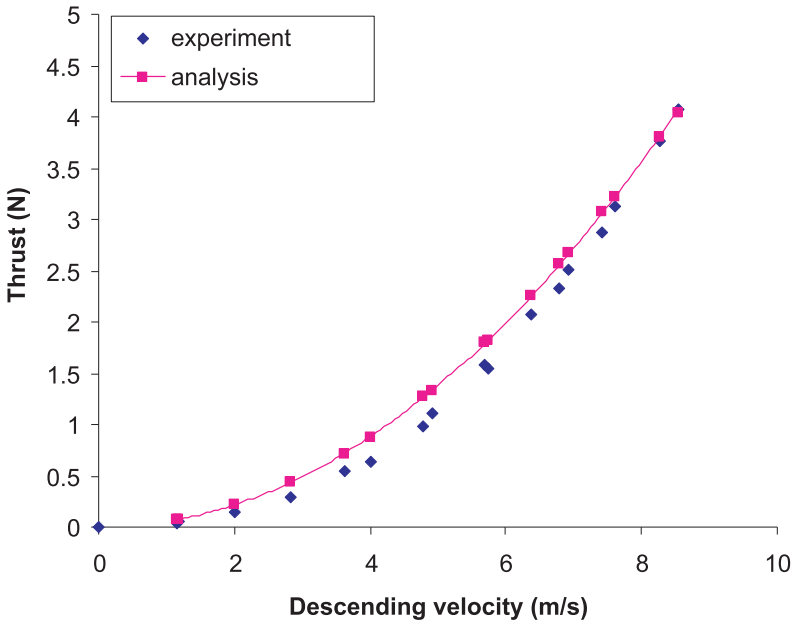

Figure 4.35: Steady state thrust generated by a 2 bladed rotor with a pitch-flap coupling $\delta_3 = -29.74°$, precone $\beta_p = -6°$ and pitch $\theta_0 = -8°$.

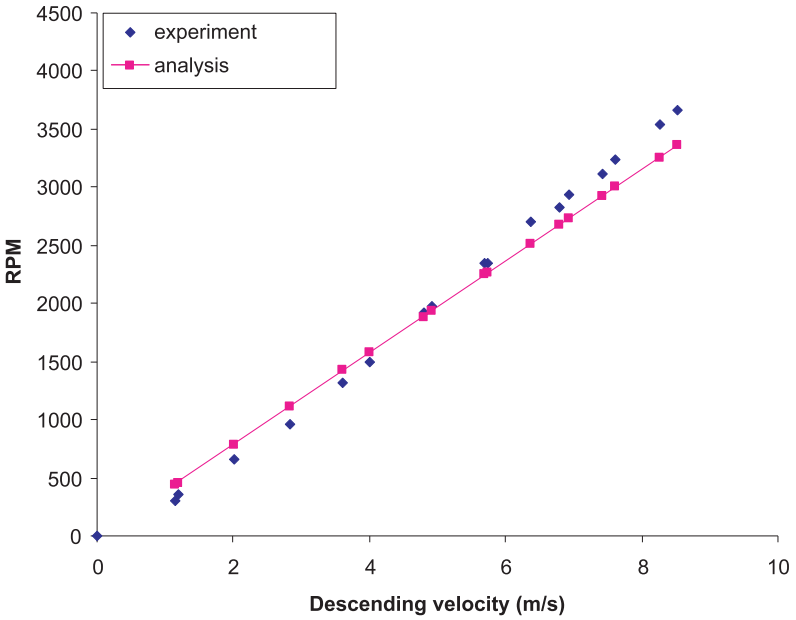

Figure 4.36: Steady state RPM generated by a 2 bladed rotor with a pitch-flap coupling $\delta_3 = -29.74°$, precone $\beta_p = -6°$ and pitch $\theta_0 = -8°$.

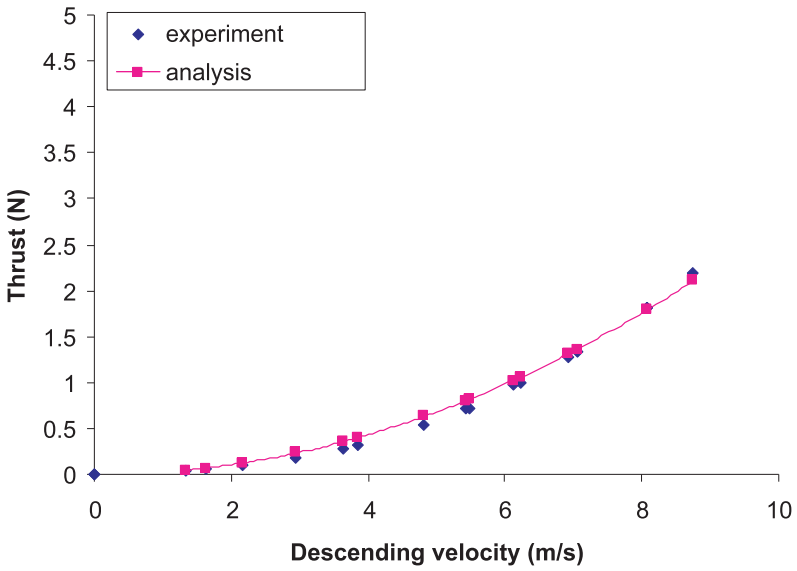

Figure 4.37: Steady state thrust generated by a 2 bladed rotor with a pitch-flap coupling $\delta_3 = -29.74°$, precone $\beta_p = -6°$ and pitch $\theta_0 = -12°$.

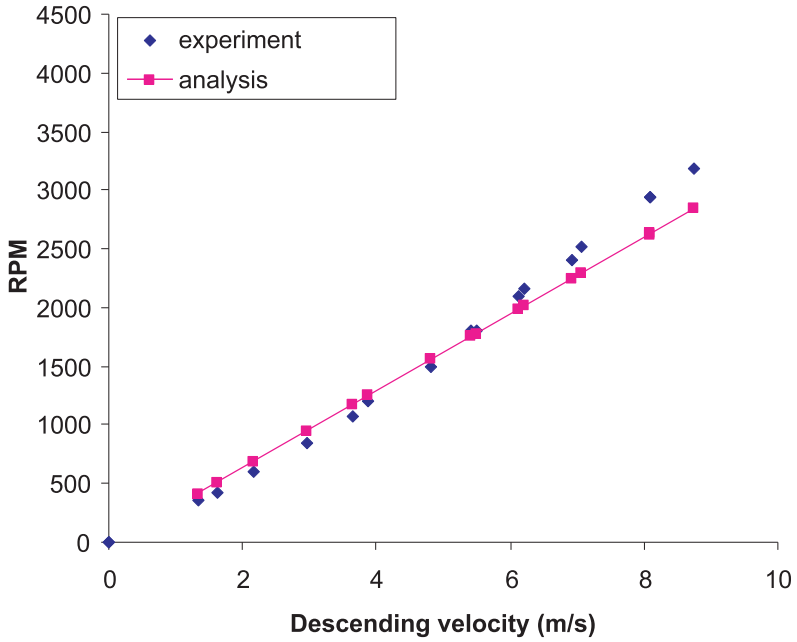

Figure 4.38: Steady state RPM generated by a 2 bladed rotor with a pitch-flap coupling $\delta_3 = -29.74°$, precone $\beta_p = -6°$ and pitch $\theta_0 = -12°$.

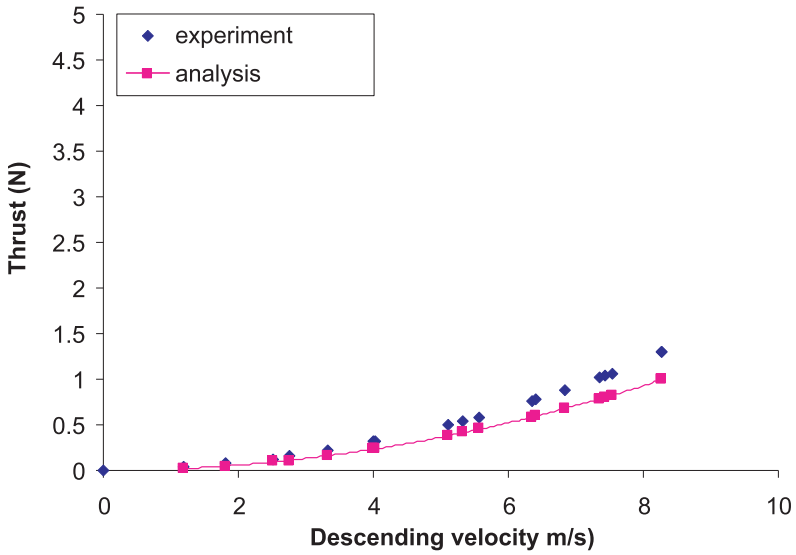

Figure 4.39: Steady state thrust generated by a 2 bladed rotor with a pitch-flap coupling $\delta_3 = -17.33°$, precone $\beta_p = 0°$ and pitch $\theta_0 = -12°$.

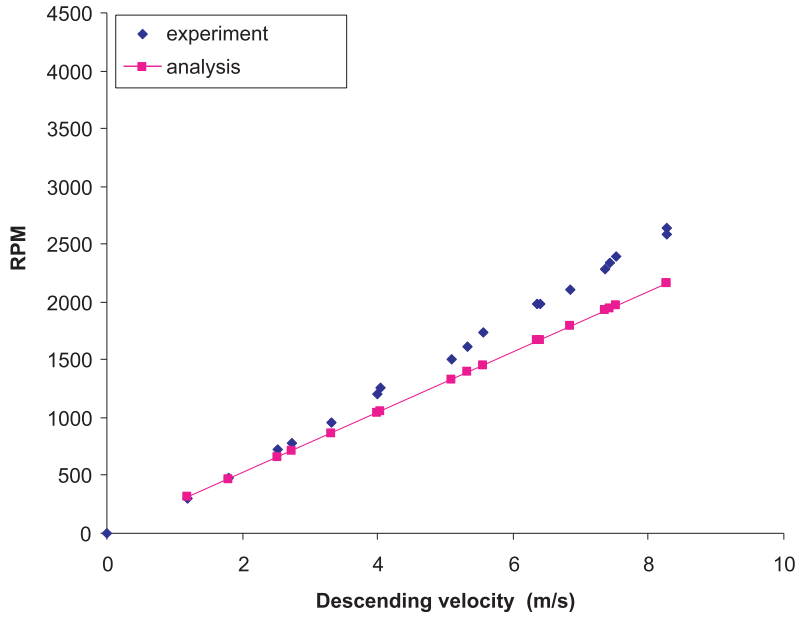

Figure 4.40: Steady state RPM generated by a 2 bladed rotor with a pitch-flap coupling $\delta_3 = -17.33°$, precone $\beta_p = 0°$ and pitch $\theta_0 = -12°$.

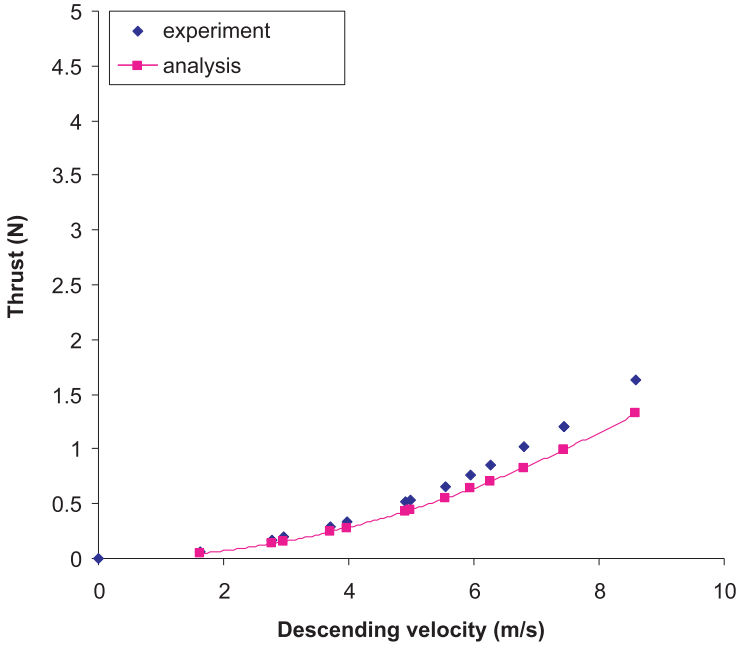

Figure 4.41: Steady state thrust generated by a 2 bladed rotor with a pitch-flap coupling $\delta_3 = -17.33°$, precone $\beta_p = -4°$ and pitch $\theta_0 = -12°$.

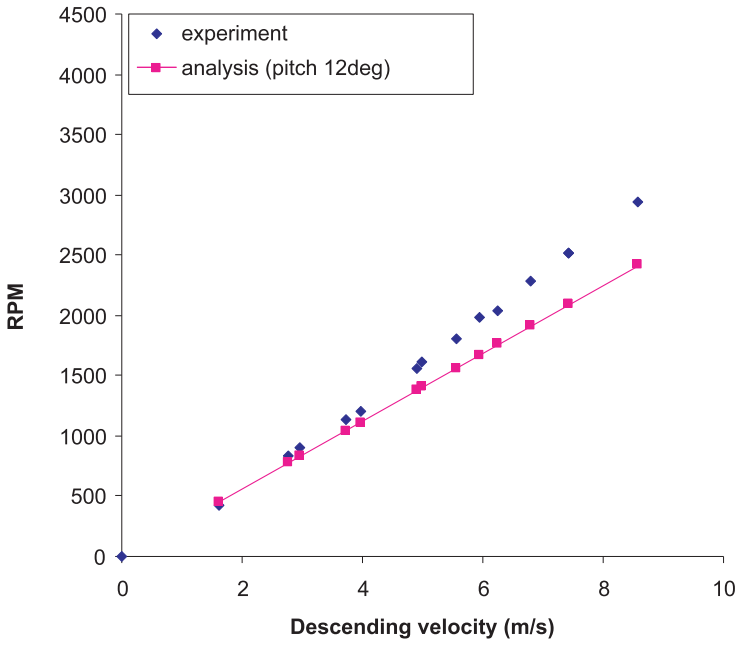

Figure 4.42: Steady state RPM generated by a 2 bladed rotor with a pitch-flap coupling $\delta_3 = -17.33°$, precone $\beta_p = -4°$ and pitch $\theta_0 = -12°$.

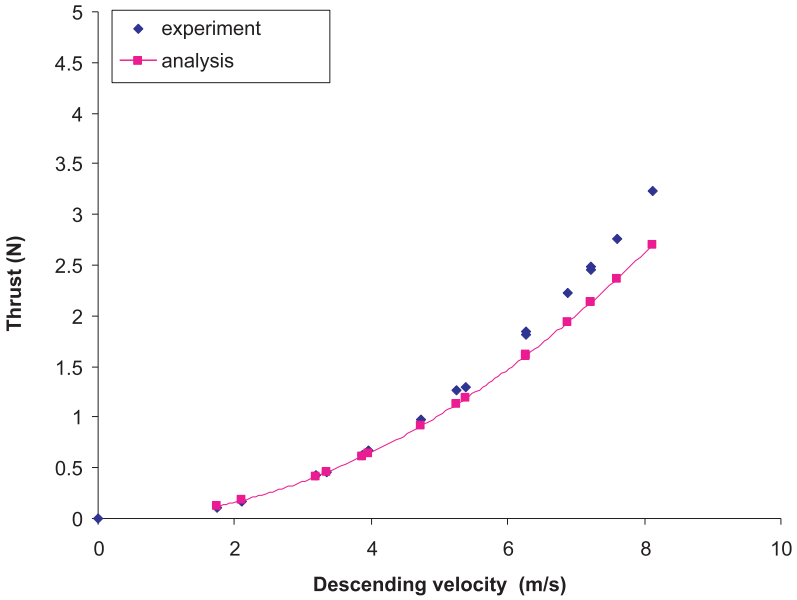

Figure 4.43: Steady state thrust generated by a 2 bladed rotor with a pitch-flap coupling $\delta_3 = -17.33°$, precone $\beta_p = -6°$ and pitch $\theta_0 = -8°$.

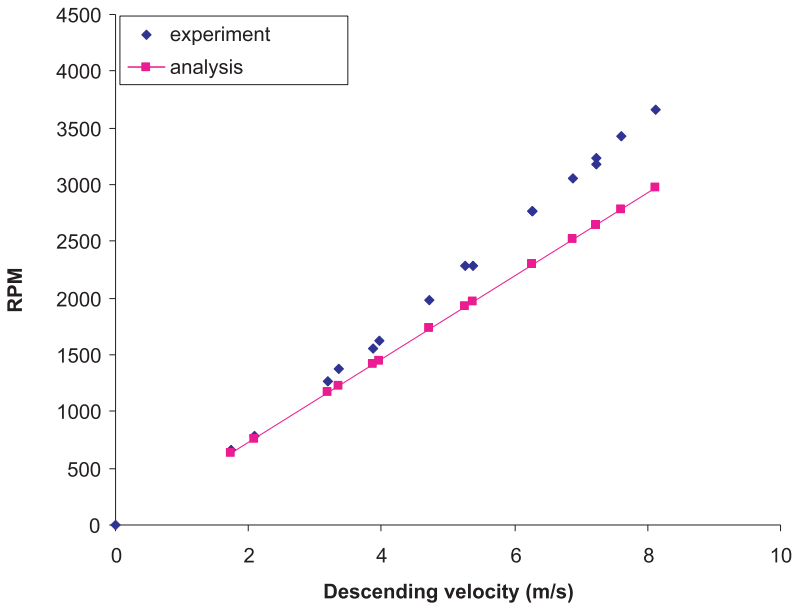

Figure 4.44: Steady state RPM generated by a 2 bladed rotor with a pitch-flap coupling $\delta_3 = -17.33°$, precone $\beta_p = -6°$ and pitch $\theta_0 = -8°$.

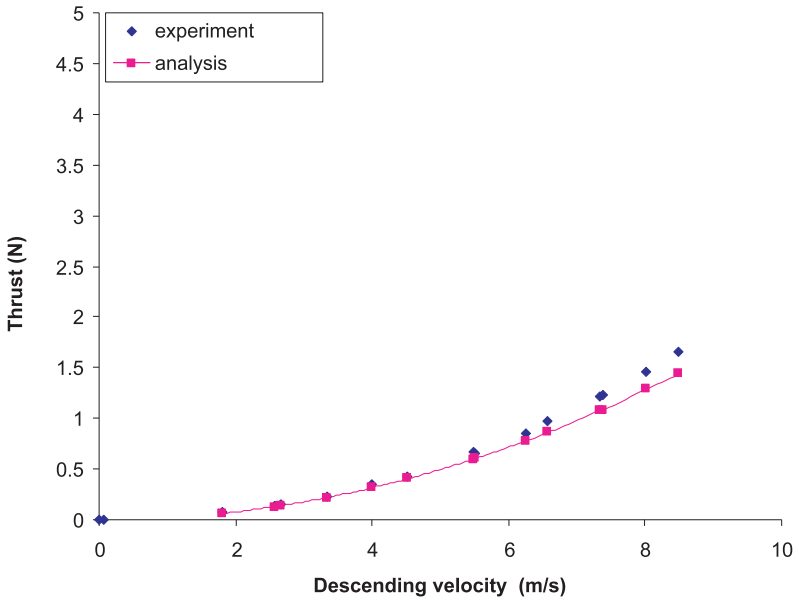

Figure 4.45: Steady state thrust generated by a 2 bladed rotor with a pitch-flap coupling $\delta_3 = -17.33°$, precone $\beta_p = -6°$ and pitch $\theta_0 = -12°$.

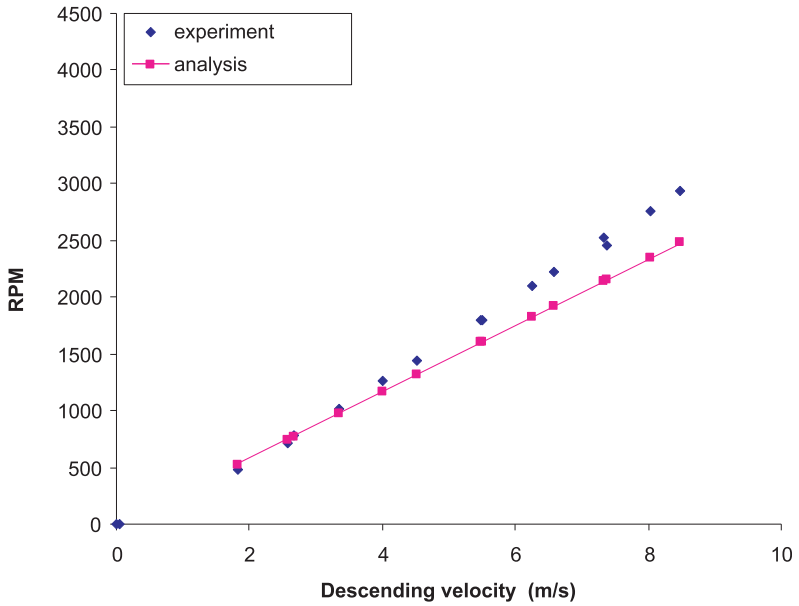

Figure 4.46: Steady state RPM generated by a 2 bladed rotor with a pitch-flap coupling $\delta_3 = -17.33°$, precone $\beta_p = -6°$ and pitch $\theta_0 = -12°$.

4.9 Parametric study

The steady state RPM and thrust values obtained from the wind tunnel tests gave an understanding of the behavior of the system and of the influence of the initial collective pitch, pitch-flap coupling and precone angles. The RPM Sweep Method, validated with the wind tunnel results, can be used to investigate the influence of different parameters on the steady state thrust and RPM. The different parameters studied are the:

1. Blade pitch, θ_0.
2. Pitch-flap coupling angle, δ_3.
3. Precone angle, β_p.
4. Blade mass m_b.

The effect of the airstream velocity V_d is not investigated as the maximum V_d is specified as 15 ft/s for the full scale Autobody. A constant value $V_d = 19.6$ ft/s is assume to perform the present study. The parametric study is carried out by varying only one of these parameters at a time from the baseline case. The baseline case is chosen as:

1. Blade pitch, $\theta_0 = -12°$.
2. Pitch-flap coupling angle, $\delta_3 = -17.33°$.
3. Precone angle, $\beta_p = -6°$.
4. Blade mass $m_b = 0.0052$ kg.

4.9.1 Influence of the pitch angle,θ_0

Figure 4.47 shows the steady state thrust and RPM for the following values of pitch: $-4°$, $-6°$, $-12°$ and $-14°$. From these two figures, it can be noted that thrust and RPM increase with less negative pitch. This trend is the same as the experimental trends observed in section 4.7. It can be seen that the trend is monotonic and no optimum value exists. Therefore, the value chosen for

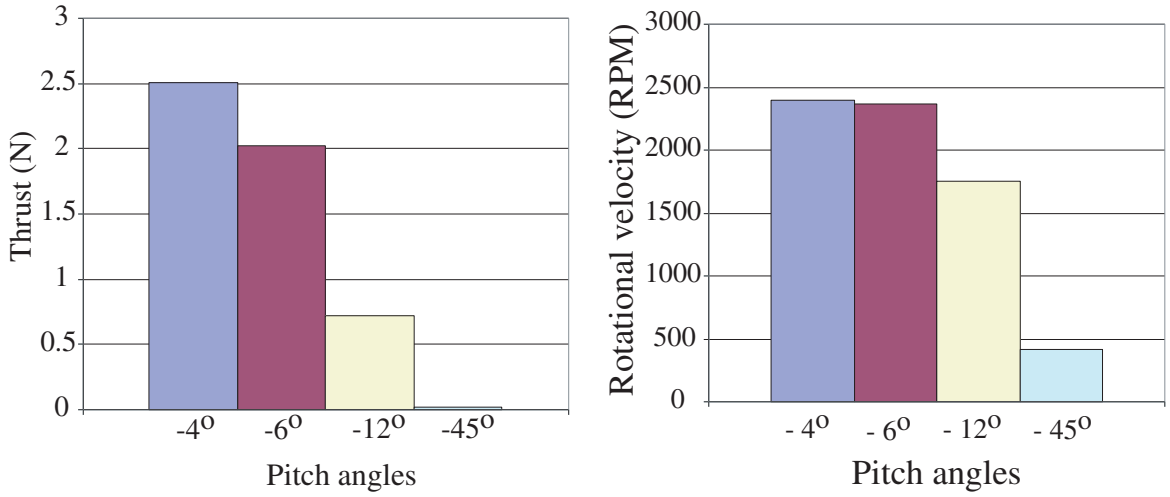

(**a**) Thrust

(**b**) RPM

Figure 4.47: Thrust and rotational velocity for different pitch angles.

the fullscale Autobody must include several other mechanical considerations. An optimum value of pitch, for the full scale Autobody should be chosen as less negative as possible to maximize the thrust. However, note that the pitch at $\frac{3}{4}$ radius should be less than zero to initiate the rotor rotation in the correct direction.

4.9.2 Influence of the pitch-flap coupling angle, δ_3

Figure 4.48 shows the thrust and RPM obtained for $\delta_3 = -6°$, $\delta_3 = -17.33°$, $\delta_3 = -34.66°$, $\delta_3 = -45°$ and $\delta_3 = -50°$. It can be seen that the thrust and RPM increase with more negative δ_3 angle. Again, the trend is monotonic and no optimum value exists. However, for δ_3 angles more negative than $-50°$, the analysis showed that the blade stalled. Therefore, the optimum δ_3 value for the Autobody was chosen to be $-45°$ to avoid stall and achieve a high steady state thrust.

4.9.3 Influence of the precone angle, β_p

Figure 4.49 presents the thrust and RPM obtained for values of precone: $0°$, $-4°$, $-6°$, $-12°$ and $-30°$. The value of the other parameters are from the baseline case, for instance $\delta_3 = -17.33°$. It can be noted that the thrust and RPM increase for more negative precone angle. As for the pitch and δ_3 cases, the trend is monotonic and no optimum value exists. An ideal value of precone

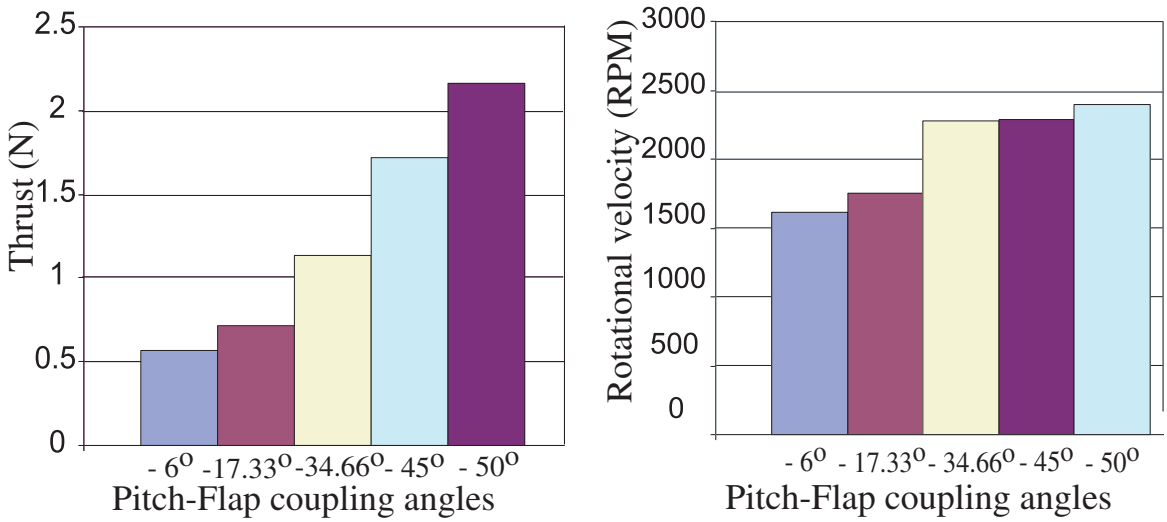

(**a**) Thrust

(**b**) RPM

Figure 4.48: Thrust and rotational velocity for different pitch-flap coupling angles.

for the Autobody would be as negative as possible. However, a large precone would result in a decrease in disk area and high stresses at the blade root.

4.9.4 **Influence of the blade mass,** m_b

Figure 4.49 presents the values of thrust and RPM computed for blade masses of 0.0052 kg, 0.0104 kg, 0.1 kg and 1 kg. It can be noted that the thrust and RPM decrease as the blade is heavier. Again, the trend is monotonic and no optimum value exists. An optimum value for the blade mass of the Autobody would be the smallest possible. In order to lower the blade mass, a low density foam could be chosen. However, care must be taken that such density foam does not result in a too low blade stiffness.

From the above parametric study, the thrust and RPM increase for:

1. Less negative pitch.
2. More negative pitch-flap coupling.
3. More negative precone angle.
4. Lighter blades.

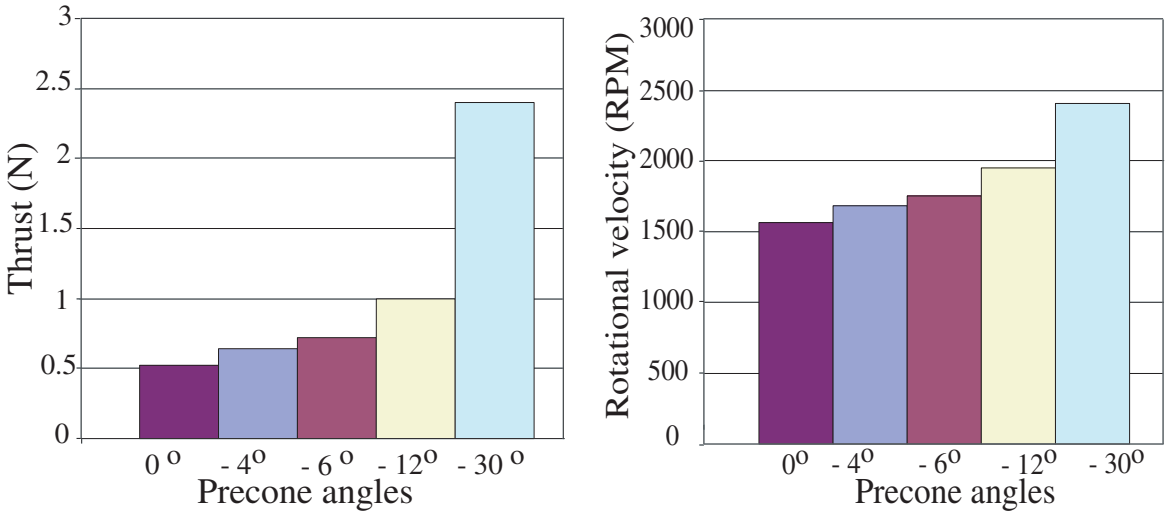

(**a**) Thrust

(**b**) RPM

Figure 4.49: Thrust and rotational velocity for different precone angles.

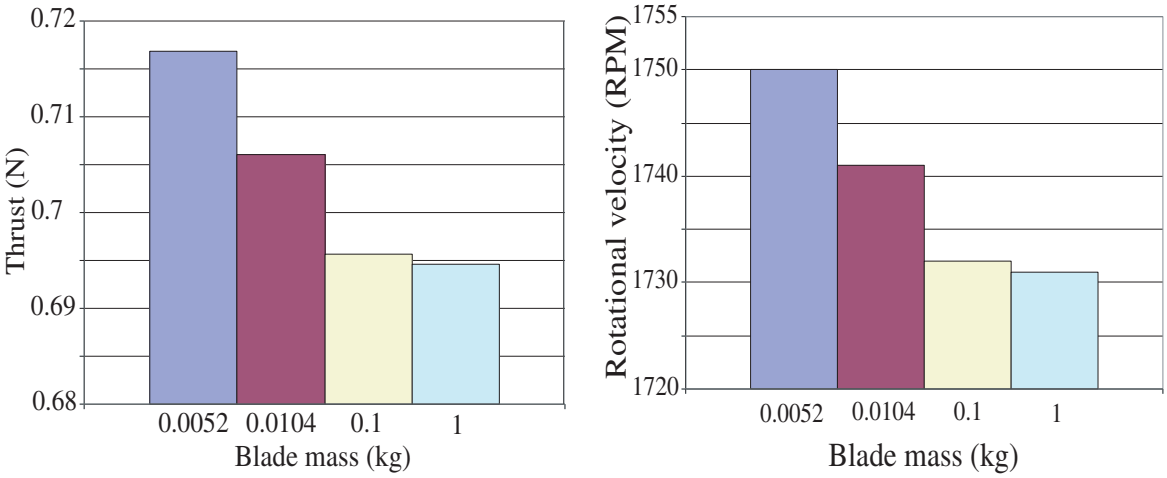

(**a**) Thrust

(**b**) RPM

Figure 4.50: Thrust and rotational velocity for different blade masses.

Table 4.5: Qualitative effect of the parameters on steady state rotational velocity Ω and thrust T.

Parameter variation	Ω	T
$\lvert\theta_0\rvert \uparrow$	$\downarrow$	$\downarrow$
$\lvert\delta_3\rvert \uparrow$	$\uparrow$	$\uparrow$
$\lvert\beta_p\rvert \uparrow$	$\uparrow$	$\uparrow$
$m_b \uparrow$	$\downarrow$	$\downarrow$

Table 4.6: Parameters influence on steady state rotational velocity Ω and thrust T.

Parameter	Parameter variation (%)	Ω variation (%)	T variation (%)
θ_0	100	25	63
δ_3	100	30.2	58.3
β_p	100	11.7	39
m_b	100	0.51	1.5

Note that the trends of the parametric study are same as the experimental trends.

The qualitative effect of the parameters is summarized in Table. 4.5. Clearly, the analysis captures the expected physically consistent trends mentioned above.

In addition, it should be noted that the quantitative influence of each parameter on the steady state rotational velocity and thrust is different. Table. 4.6 presents the variation in percentages of the steady state rotational velocity and thrust for a change of 100% in each parameter from the baseline values. It can be seen that the parameters with the greatest influence on rotational velocity and thrust are the δ_3 angle and the blade pitch. The precone and the blade mass have less important influence on the thrust and RPM.

Chapter 5

Flight tests

This chapter describes the construction and testing of the full scale prototype called the Autobody. The RPM Sweep analysis validated in Chapter 4, was used to design the full scale configuration to minimize the descending velocity. This full scale configuration was flight tested with on-board instrumentation to measure the descending velocity V_d and the rotor RPM Ω. The test set-up and results of the flight tests are discussed. Finally, the experimental data is compared with the analytical predictions.

5.1 Prototype construction

The full scale model was designed to satisfy the operational requirements discussed in Chapter 1. It was constituted of a 48-inch rotor diameter and a fuselage big enough to contain the instrumentation. The full scale rotor, shown in Figure. 5.1, was designed with the same features as the model rotor. The implementation of these features on the full scale rotor is described below.

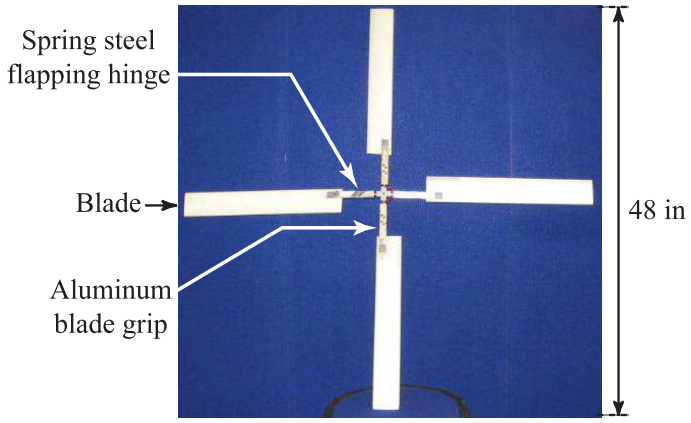

Figure 5.1: Full scale rotor

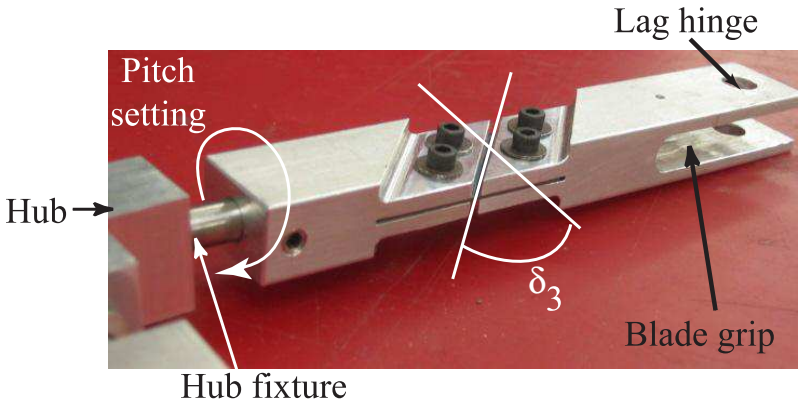

Figure 5.2: Blade grip of the full scale rotor with a δ_3 of $-45°$ at flap hinge.

5.1.1 Hub and grips

The full scale rotor was equipped with the rotor features mentioned previously, i.e., negative collective pitch at the root, negative precone $\beta_p = -4°$ and a negative pitch-flap coupling angle $\delta_3 = -45°$. Bench-top tests were conducted to measure accurately the value of the δ_3 angle: it was found to be $-41°$ instead of the designed value of $-45°$. The technical drawings of the full scale hubs are shown in Appendix A.4 and A.5.

The blade grips of the full scale rotor consist of two parts, linked by a clamped spring steel sheet as shown in Figures 5.2 and 5.3. This assembly constitutes the δ_3 hinge. The same δ_3 angle was maintained on all the four blades to keep the rotor balanced. The flapping stiffness of the hinge could be changed by varying the thickness and clamped length of the spring steel sheet. It was observed that varying the stiffness by changing the length of the spring steel sheet did not guarantee the exact same δ_3 angle for all the four blades. It was preferred to modify the stiffness by varying the thickness of the spring steel (Figure. 5.3). The technical drawings of the full scale blade grip are shown in Appendix A.6. A lag hinge was also incorporated in the full scale grip. The blade was allowed to lag in flight and rotate about this hinge to absorb the energy on impact during landing. This was expected to increase the survivability of the blades. The pitch is adjustable by rotating the grip around the hub fixture as seen in Figure 5.2. Because of the hub and grip design, the only test variables are:

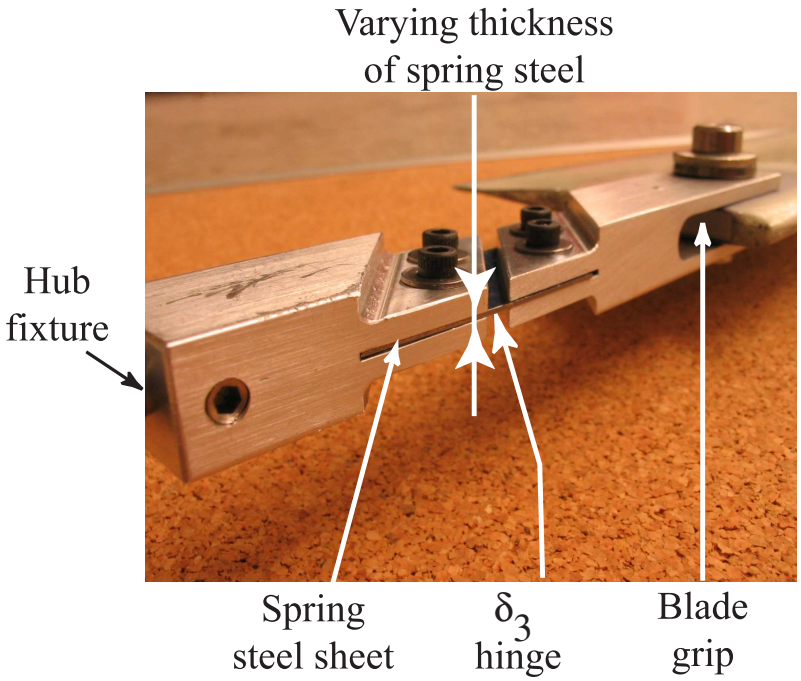

Figure 5.3: Close view of the full scale blade grip with the δ_3 hinge formed of spring steel.

1. The hinge stiffness, k_β

2. The collective pitch at the root, θ_0

3. The blade mass, m_b

5.1.2 Blades

A full scale blade is shown in Figure 5.4. The blades have a positive twist of 7.75°, that was defined by the available mold used to manufacture the blades. In order to initiate rotor rotation in the correct direction, the initial collective pitch at 75% span must be negative, i.e. $\theta_{0.75} < 0$. Therefore, the pitch at the root must meet the following requirement:

$$\theta_0 \leq -5.8^\circ \tag{5.1}$$

The mold used is 31″ long and has a twist of 12° from root to tip (Figure 5.5). Three kinds of blades were constructed:

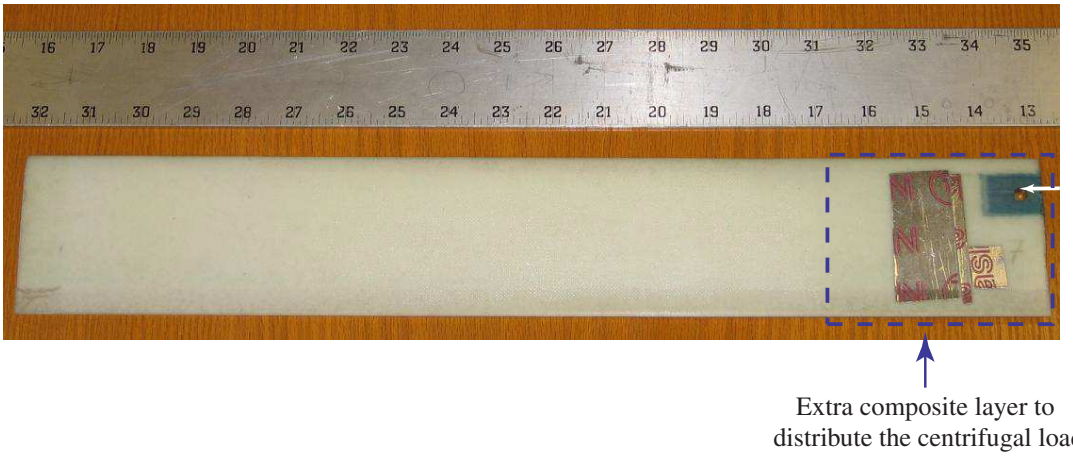

Figure 5.4: Close view of a full scale blade.

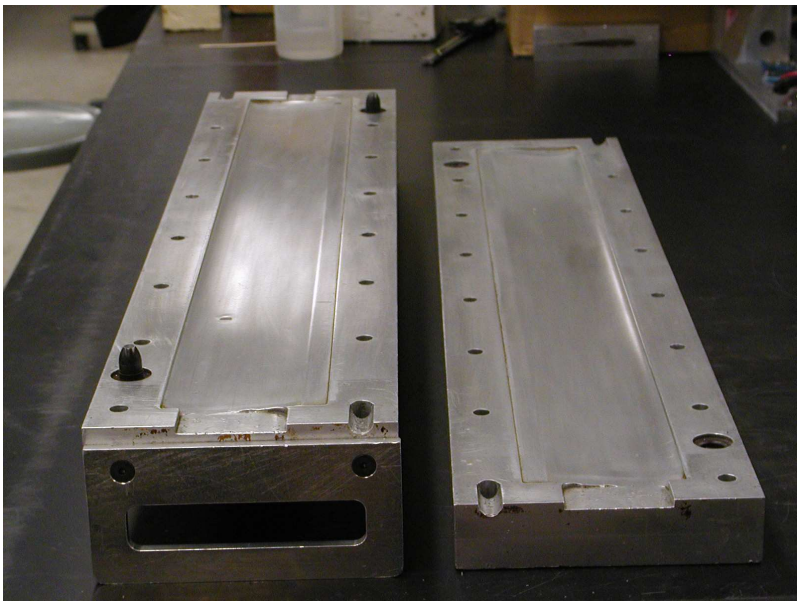

Figure 5.5: SC1095 mold used to manufacture the full scale blade.

1. The first generation of blades were constructed from 71-Rohacell foam of 75 kg/m^3 density (Ref. [14]) wrapped in fiberglass. An aluminum insert was placed at the root of the blade to ensure it was safely clamped in the blade grip (Figure 5.4). The insert was carefully positioned to ensure the blade was attached to the blade grip at the blade quarter chord. The foam core was wrapped at the root with fiberglass to evenly distribute the centrifugal load (Figure 5.4). The whole foam core was then covered with two plies of cross-ply fiberglass. The foam core had the same curing process as for the model scale blades. However, the curing temperature for the fiberglass is 250°F. The finished blade chord was 3 in and the span was 20 in. Each blade weighed 84.6 grams (Table 5.1).

2. The second generation of blades were manufactured with 31-Rohacell foam of 25 kg/m^3 density covered with fiberglass. Similar to the first generation of blades, the second generation blades included an aluminum insert placed at the root with two plies of fiberglass. The blade chord and span were kept identical. Each blade weighed 61.3 grams (Table 5.1).

3. The third generation of blades were built using 31-Rohacell foam wrapped in $IM7$ carbon weave in order to reduce the weight of the blade and to increase its stiffness. A unidirectional carbon fiber insert was located at the root of the blade. The unidirectional fibers were aligned with the centrifugal force direction to allow for a lighter insert capable of taking the whole centrifugal load. The blade root was covered with ±45° carbon weave to spread the centrifugal load on a larger area than the insert. The whole foam core was then wrapped in two plies of ±45° carbon weave. The blade chord and span were identical to the first generation blades. The third generation blades weighed 70.2 grams (Table 5.1). 200-grit sand paper was attached on the blade root surface, near the lag hinge, to generate friction between the blade and the blade grip. This is expected to increase the energy dissipated during landing, thereby increasing the blade survivability.

The parameters of the full scale blades are summarized in Table 5.1. Decreasing the weight of the blades was expected to have two benefits. Firstly, the lighter blades would have a lower inertia, and therefore speed up faster. Secondly, with a lighter rotor, the vehicle would have a lower center

Table 5.1: Full scale rotor characteristics

Rotor diameter (in)	48
Blade number, N_b	4
Blade span (in)	20
Blade chord (in)	3
Blade twist (deg/in)	.387
Blade mass (kg)	84.6 (1^{st} generation)
	61.3 (2^{nd} generation)
	70.2 (3^{nd} generation)
Airfoil	SC 1095
Pitch-flap coupling angle, δ_3 (deg)	-41
Precone angle, β_p (deg)	-4

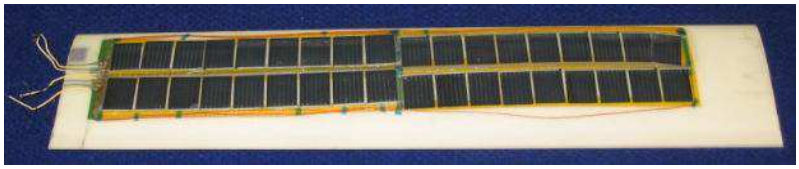

Figure 5.6: Full scale blade with embedded solar cells.

of gravity, therefore increasing the stability of the vehicle during the initial stages of release.

The Autobody is envisaged to carry on-board instrumentation to the field of operation. The payload has to function autonomously for a considerable amount of time. One way to provide power to the payload after deployment is via solar cells embedded on the surface of the blades as shown in Figure 5.6. The cells are electrically connected to the hub by a soldering terminal (see Figure 5.7). Several such blades were constructed to investigate the feasibility of embedding solar cells in a composite blade. It was found that the mass of these blades increased by approximately 20%, but the structural integrity was maintained. Care should be taken to prevent the cells from breaking during the curing phase. However, none of the blades with embedded solar cells was used in the flight tests.

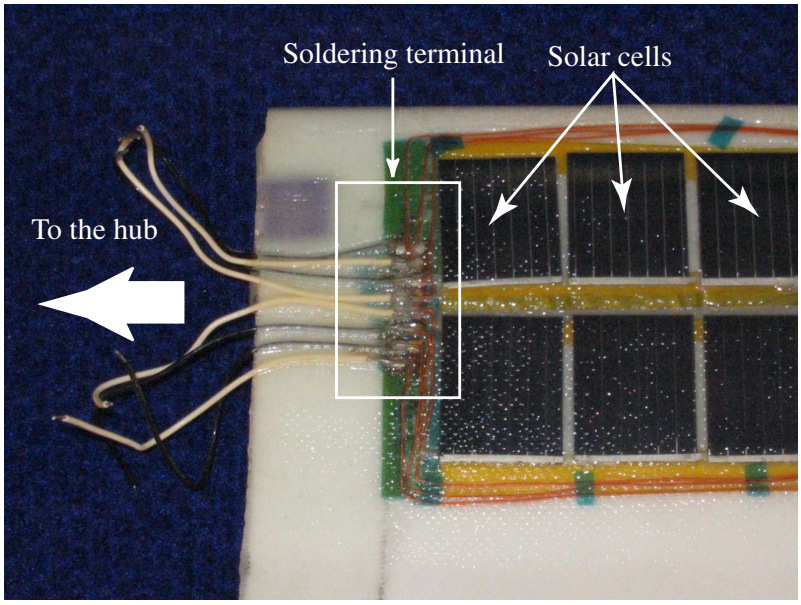

Figure 5.7: Close view of the solar cells connections.

Table 5.2: Fuselage characteristics

	Fuselage diameter (in)	Fuselage length (in)	Bottom Shape	Vanes	Counterweight (g)
Fuselage 1	4.19	5	Bluff	None	65
Fuselage 2	.25	24	Bluff	None	117.4
Fuselage 3	2.67	25	Nose cone	3	200
Fuselage 4	4.19	24	Round nose	3	765

5.1.3 **Rotor/fuselage assembly**

The Autobody must be designed such that it aligns itself in the right orientation (i.e. rotor shaft vertical, rotor on top), regardless of how it is dropped from the aircraft. In order to study the dynamics of the Autobody after its release and to determine the influence of various design parameters on the autorotative performance, three different vehicle configurations (Figure 5.8) were studied using the model scale rotor and three fuselage combinations. The dimensions of the three fuselage models are tabulated in Table 5.2.

The first configuration was dropped from the top of a tall building. It was observed that

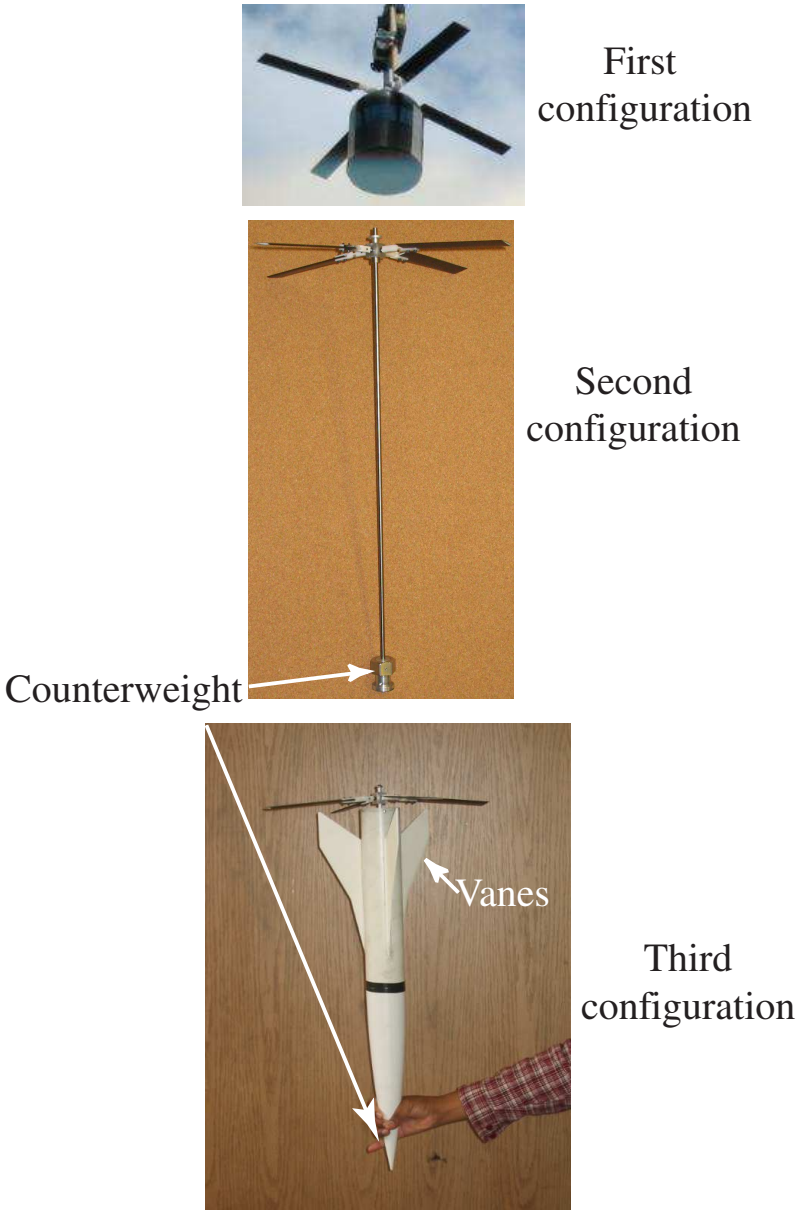

Figure 5.8: First three generation of experimental prototypes.

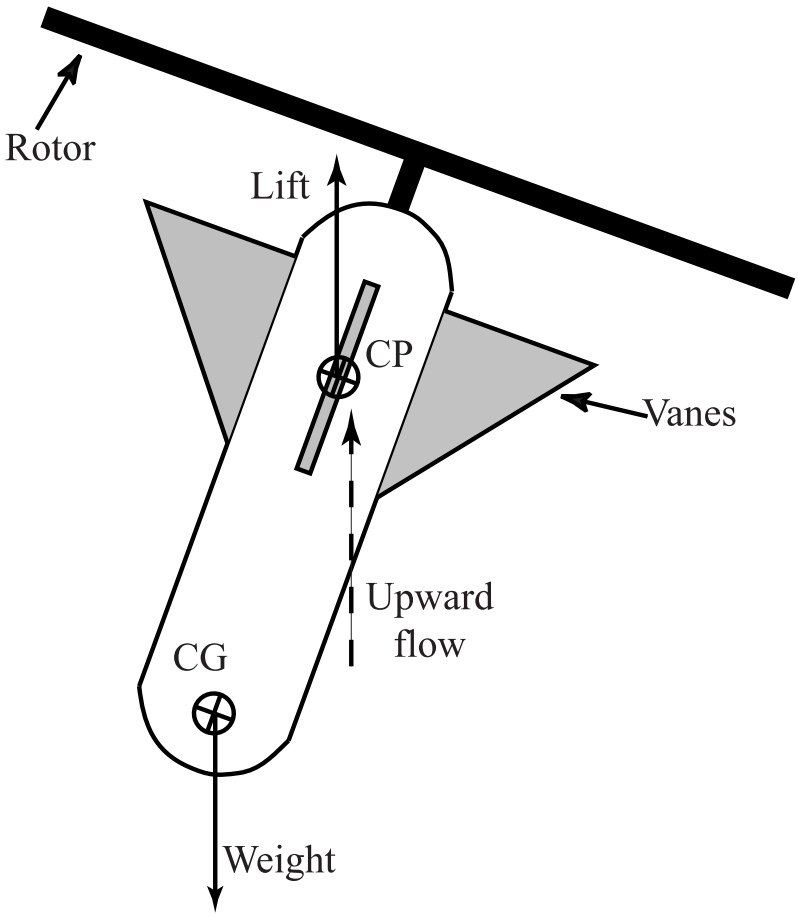

Figure 5.9: Forces affecting initial stability of the vehicle.

this configuration was unstable after release and the system tumbled before landing. The second configuration was built to identify whether the cause of the tumbling was the rotor or the fuselage. This second design consists of the same rotor as the first configuration but mounted on a long and slender shaft representing the fuselage. A counterweight was attached at the bottom of the shaft (Figure 5.8). This model was dropped from the same height. It was observed that the model was stable. Therefore, the vehicle must be slender and feature a low center of gravity to increase the vehicle stability. The third configuration included those characteristics as well as vanes. Figure. 5.9 shows that if the vehicle is angled with respect to the vertical, the reaction on the vanes will generate a lift and create a moment about the center of gravity of the vehicle which will help the Autobody to align itself vertically. This model was dropped from a helicopter (Figure 5.11) and was found to be stable throughout its flight.

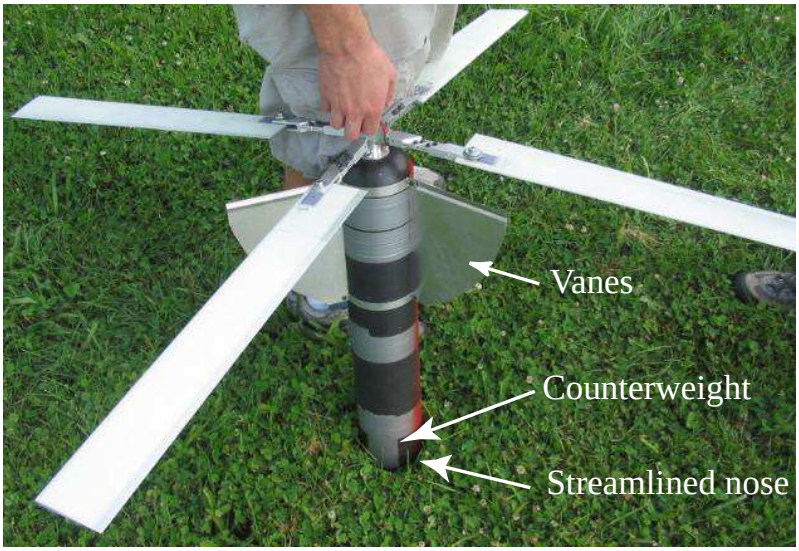

Figure 5.10: Full scale Autobody configuration.

Figure 5.11: Drop test of the third configuration from a helicopter.

Based on the tests performed on the first three configurations, it was determined that the initial release dynamics are important. The vehicle must be prevented from tumbling when the rotor is producing low thrust. As the rotor speeds up and generates more thrust, the effect of the aerodynamic forces on the fuselage become less important. In order to increase the stability of the vehicle in the initial stages of release, and to make it fall in a vertical orientation, the center of gravity (C.G.) of the vehicle must be as low as possible. This is shown schematically in Figure. 5.9. The addition of a counterweight at the bottom of the cylindrical fuselage helps to lower the C.G. of the vehicle. Therefore, the design of the full scale model requires:

1. A counterweight at the bottom of the fuselage to lower the center of gravity (C.G.) (see Fig. 5.9).

2. Vanes that stabilize the system and align the Autobody vertically if it deflects from the vertical before the rotor spins up (Fig. 5.9).

3. A nose cone that streamlines the flow and reduces the drag on the fuselage.

The full scale prototype was developed incorporating the above three concepts and is shown in Fig. 5.10. The fuselage was a long cylindrical body terminated by a heavy round nose. This configuration was tested successfully in three drop tests.

5.2 Full scale flight tests

5.2.1 Goal

The full scale prototype must land safely so the payload is not damaged upon landing. Therefore, the optimum full scale configuration is required to achieve a steady state rate of descent lower than 15 ft/s. The design was determined based on the validated analysis with additional mechanical considerations. The prototype is then tested to:

1. Verify that the desired rate of descent is attained.

2. Compare the analytical predictions and experimental data.

Figure 5.12: Autobody instrumented drop test performed from a hot air balloon.

5.2.2 Test platform

The full scale prototype was dropped from a hot air balloon. The balloon was not tethered and was not powered (Figure. 5.12). Its flight speed and direction were determined by the prevailing wind. The testing procedure consisted of ascending to a predetermined height in the balloon and then releasing the prototype to fall under gravity. The data was recorded during the drop by an on-board data-logger and was downloaded off the Autobody to a notebook computer after landing. After each drop, the balloon descended to the ground to pick up the Autobody for the next drop.

5.2.3 Instrumentation

On-board instrumentation was installed to acquire rotor RPM, acceleration along the rotor shaft axis and height data. To this end, the following sensors were installed in the fuselage :

1. A Hall switch was used to measure RPM. A magnet was attached to a holder which was mounted on the rotor shaft (Figure. 5.13). The blades, hub, shaft and magnet are rotating whereas the fuselage, bearing block and Hall switch are fixed. The motion of rotation was transmitted to the inside of the fuselage where it was safe to install the magnet and Hall switch. From the time period of the square wave output of the Hall switch, the RPM could be measured.

2. An $ADXL-202$ two-axis accelerometer [15] senses acceleration along two orthogonal axes.

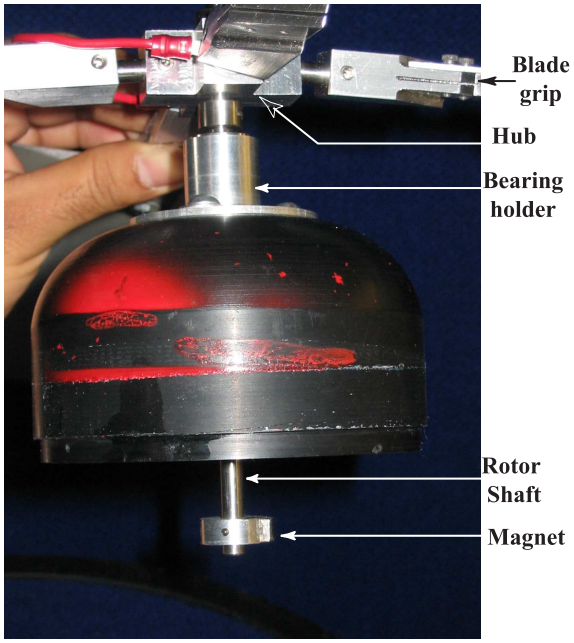

Figure 5.13: Close-up view of the placement of the magnet used to measure RPM.

The sensor is mounted in the Autobody in such a way that one of the sensing directions is aligned with the longitudinal axis of the Autobody. Therefore, the device can give accurate measurements of vertical acceleration if the Autobody falls vertically, i.e. if the accelerometer vertical axis is aligned with the gravity. The descending velocity can be obtained from the integration of the vertical acceleration, however this process is subject to integration error.

3. A pressure transducer [16] measures the static pressure inside the fuselage through holes drilled on the body. The height can be obtained from these readings and was used to cross-check with acceleration measurements.

The sensors were connected to a micro-recorder, the Tattletale TT8V2 [17], which records the data. The Tattletale weighs 1 oz and its dimensions are 2 in x 3 in x 0.5 in. Its maximum sample rate is 100 kHz, and eight analog channels and up to twenty-five digital input/output channels are available. Its RAM memory can store up to 256 kB of data and its flash memory, where the code is stored, can store 256 kB. Our application requires the use of four analog channels to record the pressure, the accelerations along the two axes and the RPM respectively. Each of

these data is sampled at 10 samples per second and stored on 2 bytes per sample. If the flight is assumed to be 60-second long, the total memory needed is therefore 4.8 kB. The input capture function is used to obtain the data from the Hall switch. A free running counter is initialized at the beginning of the code. At each rising time of the Hall switch output, the value of this timer is stored as seconds and ticks, both as short type data. A tick is a subdivision of a second: $10,000$ ticks make one second. An array of thousand samples is assigned to the storage of seconds and ticks. The memory required to store the data from the digital channel is 4 kB. The total memory space needed for one flight is therefore 8.8 kB.

5.2.4 **Test settings**

The Autobody must have a steady state rate of descent lower than 15 ft/s to ensure a safe landing. To achieve this, the thrust should be maximized. Based on the analysis (see Table 4.5), the optimum values of pitch, pitch-flap coupling angle, blade mass and precone angle could be defined. However, the final tested designs were a compromise between the results of the parametric study and mechanical considerations that are described below.

The different chosen pitch angles are presented in Table 5.3. A less negative pitch would have ensured a higher steady state thrust. However, the time to reach autorotation would have been longer. The flight would have therefore be longer, requiring a higher drop altitude.

The parametric study shows that a more negative δ_3 increases the thrust. However, at angles more negative than $-50°$, the pitch increase is so large that the blade stalls before reaching steady state. Therefore, the pitch-flap coupling angle was chosen to be $-45°$ (accurately re-measured to be $-41°$).

The blade mass was lowered as much as the manufacturing and the required rotor diameter allow. However, the blade should be stiff enough to preserve its own mechanical integrity. Three different blades foam cores of varying density and different skin were constructed yielding blade masses of 84.6g, 61.3g and 70.2g respectively.

Finally, the precone angle was selected to be $-4°$. A highly negative precone would have

Table 5.3: Flight tests matrix

Test number	1	2	3
Pitch angle (deg)	-10	-9	-10
δ_3 angle (deg)	-41	-41	-41
Precone angle, β_p (deg)	-4	-4	-4
Blade mass (kg)	0.0846	0.0613	0.0854
Flapping stiffness, k_β (Nm/rad)	313	313	94

resulted in large bending moments on the blade root and could have led to blade structural damage. In addition, a large precone would decrease the effective radius of the rotor disk.

Three different designs were tested to determine which one achieved a rate of descent lower than 15 ft/s. The full scale configurations were tested from a hot air balloon, released from an altitude of 1000 ft, 800 ft and 820 ft respectively. The parameters of the three tested configurations are shown in Table 5.3. The first flight was performed using the high-density foam covered with fiber glass, the low-density foam wrapped in fiber glass was flown during the second test and finally the low-density foam covered with carbon fiber was used during the third test. The on-board instrumentation described previously records RPM, acceleration along the vertical and horizontal axes, as well as the pressure.

5.2.5 Flight test results

First flight test

The first full scale flight test was performed with a rigid hub (see Appendix A.4). Figures 5.14-5.16 show the time history of the following data collected during the first test :

1. The vertical acceleration measured by the accelerometer.
2. The RPM obtained from the Hall switch.
3. The height given by the pressure transducer.

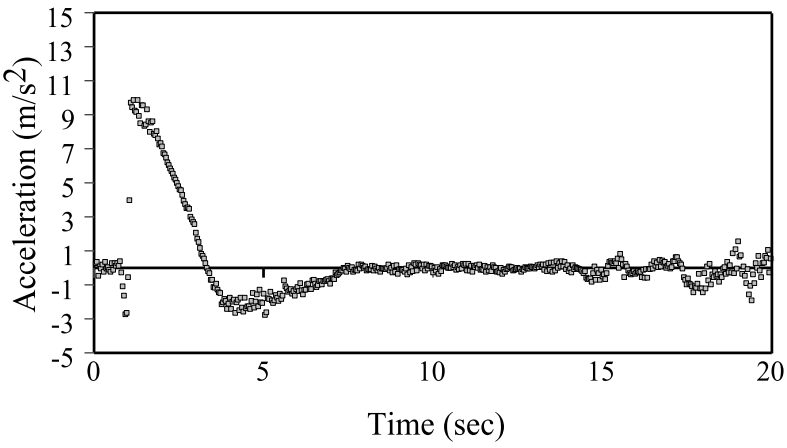

Figure 5.14: Vertical acceleration of the system given by the accelerometer during the first flight test.

It was noted that the rotor started rotating in the appropriate direction. As the rotor RPM increased, the rate of descent was arrested by the thrust generated by the rotor.

Figures 5.14 and 5.16 reveal the presence of both transient and steady state response. The Autobody was held in the balloon for 0.8 second and then released. During this time, the Autobody was stationary, and its vertical acceleration was zero (Figure 5.14), its height is constant and equal to the reference altitude of 1000 ft (Figure 5.16). From Figure 5.14, it can be seen that at the instant of release, the Autobody experiences an acceleration of 1 g, the acceleration of gravity. At this time, the system is in free fall, its vertical acceleration is 9.81 m/s^2. Thereafter, the vehicle starts producing an increasing amount of thrust. This results in a deceleration of the system.

From 2.5 seconds to 6.5 seconds from the release, the vertical acceleration becomes negative because the thrust produced by the rotor is greater than the weight of the vehicle. After approximately 6.7 seconds from the release, the vehicle stabilizes and enters the steady state of autorotation, characterized by zero vertical acceleration.

It was observed that after approximately 15 seconds, the Autobody started precessing. This can be seen as an oscillation in the vertical accelerations values (Figure. 5.14). Thereafter, the angle between the fuselage axis and the vertical kept increasing until the vehicle hit the ground. As a result of the deviation of the fuselage axis from the vertical, acceleration data recorded after

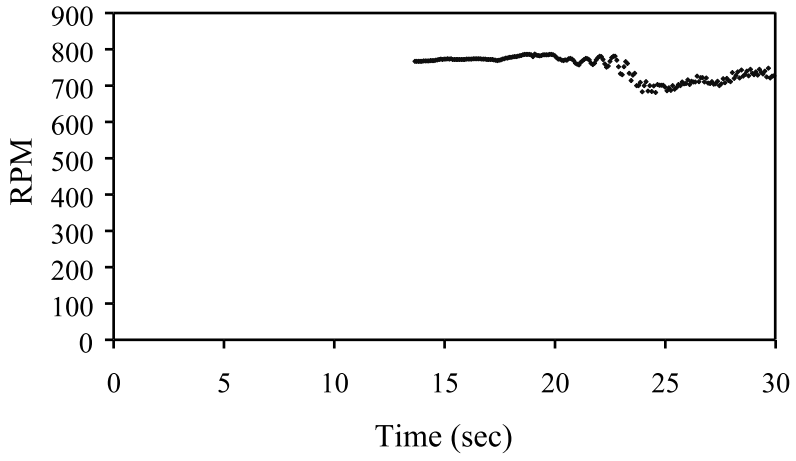

Figure 5.15: Rotor RPM time history given by the Hall switch during the first flight test.

the time the precession started was ignored. Because of the precession, the thrust decreased and the rate of descent increased. Therefore, the precession of the vehicle posed a significant challenge to the measurement of data as well as to the safe landing of the vehicle. The causes of precession will be discussed in a subsequent section.

Figure 5.15 shows the steady state rotor RPM. Because of a data capture error, the RPM data could not be acquired during the transient state of the first drop test. However, the steady state value of rotor rotational speed $\Omega = 772$ RPM is known precisely from the data. The precession can also be seen in the rotor RPM data as variations from the steady state value were observed after about 15 seconds.

Figure 5.16 shows the altitude time history during the first flight. The different phases experienced by the vehicle during the descent can clearly be seen on closer examination of the altitude time history.

- Phase 1: Because of the initial high acceleration of the body, the loss of altitude in this phase is much higher than in steady state.

- Phase 2: The vehicle enters the steady state of autorotation. Its height is a linear function of time as its vertical acceleration is zero (Figure. 5.14).

- Phase 3: From approximately 15 seconds till the end of the flight (height equals to zero), the

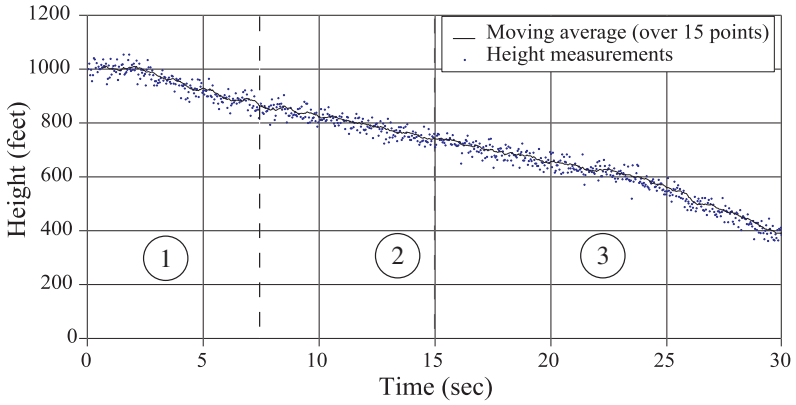

Figure 5.16: Phases in the height time history given by the pressure transducer during the first flight test.

system precessed. Therefore a lower amount of thrust was produced by the rotor. The rate of descent was thus higher and the Autobody lost altitude faster.

Descending velocity calculation

The descending velocity can be obtained either from integrating the vertical acceleration or from the slope of the height measurements from the pressure transducer. The descending velocity V_d is obtained by integration of the acceleration as follows:

$$V_{d,t+\Delta t} = a_t \Delta t + V_{d,t} \tag{5.2}$$

where Δt is the time interval between samples, $V_{d,t}$ the descending velocity at the time t, $V_{d,t+\Delta t}$ the descending velocity at the time $t + \Delta t$ and a_t is the acceleration at time t. This method is prone to errors because of the following reasons:

1. Because the sampling frequency is only $10Hz$, the drift in numerical integration is significant, i.e. Δt is too large to capture rapid variation of acceleration.

2. The precession increases the error after 15 sec of flight. Because of the precession, the accelerometer measured only a component of the effective vertical acceleration of the Autobody, i.e. a_t does not reflect the effective value of the vertical acceleration .

Therefore, the integration of the vertical acceleration data is not a reliable way to calculate the descending velocity. In order to obtain a more accurate descending velocity V_d, the height measurements are used to calculate V_d. However, the height obtained from the pressure transducer has a significant noise level ($\pm$20 ft). Because of the noise level, it is difficult to obtain the descending velocity by numerical differentiation of the height versus time data. Therefore, the following method was used to obtain the steady state value of V_d:

1. A moving average over fifteen data points (Figure 5.16) was performed to filter out the noise.
2. The time at which autorotation was attained was identified from the vertical acceleration versus time plot.
3. The slope of the height versus time curve was calculated during the steady state autorotation (region 2 in Figure 5.16).

Using this procedure, the steady state descending velocity was found to be 19.02 ft/s during the first flight test.

Precession of the vehicle:

Let us now investigate the precession of the vehicle. The precession can be attributed to three causes:

1. Dissimilar blades: The blades can have aerodynamic or mass dissimilarities. In both cases, the thrust vector is not aligned with the rotor shaft, causing a moment on the rotor disk. This results in gyroscopic precession. As blades were finished by hand, small manufacturing dissimilarities may have appeared between each blade which may lead to aerodynamic or mass imbalance. However, the mass dissimilarity was negligible as all blades were mass balanced to within 0.5% before flight.
2. C.G. position: An offset between the vehicle C.G. and the axis of the rotor shaft creates a rolling moment on the rotor disk. This rolling moment combined with the rotor rotation results in a gyroscopic precession.

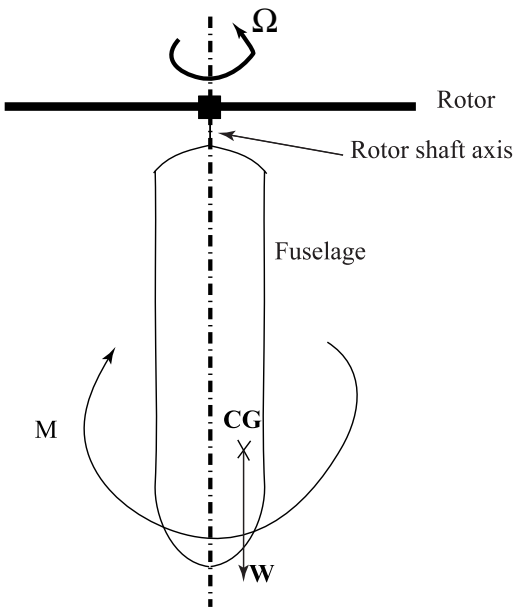

Figure 5.17: Without a gimbal , a misalignment of the CG position with the shaft axis leads to an unstable system.

3. Dissimilar flapping stiffness k_β of the δ_3 hinge: This could occur because of unequal clamping torque on the spring steel constituting the flexure hinge as well as small differences in spring steel thickness. Each blade would thus flap in a different fashion, leading to different amount of lift produced by each blade.

The precession caused by a C.G offset position is depicted schematically in Figure. 5.17. The offset of the C.G. from the axis of rotation creates a moment on the rotor, because it is rigidly attached to the fuselage. This results in gyroscopic precession of the rotor, which is transmitted to the fuselage. Consequently, the offset between the C.G. and the rotor shaft is increased, which further increases the instability.

In order to suppress this instability, a gimbal was integrated between the fuselage and the rotor. As shown in Figure 5.18, the gimbal permits the alignment of the thrust T and weight W vectors without transferring any moment to the spinning rotor. As the fuselage is free to tilt without affecting the rotor plane, i.e. the thrust direction, the C.G. can align itself along the rotor shaft axis.

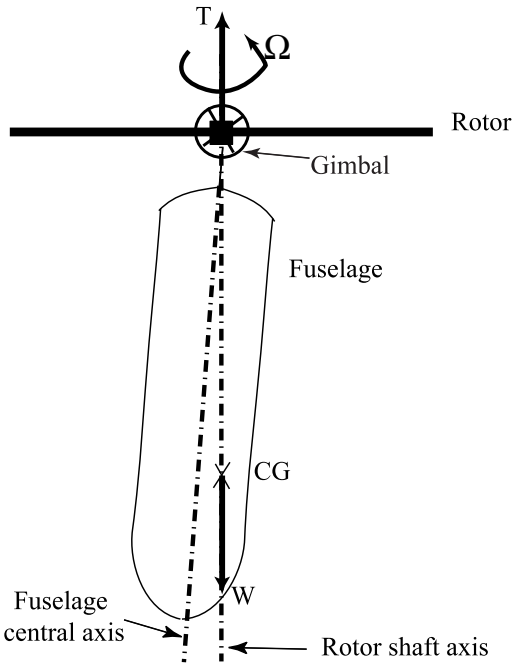

Figure 5.18: The gimbal permits the alignment of the weight and the thrust with the gravity.

Second and third flight tests

The vehicle configuration incorporating the gimbal was tested during the second and third drops (see technical drawings of the gimballed hub in Appendix A.5). Figure. 5.19 shows the gimbal installed at the rotor hub. The blades were mass balanced to within 0.5%. With the introduction of the gimbal and the careful balance of the blades, the only source of precession is dissimilarity between the flapping stiffness of each δ_3 hinge.

During the second flight, the vehicle began precessing after about 12 seconds in spite of the gimbal. During the third test, the vehicle was stable for the first 22 seconds. The cause of the precession was attributed to the dissimilar flapping stiffness of the δ_3 hinges. Because of the instability, the vertical acceleration data from the second flight test after 12 seconds and from the third flight test after 22 seconds were ignored.

The vertical acceleration, height and RPM data from the three instrumented flight tests are compared in Figures 5.20- 5.22.

Figure 5.20 presents the vertical accelerations obtained from the three tests. It can be

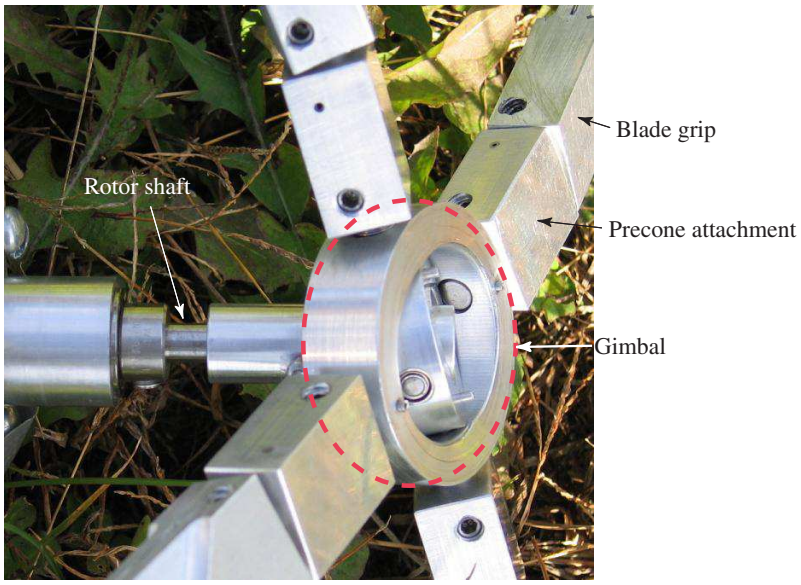

Figure 5.19: Gimballed rotor hub.

seen that all three tests show similar trends. The vertical acceleration first jumps to the value of the acceleration due to gravity and then decreases to zero when steady autorotation is reached. Figure 5.21 shows the altitude time history of the two Autobody configurations, obtained from pressure sensor measurements.

Figure 5.22 shows the RPM of the rotor during tests #1 and #2. RPM data from the third test could not be recorded because of a problem with the on-board data-logger. The transient increase in RPM can clearly be seen in the data from the second configuration. Additionally, the second configuration experiences a lower steady state RPM than the first configuration.

5.2.6 Landing impacts

For all flights, the rotor featured lag hinges about which the blades can pivot. Figure 5.23 shows a picture of the vehicle after it landed during the flight test #1. It can be seen that the rotor is suddenly brought to rest as the blades hit the ground. The lag hinge increases the survivability of the blades by allowing them to rotate about its axis.

For the third flight, the rotor hub was equipped with lag hinges as well as sandpaper attached between the blades and the blade grips near the lag hinge. On impact, the blade swivels about the

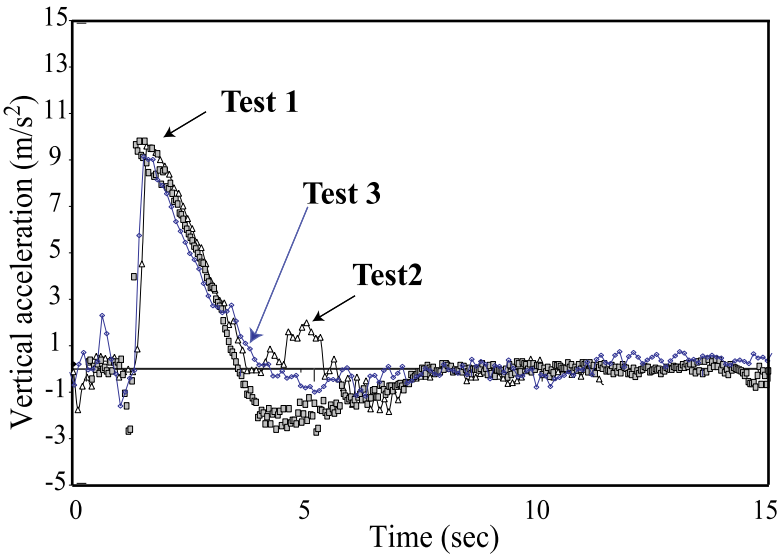

Figure 5.20: Vertical acceleration time history comparison between the three flight tests

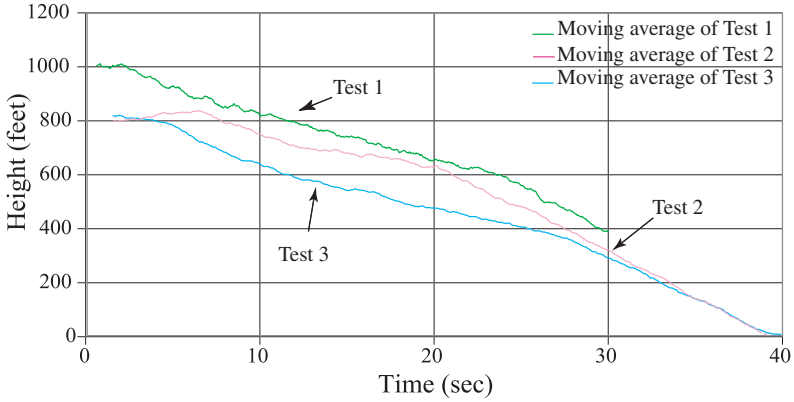

Figure 5.21: Filtered height time history comparison between the three flights.

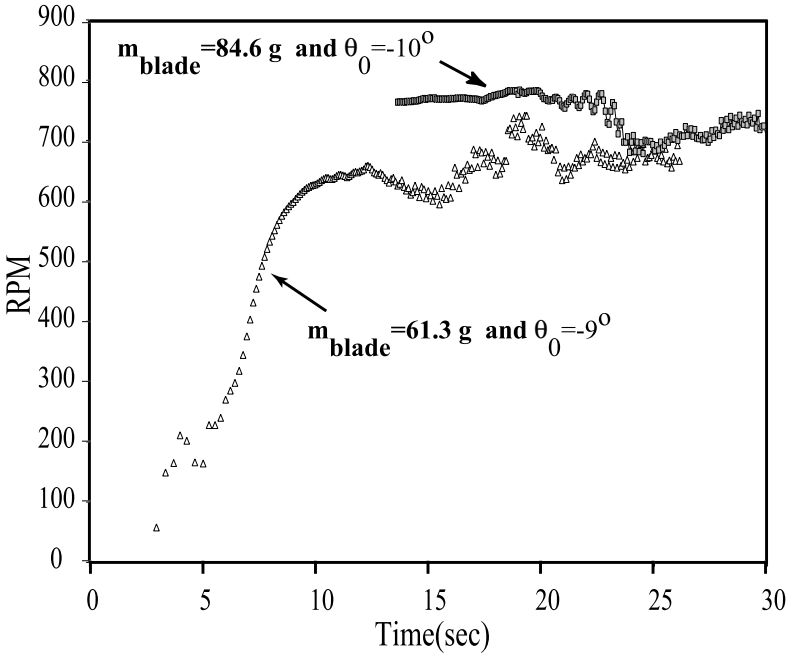

Figure 5.22: RPM time history comparison between the two flights.

Figure 5.23: Lag hinge increases blade survivability on impact.

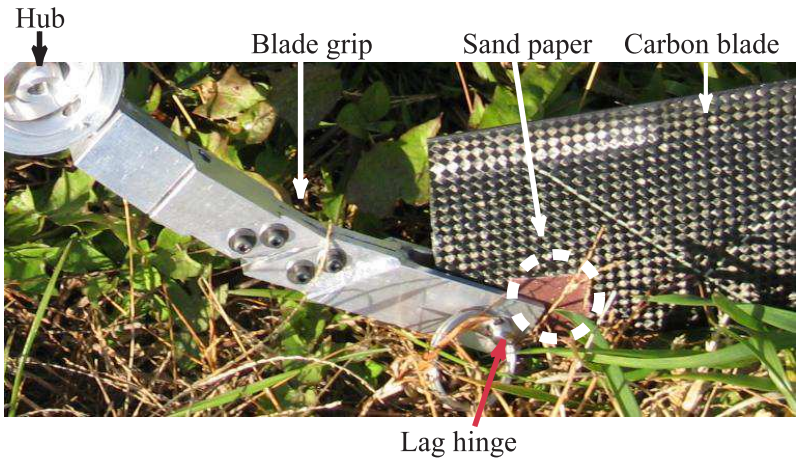

Figure 5.24: Sand paper increases the friction between the blade and the blade grip and increases the blade survivability.

lag hinge, and energy is dissipated by the Coulomb friction of the sandpaper rubbing against the blade grip. As additional energy is dissipated during the impact, the survivability of the blades increases. It was observed that the blades used in the third flight test did not suffer any damage during landing. Figure 5.24 shows a close view of a third generation blade attached to the hub by a lag hinge with sandpaper stuck between the blade and its grip. It was concluded that these two features are important aspects of the overall design.

5.2.7 Correlation with analysis

Analytical results are compared with experimental data obtained during the three flights. Figure 5.25 presents the analytical predictions and experimental data of steady state descending velocity for the three flights.

As seen in Figure 5.25, the analytical and experimental results show good agreement. The maximum error between analysis and experiment is 22.2% and occurs in the third flight test. The third test was performed with the lowest flapping stiffness k_β and it is expected that the dissimilarities between the k_β of the blades had a larger effect. Because the k_β was lower in case #3, the thrust generated was greater and the rate of descent lower than for flight #1 and #2. For all tests, the descending velocity is overestimated by the theory. This is because the analysis

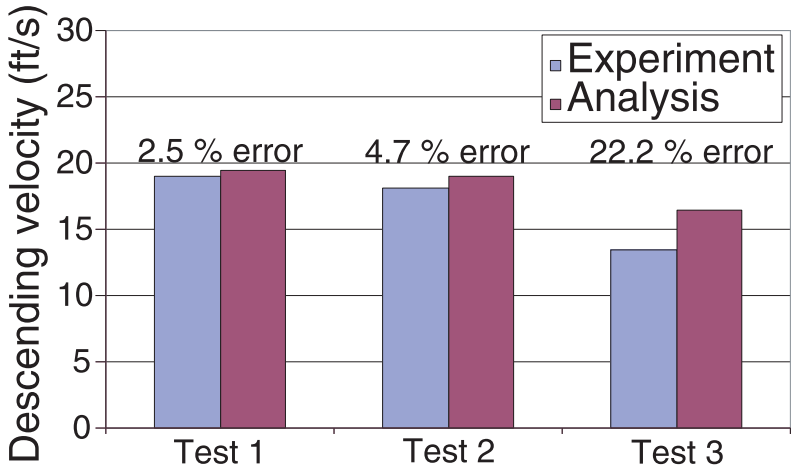

Figure 5.25: Steady state descending velocity correlation.

underestimates the thrust, as noticed during correlation of analysis with wind tunnel tests (see Chapter 4, Section 4.8). The measured descending velocity for the third test is 13.5 ft/s. Therefore, this Autobody design meets the requirement of a descending velocity lower than 15 ft/s.

Figure 5.26 shows the theoretical predictions and experimental data of steady state rotational velocity for the three flight tests. The analytical and experimental results of rotational velocity show good agreement as seen in Figure 5.26. The analysis underpredicts the rotational velocity, as noticed during correlation of analysis with wind tunnel tests (see Chapter 4, Section 4.8). The RPM error between analytical predictions and experimental data is less than 15%. Threfore, the analysis can predict accurately the rotor RPM in steady state.

From these results, it can be concluded that the flight test data and analytical predictions show good agreement. Therefore, the steady state behavior of the Autobody can be predicted accurately by the analysis. Finally, the steady state rate of descent being less than 15 ft/s during the third flight, reveals that this Autobody is a successful design.

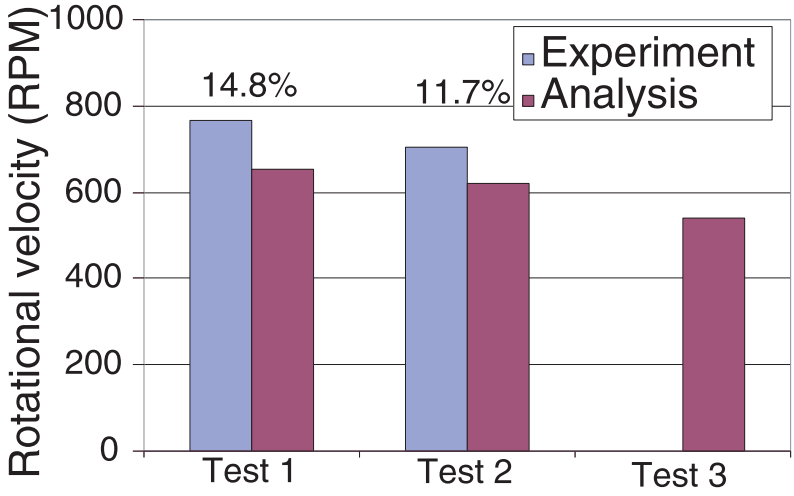

Figure 5.26: Steady state rotor rotational velocity correlation.

Chapter 6

Conclusions and Future work

6.1 Summary and conclusions

Analytical and experimental studies have been carried out to investigate the behavior of an autonomous vehicle with passive controls, called the Autobody. It is designed to deploy a payload on ground from an aircraft by means of an autorotative rotor. The design requirements were defined as:

1. A 5 lbs-gross weight.
2. A passively controlled 4-bladed rotor of 4 ft diameter.
3. A maximum steady state descending velocity of 15 ft/s.

A negative blade pitch was introduced to start the rotor rotation is the correct direction (i.e. leading edge first). A novel mechanism consisting of a negative pitch-flap coupling in conjunction with a negative precone was proposed to passively increase the pitch of the rotor blades as the rotational speed increased. The negative pitch-flap coupling incorporated in the rotor design generated an increase in pitch in response to an increase in flap angle. A negative precone was included to produce increased flap deflections. These concepts ensure that the rotor rotation was initiated in the correct rotation and that enough steady state thrust was generated to minimize the descending velocity of the system and ensure its safe landing.

Two analytical studies were proposed to predict the behavior of the Autobody in steady state of autorotation. First, a Time Marching Method was developed based on momentum theory. This method involved a rotor starting from rest. The rotor aerodynamic characteristics were computed at each time step until the net rotor torque equals zero. At this final time step, the steady state of autorotation had been reached. This method showed one major drawback. During the transient state described by this analysis, portions of the blades may go into Vortex Ring State (VRS). At

those spanwise locations, the rotor aerodynamic quantities were computed based on an empirical model whereas momentum theory was used to calculated the same quantities at the blade segments not operating in VRS. It was observed that because of the discontinuity between the experimental model and the analytical solution at a climb velocity ratio of $\frac{V_c}{v_h} = -2$, a numerical oscillation could occur, rendering the convergence very difficult. Therefore, it was determined that the Time Marching Model could not predict accurately the behavior of the system in these conditions. To address this issue, another analytical model, the RPM Sweep Method, was developed. This analysis was based on blade element momentum theory (B.E.M.T.). As the flow through the rotor is not clearly defined in Vortex Ring State, this method did not attempt to calculate the inflow in this operating state. For a given RPM, the model calculates the rotor thrust T and torque Q from B.E.M.T. The process was repeated for a range of chosen RPM in the Windmill Brake State. However, calculation was stopped if $\frac{V_c}{v_h} \geq -2$, beyond which momentum theory is not valid. The calculated rotor torque coefficients were plotted versus RPM. An extrapolation of this curve was performed to find the zero torque point which corresponded to steady state autorotation. At this RPM, the thrust and torque were calculated.

Wind tunnel tests were performed on a model scale rotor to :

1. Establish the proof-of-concept of the rotor design.

2. Investigate the influence of the rotor design parameters on the steady state performance of the rotor.

3. Validate the analysis.

The thrust and RPM were measured for several values of airstream velocities V_d, blade pitch, pitch-flap coupling and precone angles. The analysis was run for the range of descending velocity considered. It was observed that both the experimental and analytical thrust versus V_d curves were quadratic and that the RPM versus V_d curves were linear. It was observed from the wind tunnel tests results that the thrust and RPM increased for:

1. Less negative blade pitch angle θ_0.

2. More negative pitch-flap coupling angle δ_3.

3. More negative precone angle β_p.

Furthermore, it was observed that the experimental data and analytical predictions show good agreement with a maximum error in the range 10 to 15%.

A parametric study was carried out to investigate the influence of different parameters on the steady state thrust and RPM. The different parameters studied are the :

1. Blade pitch, θ_0.

2. Pitch-flap coupling angle, δ_3.

3. Precone angle, β_p.

4. Blade mass m_b.

A baseline case was considered and compared to other cases with one parameter only being varied at a time. The same trends as the wind tunnel tests trends were observed. In addition, the thrust and RPM were found to decrease with heavier blades. It was noted that the quantitative influence of each parameter on the steady state thrust and RPM is different. For a 100% change in each parameter from the baseline values, the parameters which had the greatest influence on thrust and RPM were the δ_3 angle and θ_0 angle (30.2% thrust variation and 58.3% RPM variation for 100% change in δ_3 angle and 25% thrust variation and 63% RPM variation for 100% change in θ_0 angle).

Based on the parametric study and mechanical considerations, an optimum full scale configuration was determined to achieve the objective of steady state descending velocity less than 15 ft/s. Instrumented flight tests on this configuration were conducted to obtain rotor RPM, vertical acceleration, descending velocity and altitude of the Autobody during the transient and steady states of autorotation. The Autobody was dropped from a hot air balloon and the data were recorded on an on-board microrecorder. Moreover, it was observed that blade grip design ensured blade survivability during landing impacts so that same blades could be used in future flight tests. Flight tests also indicated the possibility of an instability affecting the vehicle, caused by precession of the rotor disk. It was proposed to alleviate this problem by introducing a gimballed hub.

Testing of the Autobody equipped with the gimballed hub showed it delayed the onset of such instability. It was observed that a steady state rate of descent of 13.5 ft/s was attained for a rotor equipped with:

1. A blade pitch angle $\theta_0 = -10°$.
2. A pitch-flap coupling angle $\delta_3 = -41°$.
3. A precone angle $\beta_p = -4°$.
4. A blade mass $m_b = 85.4$ g

This configuration met all the requirements and is therefore a successful design. Furthermore, the full scale flight test experimental results showed good agreement with the analytical predictions. The maximum error between analysis and experiment was 22.2% for the prediction of the descending velocity during one of the flight tests.

6.2 Future Work

To describe more accurately the behavior of the Autobody during its flight, an analysis of the transient state of the flight should be developed. Rotor aerodynamics and rate of descent would therefore be predicted throughout the flight.

Improvements must also be carried out in the design and manufacturing of the δ_3 hinge. Repeatable and precise manufacturing process of the flexure hinge would ensure that all the hinges have equal flapping stiffness and therefore allow each blade to flap and pitch in a similar fashion. This would assure a balanced rotor and stable flight and avoid precession.

Finally, a more reliable instrumentation should be used to perform further flight tests. Specifically, a higher sampling rate microrecorder should be used and means of measuring height and descending velocity more accurately should be developed.

Appendix A

Technical Drawings

A.1 Model scale rotor assembly

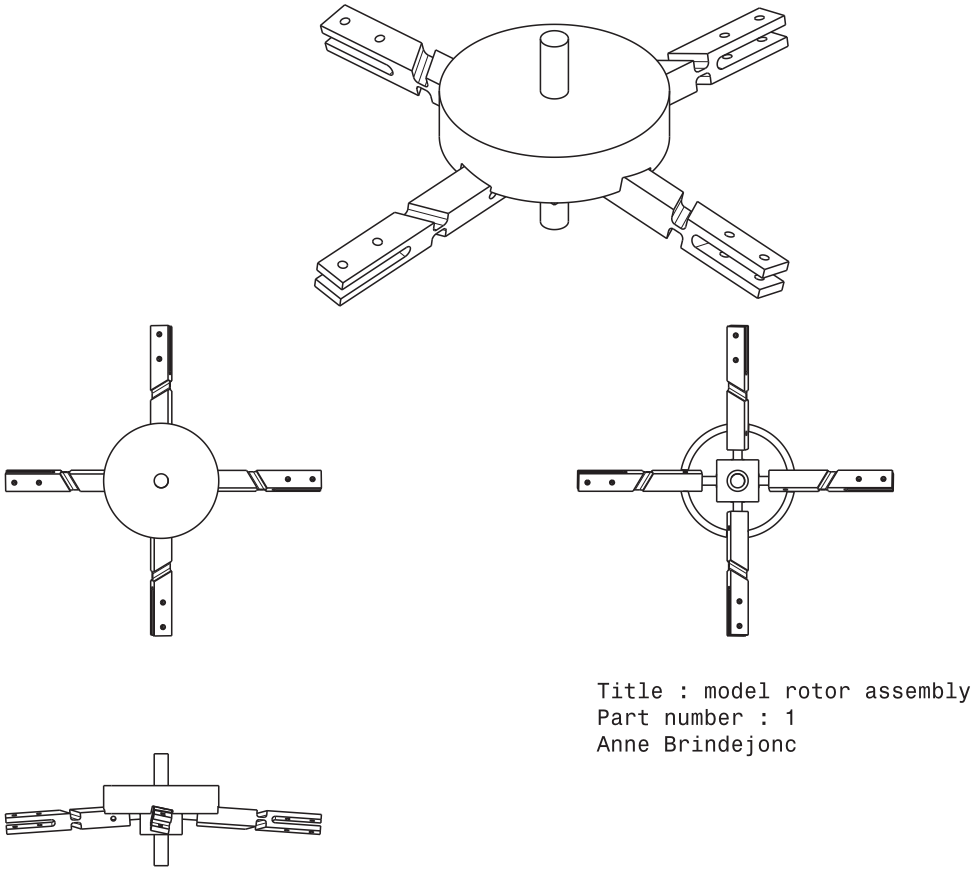

Figure A.1: Model scale rotor assembly

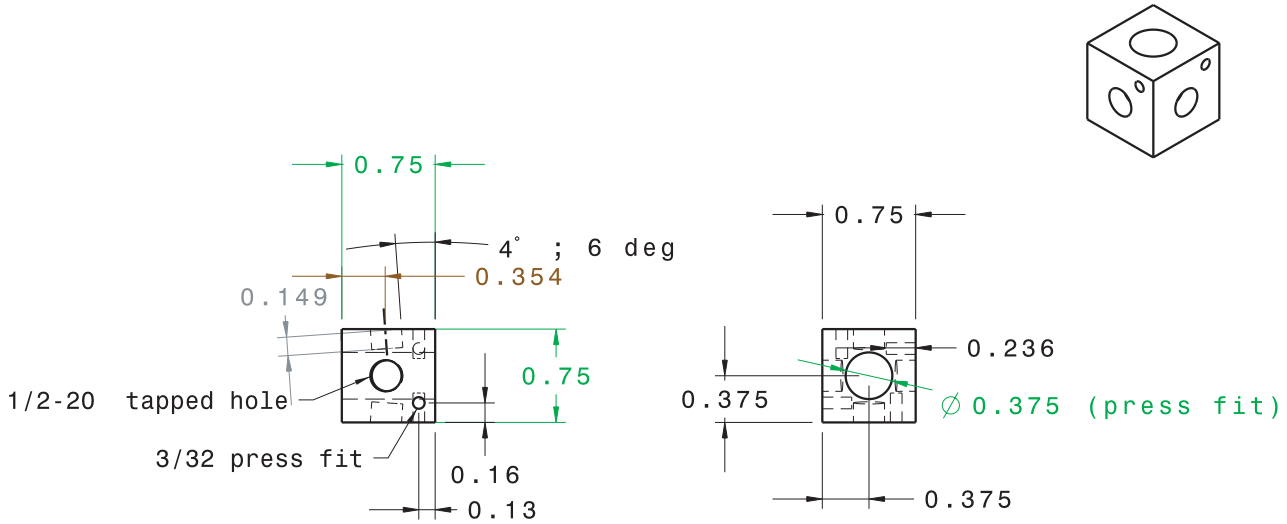

Title: Model Hub
Part number: 1a
1 of each configuration (4 or 6 deg)
Material : aluminum
All dimensions in inches
Scale: 1:1
Anne Brindejonc

Figure A.2: Model scale hub

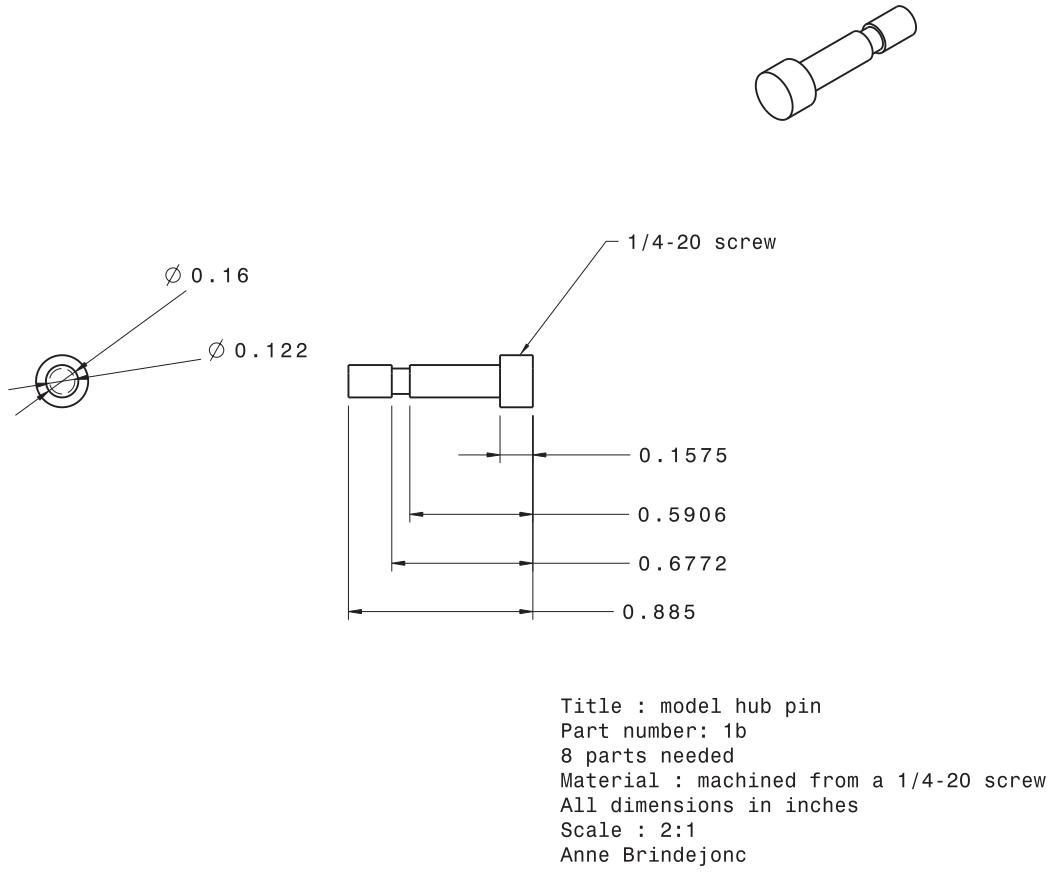

Figure A.3: Pin inserted in the model scale hub. The blade pitch is set by rotating the blade grip around this pin.

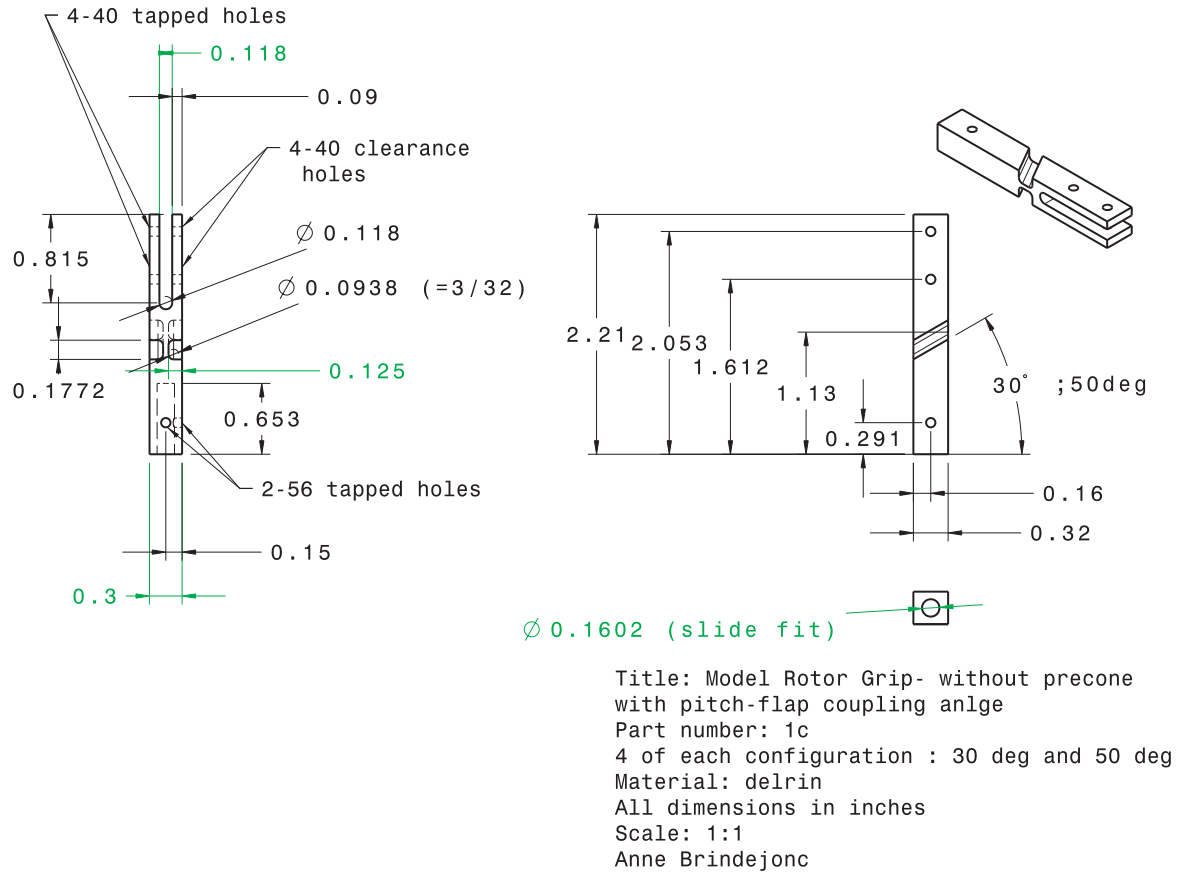

Figure A.4: Blade grip.

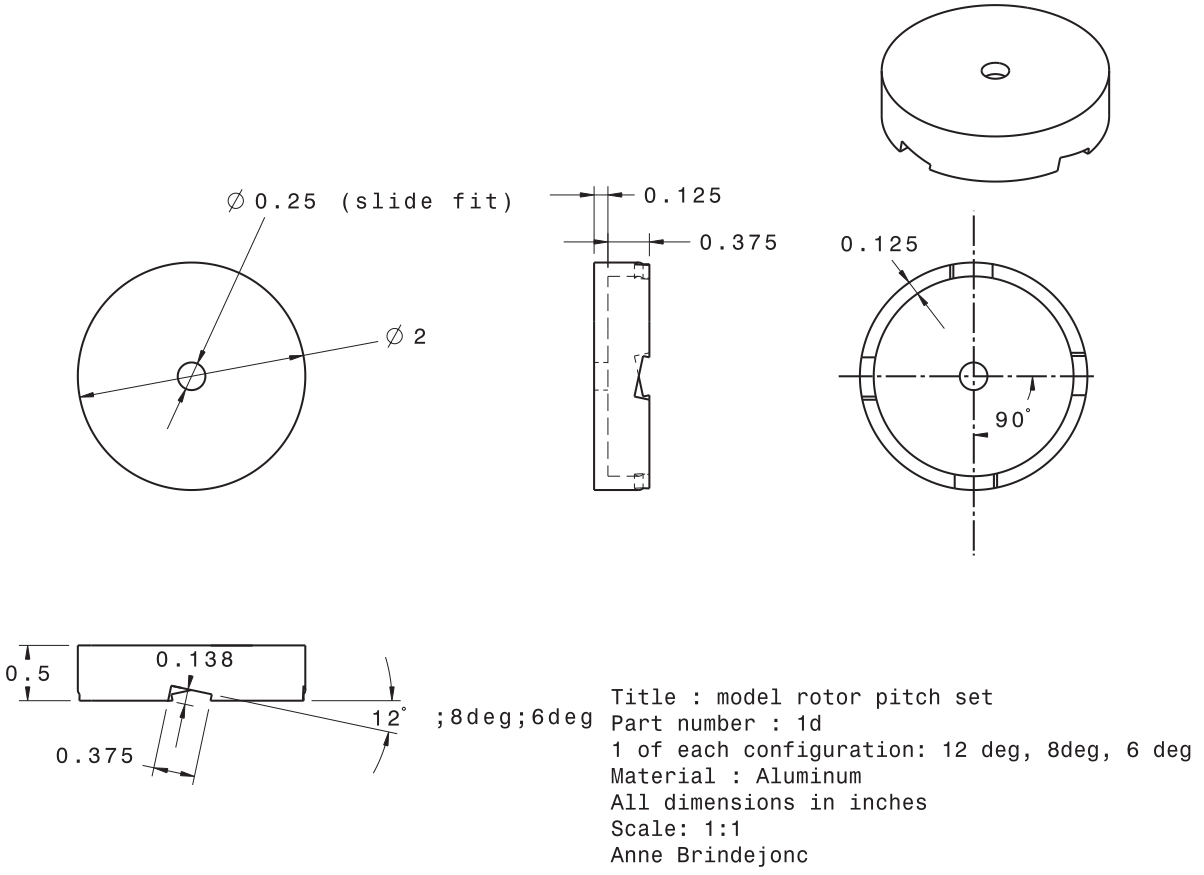

Figure A.5: Pitch setting fixture mounted on the rotor shaft.

A.2 **Rotor stand used in the wind tunnel**

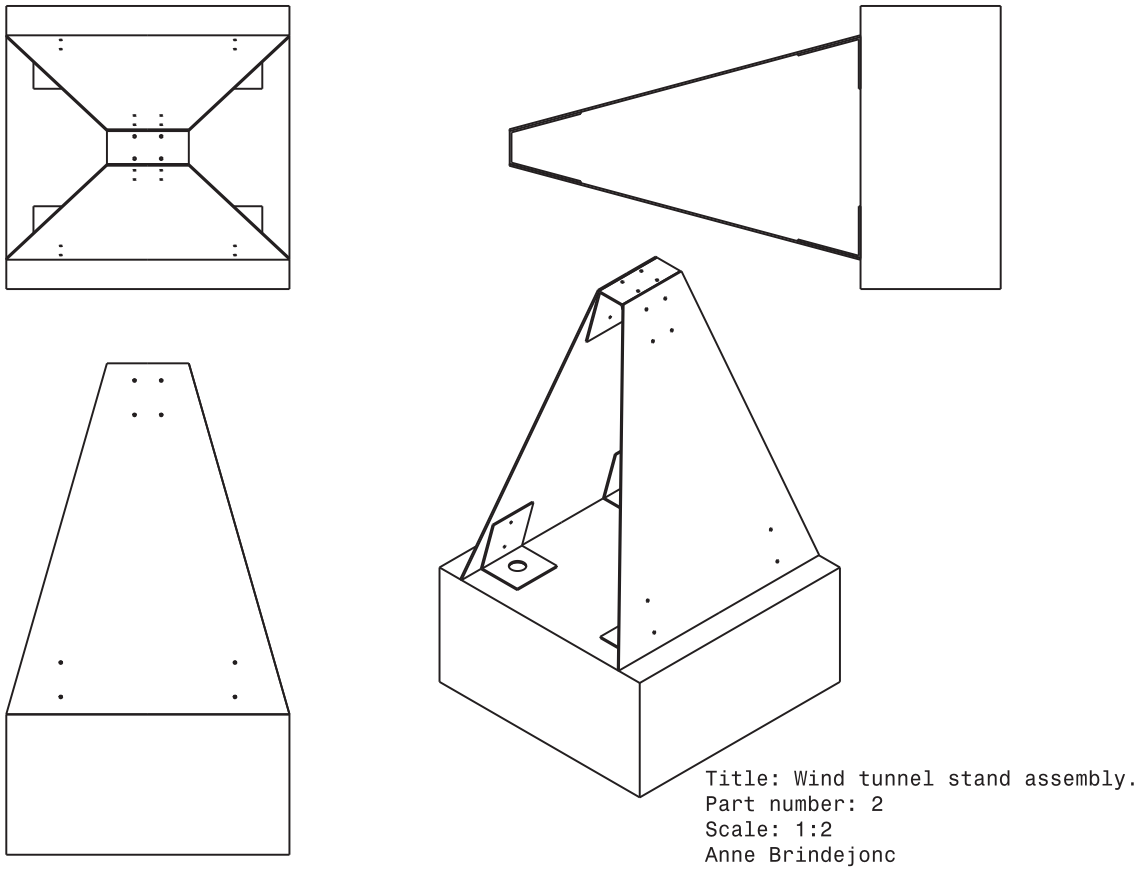

Figure A.6: Rotor stand used during the wind tunnel tests.

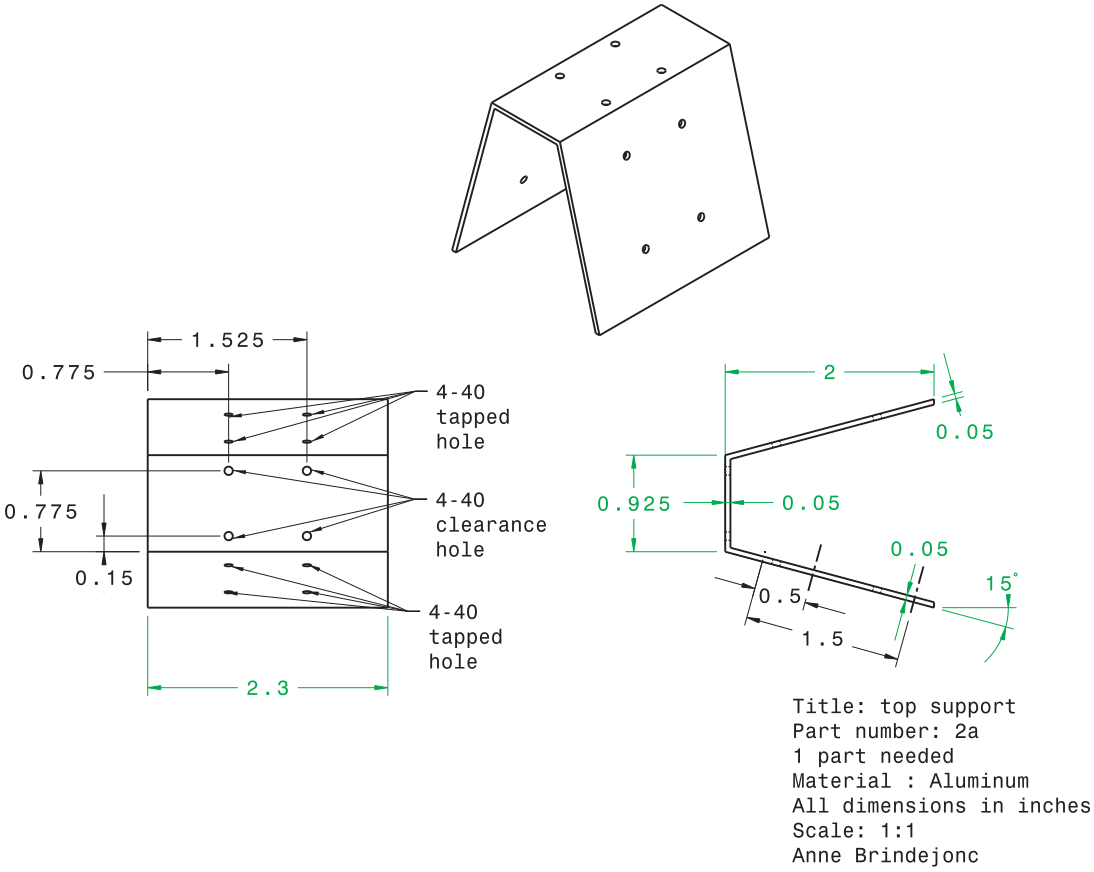

Figure A.7: Top part supporting the side mounts. The balance is attached on the top part.

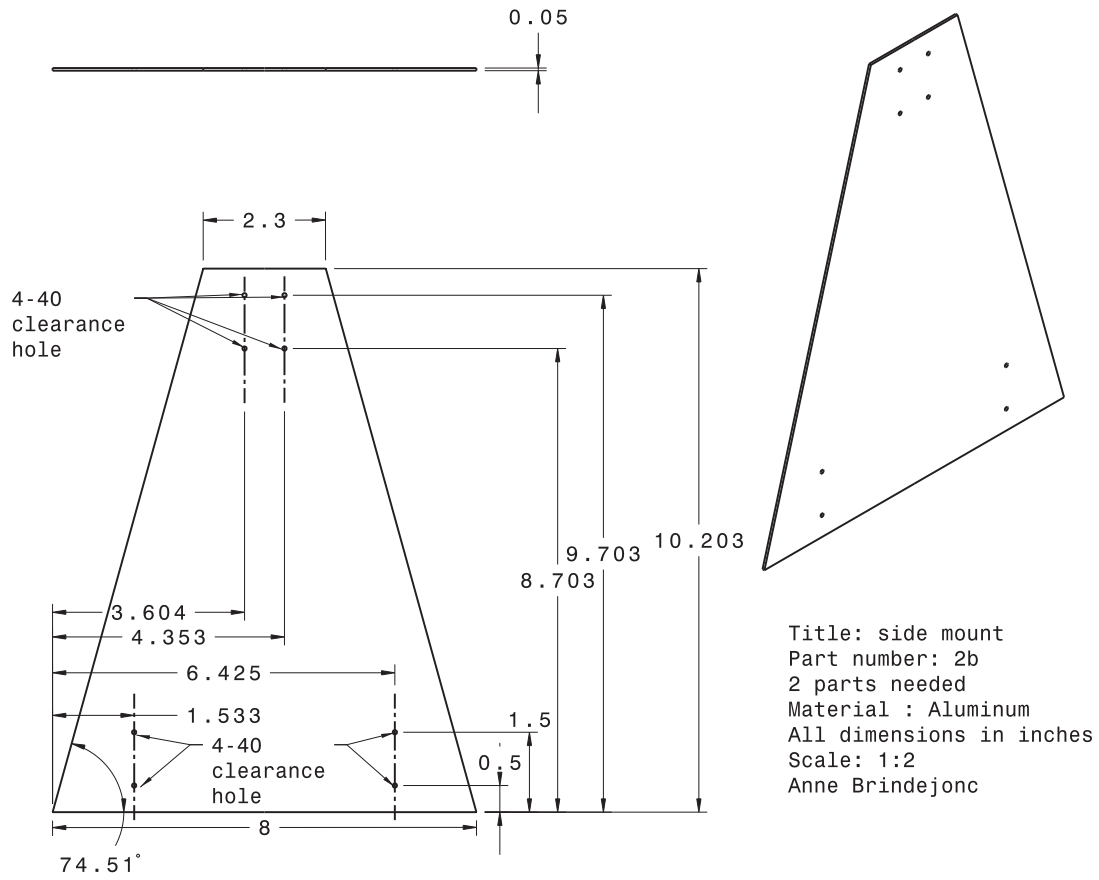

Figure A.8: Side mounts.

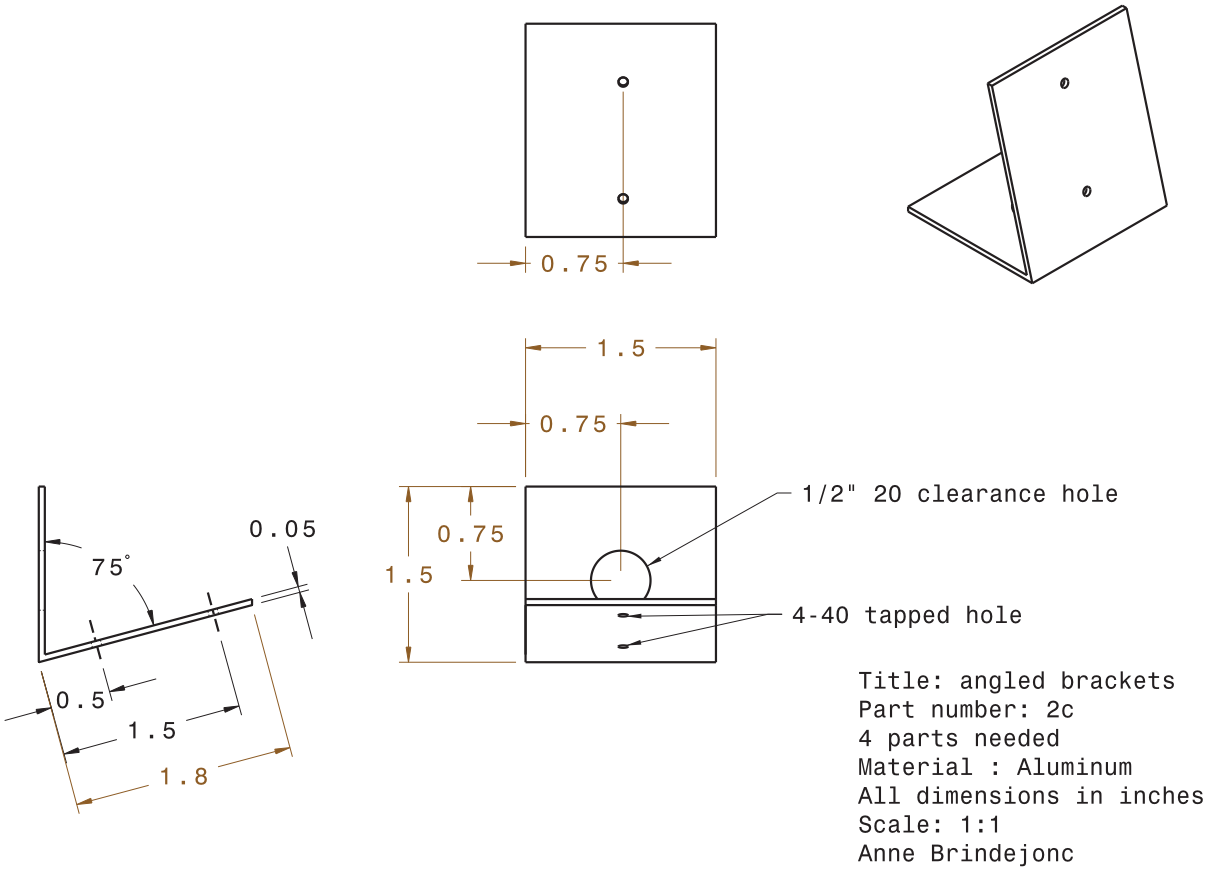

Figure A.9: Angled brackets anchoring the whole assembly.

A.3 **Load balance**

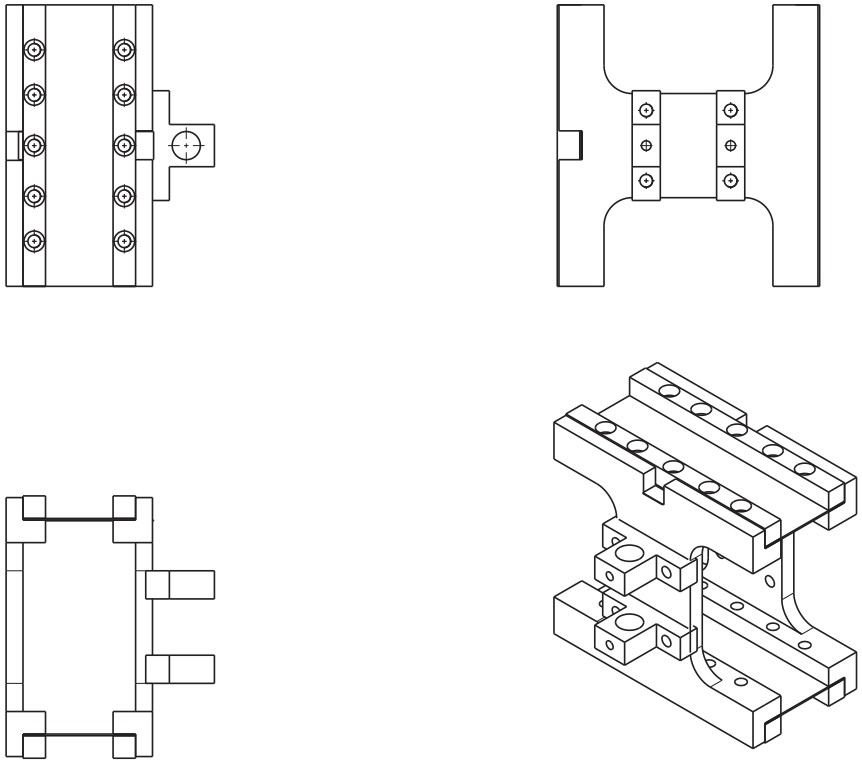

Figure A.10: Load cell balance assembly.

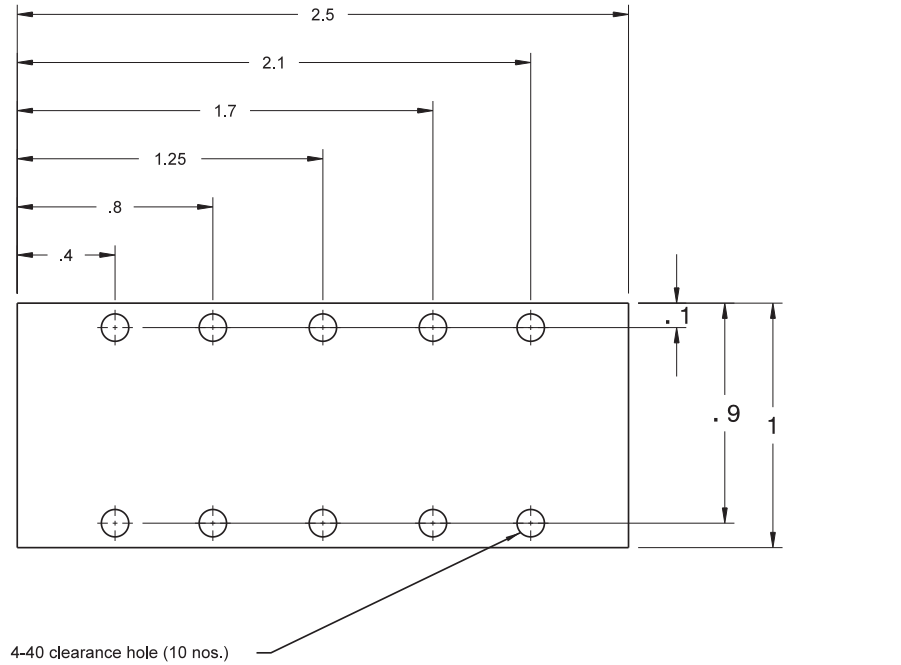

Figure A.11: Brass flexures of the balance on which the load cell is attached.

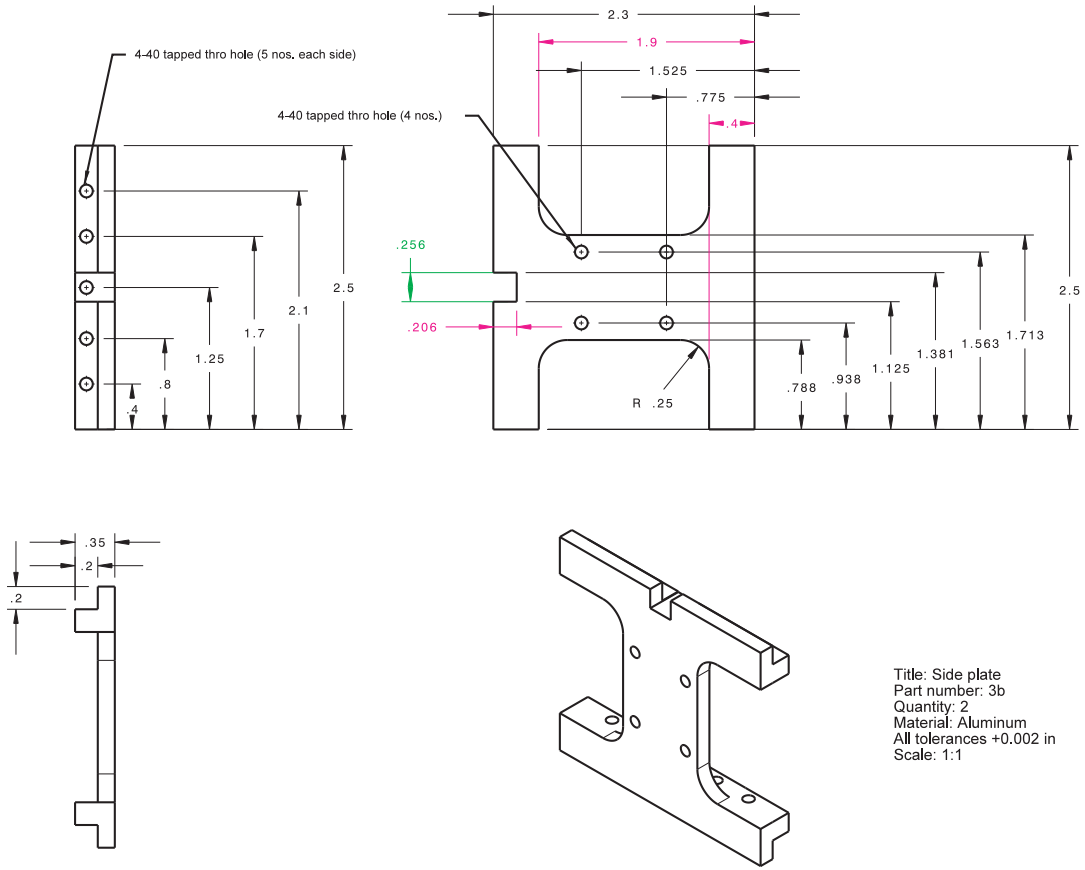

Figure A.12: Side plates of the balance.

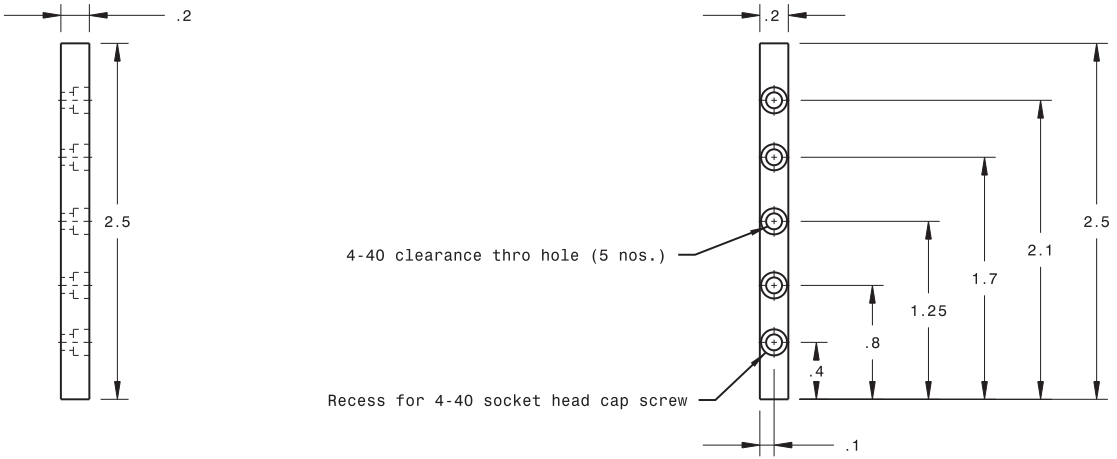

Title: Clamp
Part number: 3c
Quantity: 4
Material: Aluminum
All tolerances +/-0.001 in
Scale: 1:1

Figure A.13: Flexure clamp.

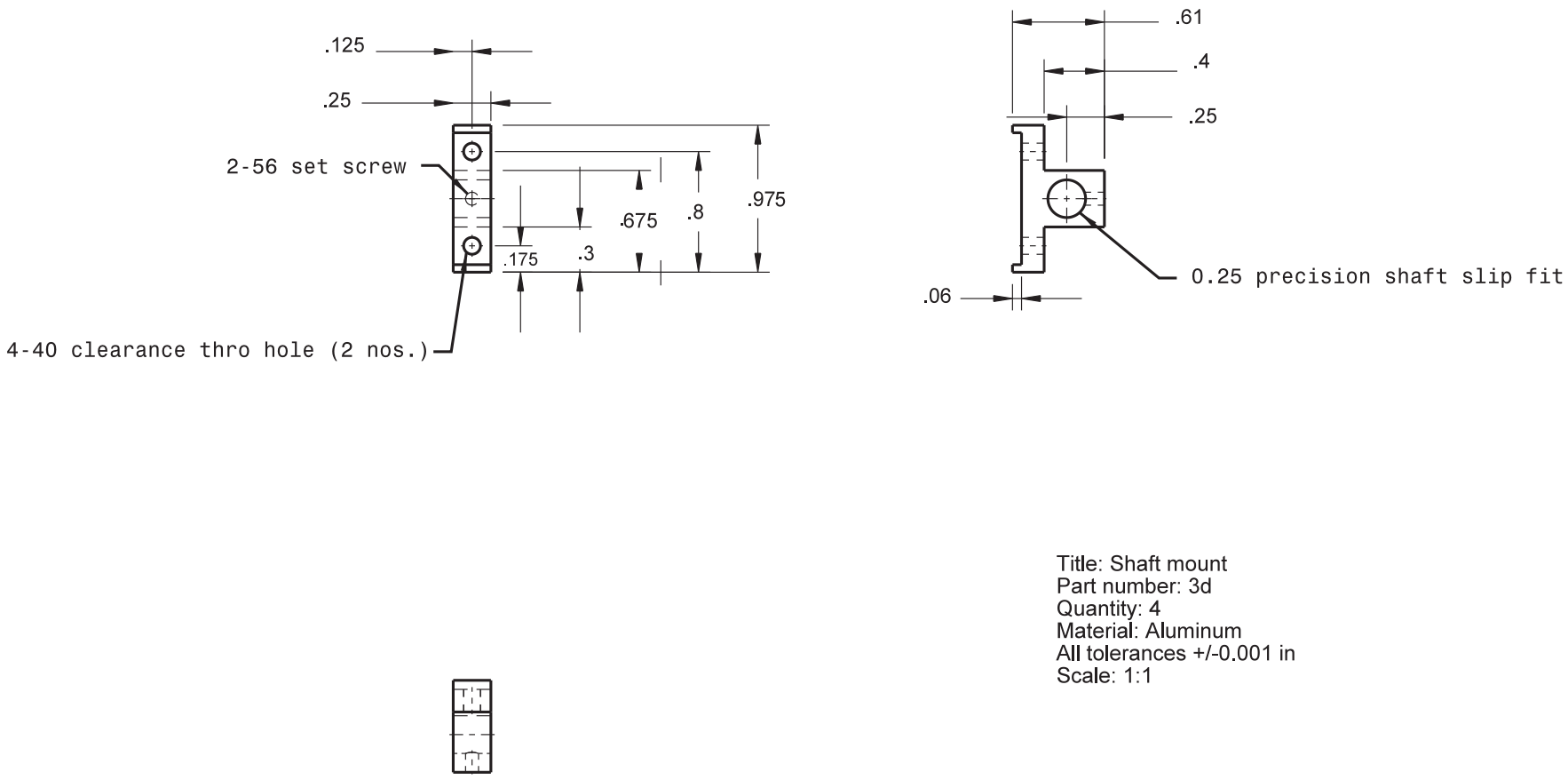

Figure A.14: Shaft mount attached to the balanced.

A.4 **Full scale rigid hub.**

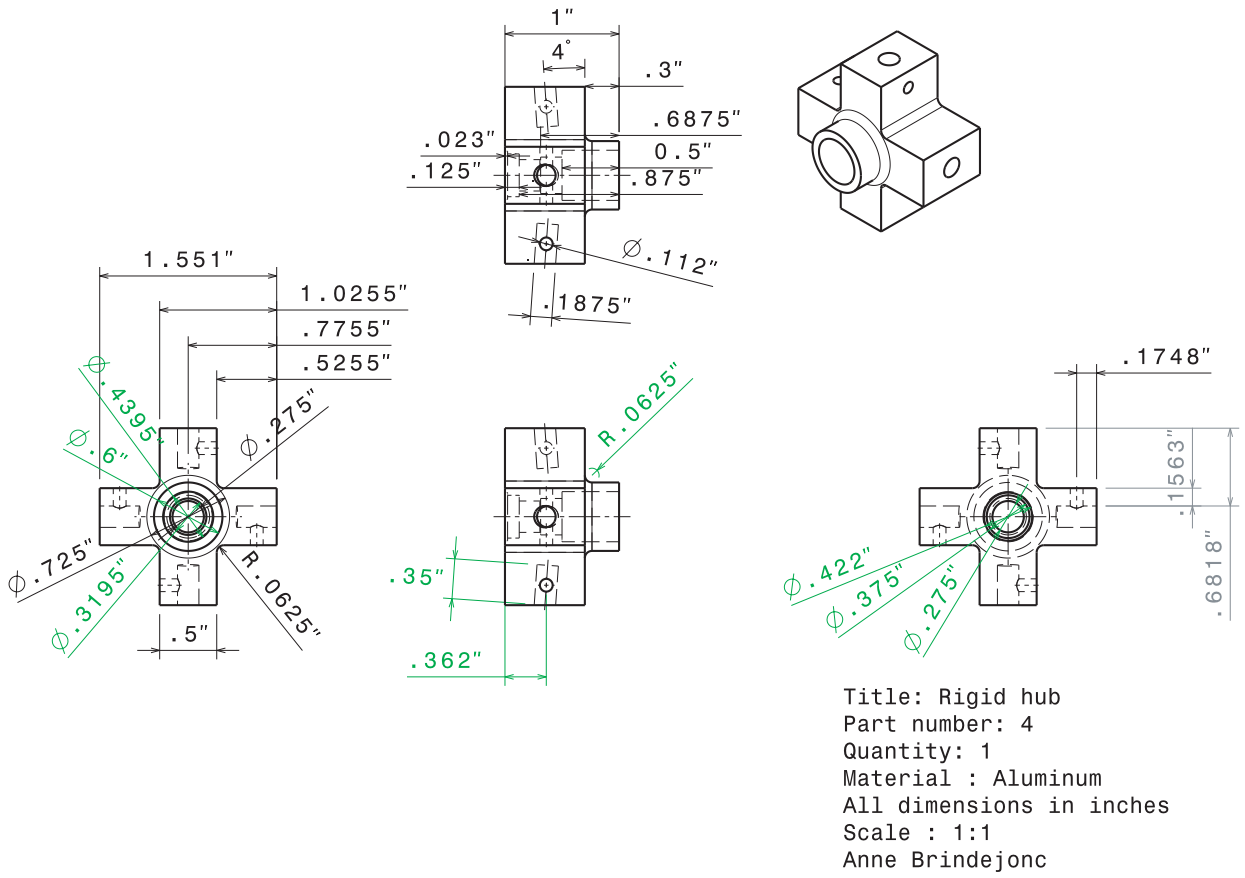

Figure A.15: Full scale rigid hub used in flight test #1.

A.5 **Full scale gimballed hub.**

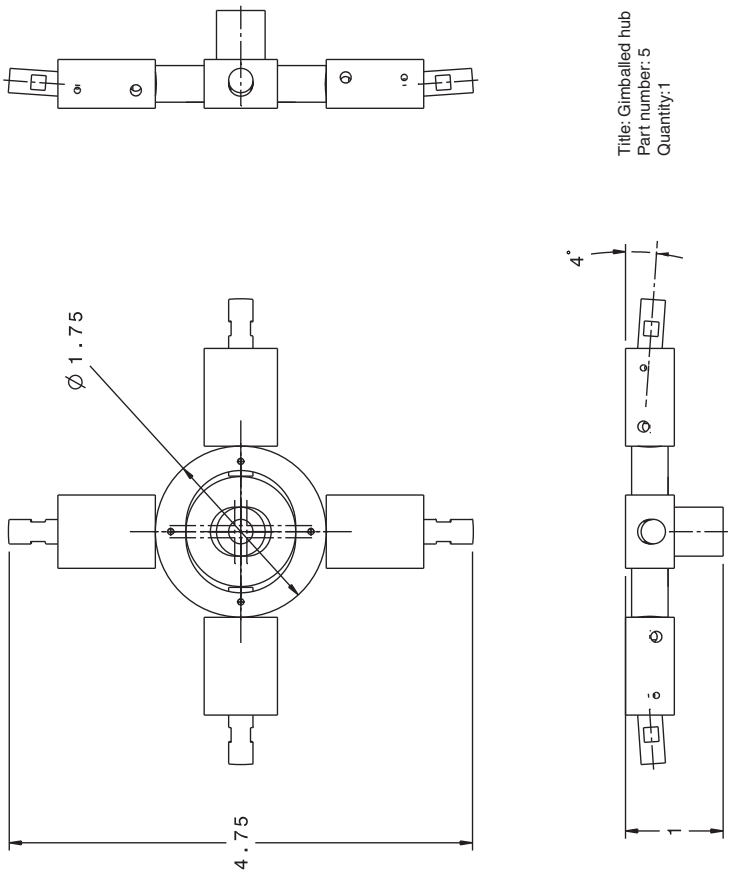

Figure A.16: Full scale gimballed hub used in flight tests #2 and #3.

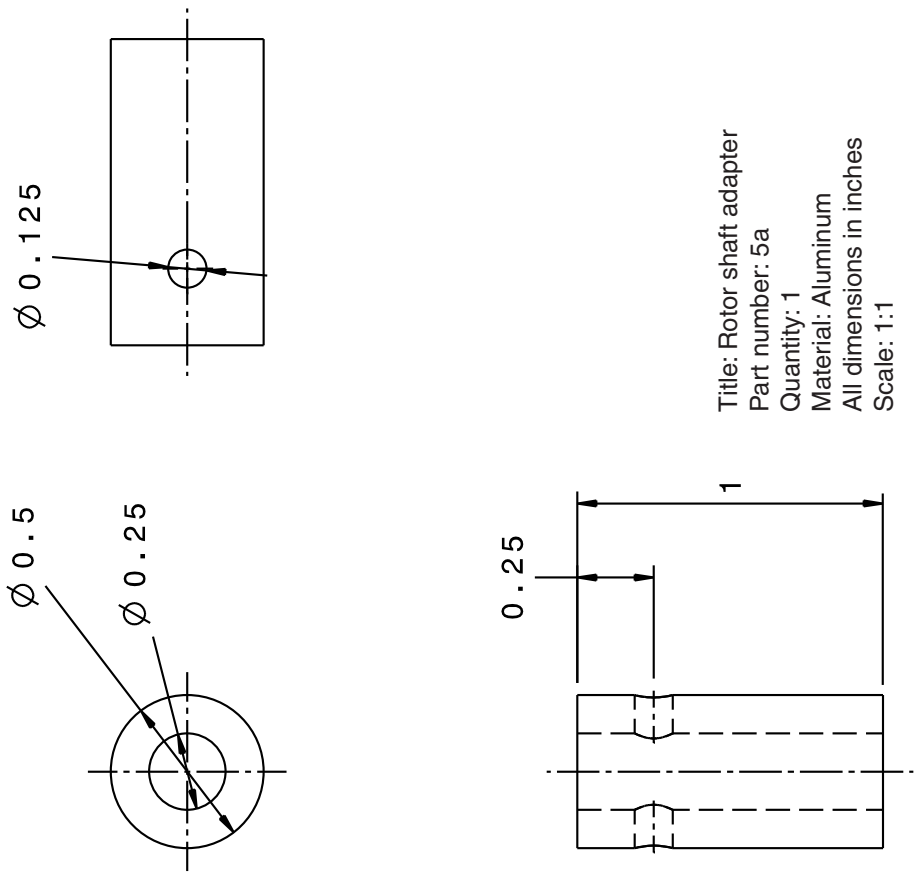

Figure A.17: Shaft adapter.

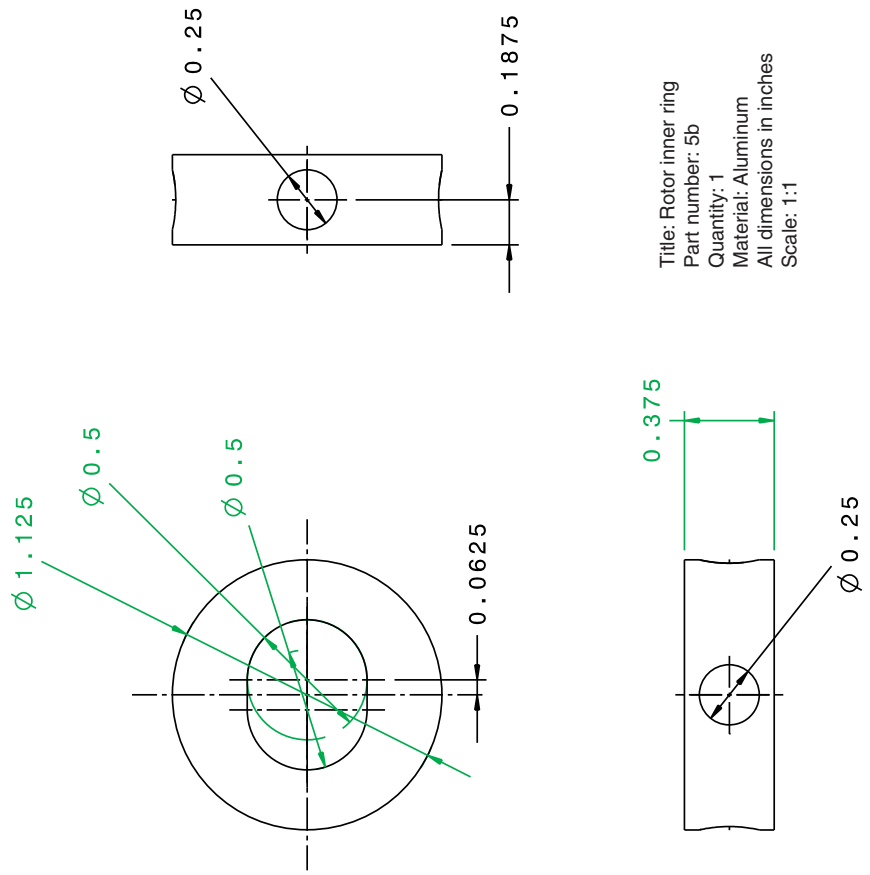

Figure A.18: Inner ring of the gimballed hub.

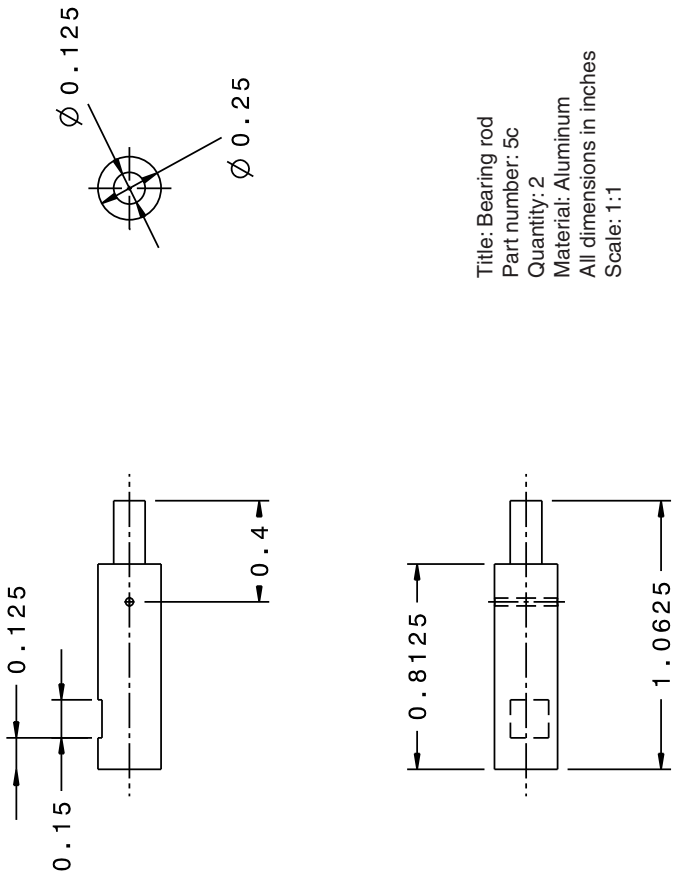

Figure A.19: Bearing rod.

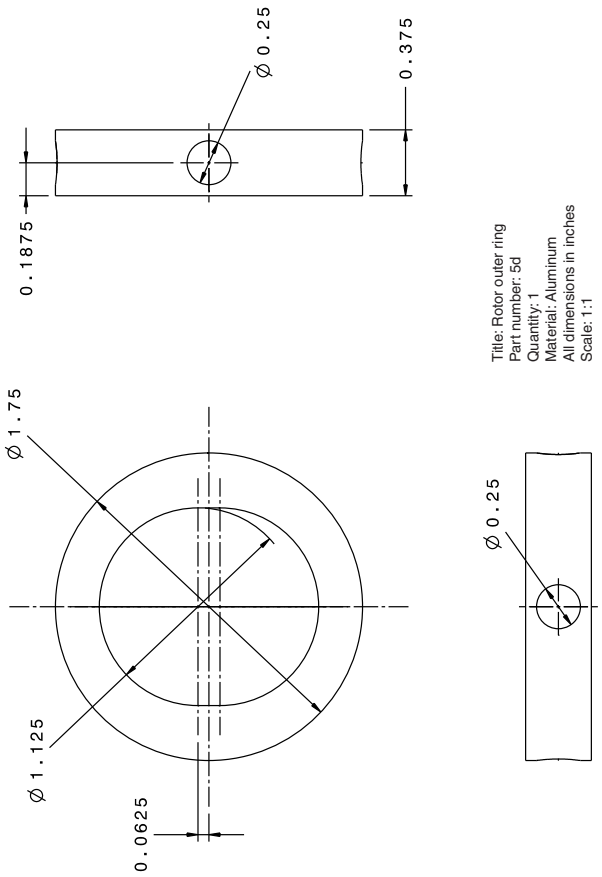

Figure A.20: Outer ring of the gimballed hub.

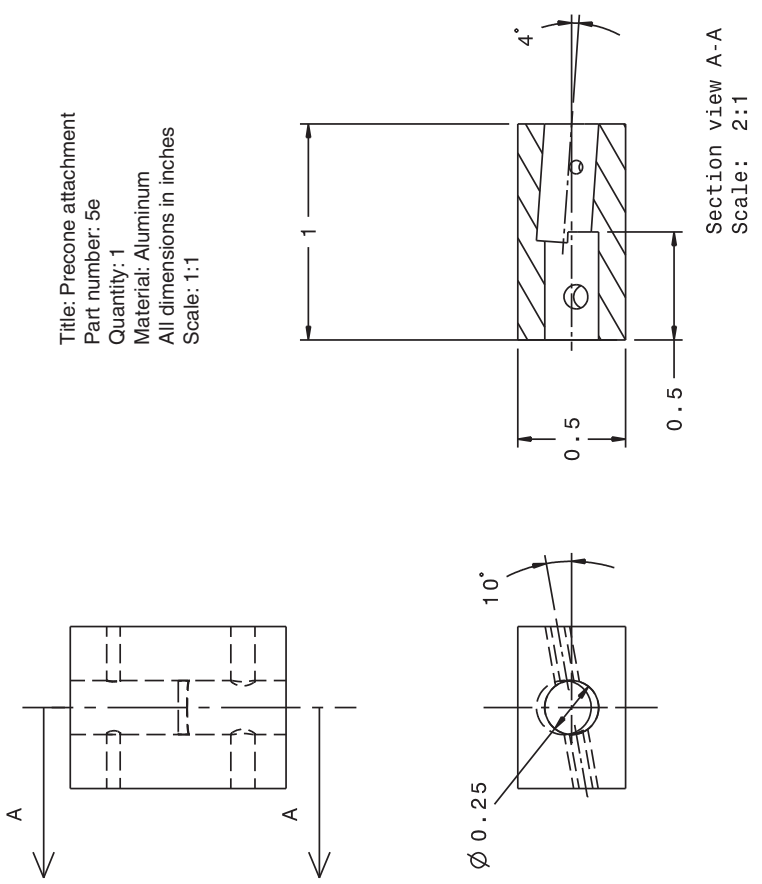

Figure A.21: Precone attachment on the full scale gimballed model.

A.6 **Full scale blade grip.**

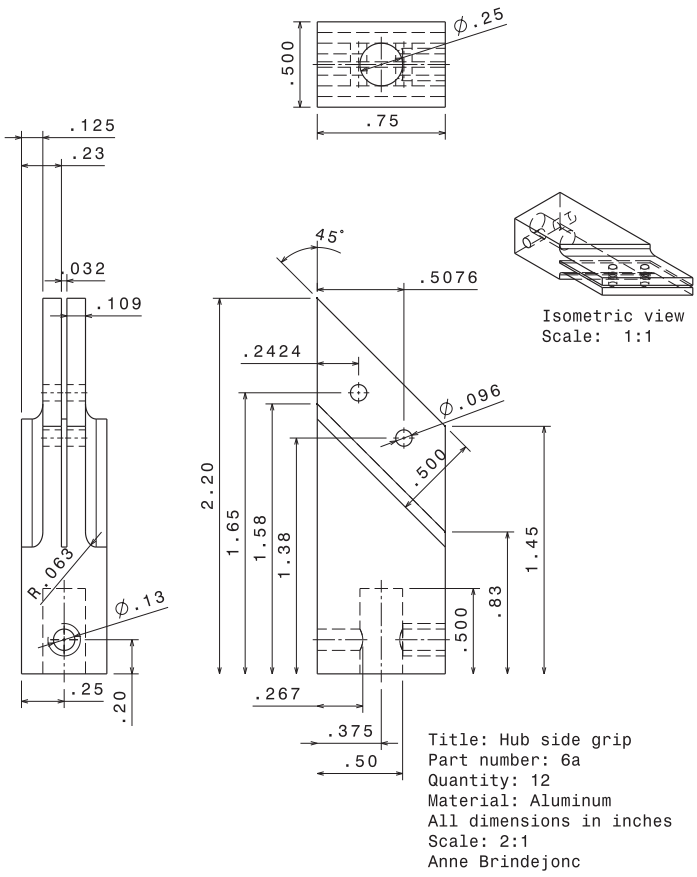

Figure A.22: Full scale blade grip: part attached to the hub.

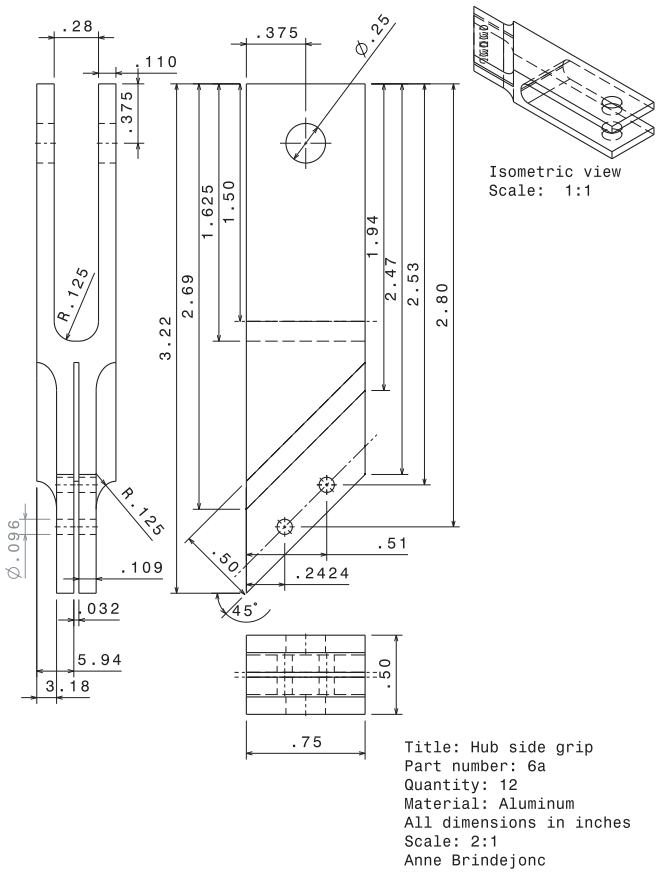

Figure A.23: Full scale blade grip: part attached to the blade.

BIBLIOGRAPHY

[1] Hudson G. C. "Roton Development and Flight Test Program". *American Institute of Aeronautics and Astronautics*, (A98-45950):370–377, 1998.

[2] Leishman J.G. *Principles of Helicopter Aerodynamics*. Cambridge University Press, 2000.

[3] Leishman J.G. "The Autogyro : The First Rotating-Wing Aircraft. Part 1 : That Curious Phenomenon of Autorotation". *Vertiflite*, 49(2):48, 2003.

[4] Prouty R.W. *Helicopter Performance, Stability, and Control*. Krieger Publishing Company, Malabar Florida, 2002.

[5] Prouty R.W. "Torque Distribution in Autorotation". *Vertiflite*, 48(2):28, 2002.

[6] Lambermont P. *Helicopters and Autogyros of the World*. 1958.

[7] Bartz J. and Miklosovic D.S. An experimental analysis of camber effects of a 6-bladed flapped autorotational aerodynamic decelerator, AIAA#2003-2143. *17th AIAA Aerodynamic Decelerator Systems Technology Conference and Seminar, Monterey, California*, May 2003.

[8] Wernicke R.F. "Preliminary Tests of Model Spacecraft Rotor Landing System". Technical report, Bell Helicopter Corporation, 1959.

[9] Kretz M. "Space Rotor : A European Project for Recovery of Heavy Lauch Vehicles". In 6^{th} *European Symposium on Space Technology*, Brighton, England, May 1966.

[10] Levin A.D. and Smith R. C. "An Analytical Investigation of the Aerodynamic and Performance Characteristics of an Unpowered Rotor Entry Vehicle". Technical Report NASA TN D-4537, April 1968.

[11] Levin A.D. and Smith R.C. "experimental aerodynamics of a rotor entry vehicle". *Journal of Aircraft*, 6(4):330–335, July-August 1969.

[12] Sirohi J., Nagaraj V.T., and Chopra I. "Design and Testing of a Rotor for Autonomous Autorotation". Baltimore, June 2004. Sixtieth Annual Forum of the American Helicopter Society International.

[13] K. Washizu, A. Azuma, J. Koo, and T. Oka. Experimental on a model helicopter rotor operating in the vortex ring state. *Journal of Aircraft*, 3:225–230, 1966.

[14] Rohacell. http://www.rohacell.com.

[15] Analog Devices. "Low-Cost +/- 2 g Dual-Axis Accelerometer With Duty Cycle Output". http://www.sparkfun.com, 2005.

[16] Kulite Semiconductor Products. "High Performance, 5VDC Output IS Pressure Transducers". http://www.kulite.com.

[17] Onset Computer Corporation. "Tattletale Model 8 Operation Manual". http://www.onsetcomp.com.